Fringe effect of electrical capacitance and resistance tomography sensors and its application in 3D imaging

A thesis submitted to The University of Manchester

for the degree of Doctor of Philosophy

in the Faculty of Engineering and Physical Science

2014

Jiangtao Sun

School of Electrical and Electronic Engineering

Table of Contents

List of figures

List of tables

Abstract

This PhD work is dedicated to investigating the fringe effect of electrical capacitance tomography (ECT) and electrical resistance tomography (ERT) sensors systematically, exploring possible solutions and developing a novel 3D imaging technique by utilising the fringe effect of electrical tomography (ET) sensors.

By referring to 2D simulation results, the fringe effect is investigated for 3D ERT and ECT sensor models with or without grounded guards, and with different axial lengths of electrodes. Simulation results reveal that increasing the electrode length or adopting grounded guards can reduce the fringe effect of ECT and ERT sensors.

In this work, a voltage-excitation strategy is proposed and validated for ERT sensors instead of the conventional current-injection strategy. This approach enables ECT and ERT sensors to be integrated together as a common one to simplify the sensor design and reduce the interference between the ECT and ERT dual-modality measurements.

For a conventional ERT sensor with the adjacent strategy, the fringe effect is evaluated for axially non-uniform central core and off-central core distributions at different axial positions and with different axial dimensions and conductivity contrasts. A method is proposed for compensating the fringe effect with the above typical distributions and a two-object distribution. A three-plane ERT sensor scheme is suggested for reducing the fringe effect induced by objects outside the sensor plane and the over-estimation by Landweber iteration. Both simulation and experiment have proved the effectiveness of the three-plane sensor scheme and the compensation method.

Using the fringe effect, a novel 3D imaging method is proposed for ET with a single-plane sensor. It is explored to image metallic objects with ECT. The axial position of the object is derived by examining the corresponding fringe effect in a single-plane ECT sensor. Along with 2D imaging of the cross-sectional distribution, 3D imaging is achieved for a cylindrical metallic rod with known size. With this method, only the 3D position of the object needs to be calculated during the reconstruction which reduces the number of unknowns greatly and can improve the accuracy and stability of reconstruction.

Declaration

No portion of the work referred to in the thesis has been submitted in support of an application for another degree or qualification of this or any other university or other institute of learning.

Copyright statement

i. The author of this thesis (including any appendices and/or schedules to this thesis) owns any copyright in it (the "Copyright") and s/he has given The University of Manchester the right to use such Copyright for any administrative, promotional, educational and/or teaching purposes.

ii. Copies of this thesis, either in full or in extracts, may be made **only** in accordance with the regulations of the John Rylands University Library of Manchester. Details of these regulations may be obtained from the Librarian. This page must form part of any such copies made.

iii. The ownership of any patents, designs, trademarks and any and all other intellectual property rights except for the Copyright (the "Intellectual Property Rights") and any reproductions of copyright works, for example graphs and tables ("Reproductions"), which may be described in this thesis, may not be owned by the author and may be owned by third parties. Such intellectual Property Rights and Reproductions cannot and must not be made available for use without the prior written permission of the owner(s) of the relevant Intellectual Property Rights and/or Reproductions.

iv. Further information on the conditions under which disclosure, publication and exploitation of this thesis, the Copyright and any Intellectual Property Rights and/or Reproductions described in it may take places is available in the University IP Policy (see http://www.campus.manchester.ac.uk/medialibrary/policies/intellectual-property.pdf), in any relevant Thesis restriction declarations deposited in the University Library, The University Library's regulations (see http://www.manchester.ac.uk/library/aboutus/regulations) and in The University's policy on presentation of Theses.

Acknowledgements

As a PhD student at the group of Sensing, Imaging and Signal Processing (SISP), it has been my privilege to have inspiring and fruitful discussions with many staff and fellow students there. In particular, I would like to sincerely appreciate and thank:

My supervisor, Prof. Wuqiang Yang, for his constant encouragement and insightful guidance in doing my research as well as valuable suggestions on how to be a good person.

The China Scholarship Council for financially supporting my PhD study at the University of Manchester.

Prof. Peyton and Prof. Ozanyan for helpful discussions about my research topic in my first and second year vivo respectively.

Prof. Hongwei Bian and Dr Zhigang Qu for valuable discussions about how to finish my PhD study; Dr Yi Li for his help with the simulation of electrical capacitance sensors at the initial stage of my PhD study; Dr Wuliang Yin for helpful discussions about the possible solutions to some problems encountered in my research.

The staff in the mechanical workshop at the school of electrical and electronic engineering for their assistance and advice on the fabrication of several ECT and ERT sensors.

At last, I would like to express my grateful thanks to my parents who gave me life and has been giving me immerse support throughout my life; my girlfriend Dun Liu who encouraged and supported me to get over the hard times in the past three years; my fellow students Zhen Ren, Wenqian Zhu, Chao Liu, Chengwei Gan, Mengqi Bai and Yuedong Xie for their friendship and the fun time with them.

Publications

[1] Sun J T and Yang W Q (2014), Evaluation of fringe effect of electrical resistance tomography sensor, *Measurement*, 53, pp 145–160

[2] Sun J T, Yang T M and Yang W Q (2014), Adaptive selection of relaxation factor and number of iterations in Landerweber iteration, *IEEE Trans. Inst. Meas.*, under review

[3] Sun J T and Yang W Q (2013), Fringe effect of electrical capacitance and resistance tomography sensors, *Meas. Sci. Technol.*, 24, pp 074002

[4] Sun J T and Yang W Q (2012), 3D Effect of Electrical Capacitance and Resistance Tomography Sensors, *Proc. IEEE Int. Conf. on Imaging Systems and Techniques*, 16–17 July, Manchester, UK, pp 562–565

[5] Bian H W, Sun J T and Yang W Q (2012), Theoretical analysis method for Howland current source design, *J. Meas. Sci. Instrum.*, 3 (3), pp 287–293

[6] Sun J T and Yang W Q (2011), 3D issues of electrical capacitance and resistance tomography sensors, *Proc. IASTED Int. Conf. on Signal and Image Processing and Applications*, 22–24 June, Crete, Greece

Acronyms and symbols

Acronyms:

AC	alternating current
ART	algebraic reconstruction technique
BEM	boundary element method
CMOS	Complementary Metal-Oxide Semiconductor
CMRR	common mode rejection ration
DAQ	data acquisition
DC	direct current
ECT	electrical capacitance tomography
ECVT	electrical capacitance volume tomography
EIT	electrical impedance tomography
EMT	electrical magnetic tomography
ERT	electrical resistance tomography
ET	electrical tomography
FDM	finite difference method
FEM	finite element method
GPU	graphics processing units
GUI	Graphical User Interface
IEEE	Institute of Electrical & Electronics Engineers
LBP	linear back projection
LCR	inductance/capacitance/resistance
L-M	Levenberg-Marquardt
PC	Personal Computer
PCB	printed circuit board
PDE	partial differential equation
PSD	Phase-sensitive demodulation
RMS	root mean square
SNR	signal-to-noise ratio
SVD	singular value decomposition
TSVD	truncated singular value decomposition
USB	universal serial bus

Symbols:

$\varepsilon(x, y)$	permittivity distribution
$\varphi(x, y)$	electric potential distribution (V)
$\rho(x, y)$	static charge distribution (C)
$E(x, y)$	electric field distribution (V/m)
$\Delta V_{i,j}$	potential difference (V)
Γ_j	electrode surface
$\sigma(x, y)$	conductivity distribution (S/m)
Q	surface charge (C)
E_i, E_j	current-injection and sank electrodes
V_0	potential (V)
V	volt
n	outer norm direction
J	current density (A/m^2)
I_0	magnitude of injected current (A)
ω	angular frequency (rad/s)
$\varphi(x, y)$	complex potential distribution (V)
j	imaginary unit $\sqrt{-1}$
i, j	electrode or electrode pair index
V_i	voltage phasor
I_j	current phasor
$Z_{i,j}$	inter-electrode impedance (Ω)
$Im(Z_{i,j})$	imaginary part of $Z_{i,j}$
$Re(Z_{i,j})$	real part of $Z_{i,j}$
$C_{i,j}$	inter-electrode capacitance (pF)
$G_{i,j}$	inter-electrode conductance (S)
$P(x, y)$	pixel area (m^2)
$i - j$	electrode pair index
(x, y)	2D position
V_i, V_j	AC voltage (V)
N	number of electrodes

$S(x, y)$	sensitivity distribution
$S_{i,j}$	sensitivity map
$S_{i,j}^{*}$	normalised sensitivity map
I_i, I_j	AC current (A)
k	pixel index
λ	normalised capacitance
C_m	measured capacitance (pF)
C_l, C_h	low and high reference capacitance (pF)
V	normalised change of voltage difference (V)
V_m, V_r	measured and reference voltage difference (V)
ΔC	vector of measured capacitance change
$\Delta\varepsilon$	vector of permittivity change
J	Jacobian matrix
M	number of independent measurements
N	number of pixels
S	normalised sensitivity matrix
g	normalised vector of permittivity distribution
S^{-1}	analytical inverse of S
$\hat{g}$	reconstructed permittivity distribution
S^T	transpose of S
e	measurement noise vector
U	$M \times M$ orthogonal matrix
V	$N \times N$ orthogonal matrix
Σ	$M \times N$ diagonal matrix
p	rank of S
$\delta_1, \cdots \delta_p$	non-zero singular values of S
Σ^{-1}	inverse of Σ
U^T	transpose of U
V^T	transpose of V
$diag[]$	diagonal matrix
$f(\delta)$	spectral filter
δ	Σ
μ	regularisation parameter

μ_λ	identity vector
I	identity matrix
α_k	relaxation factor in Landweber iteration
$k, k+1$	iteration step index
g_k, g_{k+1}	normalised permittivity vector for k_{th} and $k+1_{th}$ iteration
P	projection operator
S_k	k_{th} row vector of S
λ_k	k_{th} normalised capacitance
RIE	relative image error
CR	capacitance residual
CC	correlation coefficient
$\bar{\hat{g}}$	mean values of g
$\bar{g}$	mean values of $\hat{g}$
C_{equ}	equivalent capacitance (pF)
C_0	elementary capacitance (pF)
$C_{a_1}, \cdots C_{a_n}$	capacitance induced by fringe effect above sensor plane (pF)
$C_{b_1}, \cdots C_{b_n}$	capacitance induced by fringe effect below sensor plane (pF)
R_{equ}	equivalent resistance (Ω)
R_0	elementary resistance (Ω)
$R_{a_1}, \cdots R_{a_n}$	resistance induced by fringe effect above sensor plane (Ω)
$R_{b_1}, \cdots R_{b_n}$	resistance induced by fringe effect below sensor plane (Ω)
V_A	amplitude of an AC voltage (V)
V_{RMS}	measured RMS value of V_A (V)
$Crest\ factor$	ratio of peak value to RMS value of a waveform
V_{ac}	vector of potential differences after compensation
V_m, V_t, V_b	measured vectors of potential differences from middle, top and bottom electrode planes respectively
WF	weighting factor
V_r	vector of potential residual
V_n	measured vector of potential differences
C_f	calculated fringe effect of an ECT sensor with dielectric object
C_{2D}	averaged capacitance with 2D model for calculation of C_f

C_{3D}	averaged capacitance with 3D model or experiment for calculation of C_f
$C_f^{'}$	calculated fringe effect of an ECT sensor with metallic object
$C_{2D}^{'}$	averaged capacitance with 2D model for calculation of $C_f^{'}$
$C_{3D}^{'}$	averaged capacitance with 3D model or experiment for calculation of $C_f^{'}$
kΩ	1000 Ohm
NR	norm ratio of two images
$\hat{g}$	reconstructed image for 3D model
g	reconstructed image for 2D model
ε_r	relative permittivity
∇	gradient operator
$\nabla \cdot$	divergence operator

Chapter 1: Introduction

This chapter briefly introduces the research topic studied in this thesis. There are three main sections: background, motivation and objectives of this research, plus the organisation of this thesis.

1.1 Background

1.1.1 2D and 3D imaging in electrical tomography

The concept of electrical tomography (ET) was established in the 1980s (Barber and Brown 1984, Fasching 1988, Huang *et al*. 1988a). ET is a technique used to visualise and measure the distribution of materials with different electrical or magnetic properties within an imaging plane or volume of interest using a proper multi-electrode/coil sensor. There are three modalities of ET: Electrical Capacitance Tomography (ECT), Electrical Resistance Tomography (ERT) and Electro-magnetic Tomography (EMT), with similar sensing principles but measuring different electrical or magnetic properties and for different applications. The typical application of ET in industry is to measure a multi-phase flow, featured by providing 2D (Two-dimensional) or 3D (Three-dimensional) reconstructed images.

With 2D imaging, a uniform electrical field distribution is assumed along the axial direction of a single-plane ET sensor, which can only be achieved with infinite or sufficient long electrodes (Peng *et al*. 2005) for axially uniform distributions. Under this condition, the 3D field distribution can be represented by a 2D one. As a result, a 2D slice or cross-sectional image of the 3D material distribution can be reconstructed based on the 2D sensitivity matrix, which is derived from the 2D electric field distribution. Therefore, 2D imaging can be regarded as a simplified version of 3D imaging and has been extensively investigated and applied to various applications (York 2001, Yang 2010, Giguère *et al*. 2008, York *et al*. 2011).

Since the material distribution of a multi-phase flow in industry and the electric field of an ET sensor are essentially 3D, a great effort has been dedicated to 3D imaging with ERT and ECT recently (Banasiak *et al*. 2010, Banasiak *et al*. 2012, Cao and Xu 2013, Dehghani *et al*. 2005, Li 2008, Marashdeh *et al*. 2008, Murphy *et al*. 2006, Pinheiro *et*

al. 1998, Soleimani *et al*. 2007, Soleimani *et al*. 2009, Warsito and Fan 2005, Wilkinson *et al*. 2006, Wajman *et al*. 2006, Warsito *et al*. 2007, Li and Holland 2013). Most of those 3D imaging techniques employ a multi-plane sensor and utilise the measurements between electrode planes as proposed by Wajman *et al*. (2006). To improve the signal-to-noise ratio (SNR) of 3D ECT imaging with short electrodes, a variety of electrode geometries can be applied, subject to the shape of the imaging volume, i.e. the so-called electrical capacitance volume tomography (ECVT) (Warsito *et al*. 2007) and the small measurements between the vertically distant electrodes may be abandoned (Warsito *et al*. 2007, Li and Holland 2013). Although the achieved 3D imaging results seem promising, more effort is needed to improve the image quality because of the following three main reasons.

Firstly, most of them are implemented with incomplete measurement data because the electrodes on both the bottom and top ends of a true 3D sensor are normally removed for the measurements (Soleimani *et al*. 2007). The one with complete measurement data should be similar to true 3D ECT imaging proposed by Li (2008) and Soleimani *et al.* (2007). It means that the 3D reconstructions with incomplete measurement data are only approximated 3D imaging.

Secondly, the condition number of the sensitivity matrix of a 3D ET sensor is much larger than that of a corresponding 2D sensor due to the increased number of unknowns, as compared by Li (2008) between 2D and true 3D ECT sensors. A much larger condition number means that 3D ET imaging presents a more severely ill-posed and ill-conditioned problem and would suffer from very small measurement errors, such as measurement noise or simulation errors (Soleimani *et al*. 2007). This brings high demands on sensor fabrication and measurement electronics. A fast reconstruction algorithm was implemented by Pinheiro *et al.* (1998) to reduce the condition number of 3D ERT imaging but led to deteriorated image resolution.

Thirdly, 3D imaging with a reasonable resolution takes a much longer time than 2D imaging (Li 2008, Pinheiro *et al*. 1998, Soleimani *et al*. 2007) because it needs to obtain the approximated inverse of a very large sensitivity matrix for image reconstruction, as indicated by the large number of independent measurements and voxels for imaging. This would limit its application in situations with high commands on real-time performance. 3D imaging by a single-plane ET sensor was attempted. However, neither

the position nor the shape of the object can be correctly reconstructed (Cao and Xu 2013, Soleimani *et al*. 2007). More geometry parameters in a 3D ET sensor also makes the sensor design more difficult than a 2D one since the approximated 3D imaging is an "open-field" as described by Li (2008).

In view of the above points, 2D ET imaging is preferred in most practical cases.

1.1.2 Fringe effect in 2D imaging

As mentioned previously, only infinite or sufficient long electrodes can make the electric field distribution of an ECT sensor uniform in the z-direction for an axially uniform distribution. In reality, however, the electrode length is limited, which would lead to an electric field's distortion on the both ends of electrodes, i.e. the fringe effect. The fringe effect results in: (1) the sensor has different sensitivities to the perturbations of material distribution at different axial layers (Yan *et al*. 1999, Peng *et al*. 2005); (2) even the material distribution outside the imaging volume of interest can be sensed and hence affect the reconstructed image (Yan *et al*. 1999). Because the inverse problem of ET is badly ill-conditioned (Wang *et al*. 2002, Ma *et al*. 2006, Yang 2007b), the fringe effect would distort the constructed image severely, even if the resultant change in the measured data may be insignificant. This means that the fringe effect would make the simplification of 3D imaging into 2D non-permissible, if it is not minimised.

Few literatures have considered the fringe effect in ECT sensors due to their finite electrode length. Yan *et al*. (1999) investigated the fringe effect by comparing the sensing ranges and the reconstruction errors of ECT sensors without or with different guards for some distributions. However, they did not examine the influence of the electrode length on the fringe effect. Peng *et al*. (2005) tried to determine the optimal electrode length by comparing simulation results of 3D models with those of 2D models to make the fringe effect negligible for a certain sensor structure, but only qualitative results were given. Alme and Mylvaganam (2006a) simulated the fringe effect in ECT/ERT sensors using COMSOL Multiphysics (a commercialised FEM package). They concluded that the 3D simulation of ECT sensors are closer to the experimental results than the 2D simulation, and the fringe effect of an ECT sensor can be quite small for low permittivity materials regarding the capacitance values before normalisation. Similarly, Alme and Mylvaganam (2006b) compared the resultant capacitance before

normalisation from the 2D and 3D simulation of the same ECT sensor for homogeneous distribution, and found that the fringe effect, represented by the difference between absolute capacitance before normalisation from 2D and 3D simulation, would increase almost linearly with permittivity in the image area. York *et al*. (2011) suggested that it is a challenge to constrain the 3D electric field distribution of an ECT sensor to a 2D plane, i.e. it is very difficult to achieve 2D imaging with a negligible fringe effect. All the above confirmed that serious fringe effect would occur if an ECT sensor is not properly designed. Quantitative investigation is still desired for the fringe effect of ECT sensors with different structure and geometry.

Up to now the fringe effect of ERT sensors for 2D imaging has not been investigated systematically. Alme and Mylvaganam (2006a) asserted that the small "pin" electrodes suggest that the fringe effect is prominent for a conventional ERT sensor. The fringe effect was illustrated qualitatively and avoided by using voltage-excitation and long strip electrodes (not "pin" electrodes) as described by Li and Yang (2009). It was investigated quantitatively by comparing the simulation results of a 3D ERT sensor with the corresponding 2D analysis when the fringe effect was ignored (Ma *et al*. 1997), or comparing the 2D and 3D simulation results with the corresponding experimental results (Fransolet *et al*. 2002, Alme and Mylvaganam 2006a). Those comparisons show that the fringe effect is severe for a conventional ERT sensor and would be reduced by using longer electrodes. However, the comparison was made quantitatively only for simulated or measured potential differences before normalization, which may be referred to as "absolute" fringe effect. The normalised potential differences, however, really matter in image reconstruction. Meanwhile, the current-injection strategy was adopted for ERT in all those comparisons, except for that by Li and Yang (2009), which only gave a qualitative illustration of the electric field distribution of an ERT sensor with voltage-excitation. Therefore, the fringe effect of ERT sensors with either current-injection or voltage-excitation needs to be further exploited.

1.1.3 Reducing and making use of fringe effect

To reduce the fringe effect, possible solutions may be derived from the simplification of a 3D model for ET into a 2D one in simulation with finite element method (FEM) as suggested by Yan *et al*. (1999). In the simulation, a 3D model of an ET sensor with a limited axial length (user-defined) is simplified into a 2D one based on the assumption

that the electric field distribution is axially uniform within the axial sensing range of the ET sensor, which is constrained to the user-defined volume enclosed by the electrode plane, i.e. no fringe effect presents in this case. Take ECT as an example, this assumption can be approximately fulfilled with two prerequisites in practice: (1) The measurement electrodes are sufficient long (Peng *et al*. 2005) and appropriate guards are applied, e.g. the use of grounded end guards to constrain the axial sensing range of the sensor (Yan *et al*. 1999); (2) The permittivity distribution is axially uniform (Yan *et al*. 1999) since the electric field distribution also depends on the permittivity distribution. This means that the fringe effect of an ET sensor can be affected by two factors: (1) sensor structure and geometries and (2) axial object distribution. Systematic investigation of the fringe effect may help find solutions to reduce the fringe effect.

2D FEM simulation with COMSOL Multiphysics can be used as the reference to evaluate the fringe effect of an ET sensor. As mentioned above, the measured data from an ET sensor contains the fringe effect, which is influenced by the axial material distribution, e.g. the axial position of a single rod inside the sensing range of the sensor. This makes it possible to implement 3D imaging of certain processes with a conventional single-plane ET sensor, which is actually designed for 2D imaging.

1.2 Motivation and objectives

1.2.1 Motivation

Based on the above discussion, there are three motivations for this study:

(1) Systematic investigation is still needed for the fringe effect of ECT and ERT sensors (with either current-injection or voltage-excitation), especially regarding the normalised measurements
(2) Effective methods need to be sought to reduce the fringe effect
(3) Fringe effect may be used to achieve 3D imaging of certain processes with a single-plane ET sensor.

1.2.2 Objectives of this study

This study aims to investigate and reduce the fringe effect of ECT and ERT sensors as well as apply the fringe effect for 3D imaging with a conventional single-plane ECT sensor. The objectives include:

(1) To evaluate the fringe effect of ECT and ERT sensors for different electrode length, the use of grounded guards and different axial object distributions
(2) To minimise the fringe effect of ECT and ERT sensors by optimising the sensor design or using compensation methods
(3) To achieve the fringe-effect-based 3D imaging of a metallic rod in dielectric material with a conventional single-plane ECT sensor.

The novelties of this study include:

(1) A voltage-excitation strategy is proposed for the use with ERT sensors to apply grounded end guards for minimised fringe effect and integrate ECT and ERT sensors together for improved dual-modality measurement

(2) By systematic investigation, it is found that increasing the electrode length and applying grounded end guards can reduce the fringe effect of ECT and ERT sensors with voltage-excitation for axially uniform distributions

(3) It is found that the fringe effect is related to the axial position and dimension of an object distribution as well as the conductivity contrast of the two phases to be imaged, which can be minimised with a compensation method based on selective scaling

(4) A three-plane ERT sensor scheme is proved to be effective in reducing the fringe effect induced by objects outside the measurement sensor plane and the over-estimation of object size by Landweber iteration

(5) Given the prior knowledge about the shape and size, a metallic rod in table salt or deionised water is accurately reconstructed in 3D by making use of the fringe effect with a conventional single-plane ECT sensor designed for 2D imaging.

1.3 Organisation of thesis

In the beginning of the thesis, the background, motivation and objectives are briefly introduced.

Chapter 2 reviews the fundamentals of ECT and ERT, including their basic principles, hardware, forward problems, FEM simulation models, sensitivity calculation, data normalisation, inverse problem and popular reconstruction algorithms.

Chapter 3 investigates the fringe effect of ECT and ERT sensors due to the sensor design. The influence of both electrode length and grounded end guards on the fringe effect will be evaluated. A voltage-excitation strategy and grounded guards are applied to ERT for the first time. A common structure for ECT and ERT sensors is proposed to reduce their fringe effect and an integrated sensor is designed for ECT/ERT dual-modality measurement.

Chapter 4 evaluates the fringe effect of a conventional ERT sensor due to the axial object distribution. The fringe effect is examined by considering the axial position and dimensions as well as the conductivity contrast of some typical object distributions. A compensation method and a three-plane ERT sensor are suggested to minimise the fringe effect.

Chapter 5 presents an application of fringe effect for 3D imaging with a single-plane ECT sensor. The 3D imaging principle and metal detection are illustrated. 3D imaging of a metal rod is implemented with both table salt and deionised water as the background material. Some calibration issues are addressed.

Finally in Chapter 6, general conclusions are drawn from this research and suggestions are given for future work.

Chapter 2: Fundamentals of ECT and ERT

ET is based on soft-field sensing as the electric field or sensitivity distribution depends on the material distribution. Because of the soft-field sensing and the limited or small number of measurements on the boundary of the imaging volume, the inverse problem for ET is intrinsically ill-posed and challenging. ECT and ERT are two ET techniques, which have been extensively investigated in the past two decades. This chapter presents a review of the fundamentals of ECT and ERT in term of their basic principles, forward problems, finite element method (FEM) simulation models, hardware, sensitivity matrix calculation, data normalisation, inverse problems, popular reconstruction algorithms as well as the evaluation of the algorithms.

2.1 Basic principles of ECT and ERT

Figure 2.1 shows a typical 8-electrode ECT system, which consists of three parts: an ECT sensor, a data acquisition system or unit (including a sensing electronics), and an image computer (e.g. a PC). A typical ERT system has a similar structure, but with a different sensor and sensing electronics. The permittivity or conductivity change of the material inside the imaging area can be sensed by the ET sensor. The corresponding analogue signal in a selected measurement channel is conditioned by the sensing electronics, converted into a digital signal and transmitted to the PC through the data acquisition (DAQ) unit. The PC is used to select the measurement channel, control the data acquisition process, implement image reconstruction algorithms and display the reconstructed image.

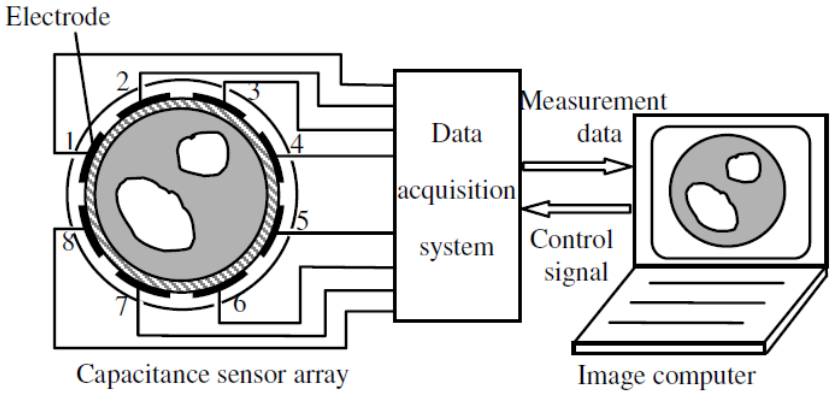

Figure 2.1 A typical 8-electrode ECT system (Wu *et al*. 2013)

An ECT or ERT sensor consists of a number of electrodes, typically 8, 12 or 16 electrodes for ECT and 16 or 32 electrodes for ERT, which are evenly mounted around the external or internal periphery of a circular insulated pipe, but occasionally a conductive pipe in ERT. As an example, Figure 2.2 shows a typical 12-electrode ECT sensor.

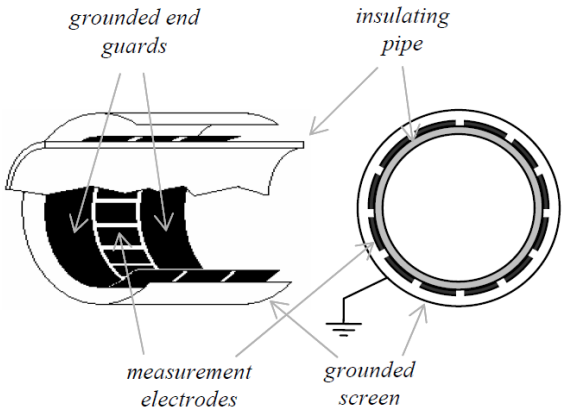

Figure 2.2 A typical 12-electrode ECT sensor (Flores *et al*. 2005)

As shown in Figure 2.2, the typical ECT sensor is made up of four parts: an insulating pipe, measurement electrodes, grounded end guards and a grounded outer screen. The grounded end guards and outer screen are metallic and used to eliminate the interference of outside noises (Yang 2010). For a typical ERT sensor, however, it is not necessary to use grounded end guards and outer screen due to different sensing mechanisms and different applications. ECT is usually applied to image a permittivity distribution of a two-phase flow with the continuous phase being non-conductive while ERT is usually for visualising the conductivity distribution of a two-phase flow with the continuous phase being conductive. Since the electrodes need to be in contact with the continuous phase inside the imaging region of an ERT sensor, they are normally mounted on the inner surface of the pipe. Generally, the measurement electrodes of ECT sensors are long strip metal (Yang 2010) while the measurement electrodes of ERT sensors are small "pin" metal (Dickin and Wang 1996). The measurement electrodes can be made of different types of metals, e.g. solid brass plate (Huang *et al*. 1989), copper adhesive tape (Yang 2010) or copper layer in printed circuit board (PCB) (Mohamad *et al*. 2012) for ECT sensors and stainless steel, silver, gold, platinum or silver palladium (Dickin and Wang 1996) for ERT sensors. In some occasions, grounded radial screens may be used to reduce the standing capacitance between adjacent electrodes (Yang 2010).

To interrogate an imaging area of interest, an electrical signal, i.e. an alternating voltage (ECT) or current (ERT), is applied to an electrode with other electrodes being grounded in the case of ECT or a pair of electrodes with other electrodes floating in the case of ERT, to generate an excitation field. A set of capacitance or resistance measurements is then taken from other available electrodes or electrode pairs according to the measurement strategy employed, which is called a projection. By moving the excitation source around the pipe, other projections from different angles can be obtained to form a complete set of measurement data. The forward problem needs to be solved to calculate the electric field distribution in the interior area of the sensor and predict the measurements at the boundary electrodes or electrode pairs from an arbitrary material distribution for image reconstruction.

The measured data are then normalised and converted into a 2D cross-sectional image or 3D image to present the material distribution inside the pipe using a proper image reconstruction algorithm. This is termed as solving the inverse problem. The forward problem and inverse problem will be discussed in details later.

For an ECT sensor with the conventional measurement protocol, a complete set of independent capacitance measurements are taken between all possible combinations of the electrodes. The number of independent measurements is given by $N * (N - 1)/2$, where N is the number of electrodes. For example, all possible electrode combinations with a typical 12-electrode ECT sensor are shown in Figure 2.3, giving 66 independent measurements.

Different measurement protocols were discussed and compared by Alme and Mylvaganam (2007) and Yang and Peng (2013). While different electrode combination strategies showed certain superiorities over the conventional single-electrode strategy regarding the quality of reconstructed images, the total number of independent measurements is determined by the number of electrodes only.

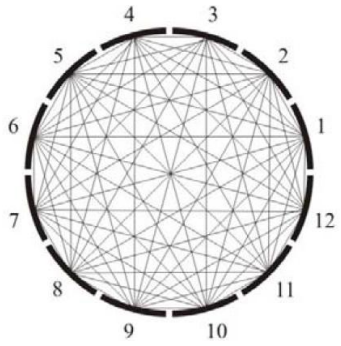

Figure 2.3 Possible electrode combinations with a typical 12-electrode ECT sensor (Flores *et al*. 2005)

For an ERT sensor, a typical data collection strategy is the adjacent strategy, which applies an alternating current to all possible pairs of adjacent electrodes, and measures potential differences between adjacent electrodes (Dickin and Wang 1996). To deal with the problems caused by the contact impendence on the electrode-electrolyte interface, the measured potential difference related to current-injecting electrodes are discarded. Because reciprocity exists between the pairs of current-injecting and voltage-measuring, the number of independent measurements for potential difference is given by $N * (N - 3)/2$, where N is the number of electrodes (Barber *et al*. 1983). A 16-electrode ERT sensor gives 104 independent measurements, presenting the potential difference with this strategy. Different protocols for data acquisition in ERT, e.g. adjacent, opposite and diagonal strategy with non-conductive boundary and the conductive boundary strategy, were discussed by Dickin and Wang (1996). Before image reconstruction, the capacitance or resistance measurements need to be normalised for calibration purpose, which will be discussed later.

To calculate the sensitivity matrix, the imaging area inside an ET sensor needs to be divided into small pixels for FEM or finite difference method (FDM) analysis to determine the changes in capacitance between a pair of electrodes or resistance between two electrode pairs due to a small perturbation of the permittivity or conductivity in each pixel, and also for image reconstruction. The reconstructed image can be represented by a matrix, each element of which is allocated a grey level of a pixel at a specified spatial position. The number of pixels is typically in the order of 1000 (Yang and Peng 2003), which is much larger than the number of independent measurements from an ET sensor. It is this reason that it is impossible to obtain a unique solution for each image pixel, i.e. the inverse problem is ill-posed and ill-conditioned (Yang 2007b, Wang *et al*. 2002), which results in blurred images. Also, because of the soft-field nature of ET, the spatial resolution of ET is relatively low, e.g. it is between 3 and 10% of the sensor diameter for ERT (Dyakowski *et al*. 2000, Wilkinson *et al*. 2006).

2.2 Forward problem and FEM simulation model

ET systems typically employ an alternating voltage or current with a fixed frequency below 1 MHz, which is sufficiently low to ignore the coupling between electric and magnetic fields. Because the corresponding wavelength is larger than the typical sensor size by several orders of magnitude at this frequency range, the electric potential

distribution inside an ET sensor can be approximately described by the electrostatic field theory. Accordingly, the 2D electric field distribution inside an ECT sensor can be described by the Poisson equation and formulated as (Loser *et al*. 2001):

$$\nabla \cdot [\varepsilon(x,y)\nabla\varphi(x,y)] = -\rho(x,y) \tag{2.1}$$

where $\varepsilon(x,y)$ is the permittivity distribution, $\varphi(x,y)$ is the electric potential distribution, and $\rho(x,y)$ is the static charge distribution, which is the source of the electric field. In most cases, there is no charge inside the ECT sensor. Thus, equation (2.1) becomes the following Laplace equation:

$$\nabla \cdot [\varepsilon(x,y)\nabla\varphi(x,y)] = 0 \tag{2.2}$$

where the electric field is given by $E(x,y) = -\varphi(x,y)$. Note that with equation (2.2) it is assumed that the conductivity of the medium inside the ECT sensor is negligible. If the potential distribution is known, the capacitance between a pair of electrodes (excitation electrode i and detection electrode j) can be defined as (Yang and Peng 2003):

$$C_{i,j} = \frac{Q}{\Delta V_{i,j}} = -\frac{1}{\Delta V_{i,j}} \iint_{\Gamma_j} \varepsilon(x,y)\nabla\varphi(x,y)d\Gamma \tag{2.3}$$

where $\Delta V_{i,j}$ is the potential difference between the electrode pair, Γ_j is a surface enclosed by the detection electrode j and Q is the surface charge on Γ_j. This definition of the capacitance between a pair of electrodes was also proposed by Xie *et al*. (1990) with more details included, e.g. the influence of a boundary condition.

Similarly, the 2D electric field distribution inside an ERT sensor can be described as (Lionheart 2001):

$$\nabla \cdot [\sigma(x,y)\nabla\varphi(x,y)] = 0 \tag{2.4}$$

where $\sigma(x,y)$ is the conductivity distribution inside the ERT sensor. For a conventional ERT with the current-injection and voltage-measurement strategy, the potential difference between each specified electrode pair is measured, which can be predicted directly by solving equation (2.4).

Using equations (2.2) and (2.4), the 2D electric field distribution inside an ECT or ERT sensor can be solved for a given permittivity or conductivity distribution and boundary conditions applied to the sensor, i.e. solving the forward problem. Even though the Laplace equation may be the simplest partial differential equation (PDE), it is still too difficult to obtain the analytical solution to the electric field distribution for the typical geometry and the boundary conditions of an ECT or ERT sensor. Therefore, FEM, FDM or boundary element method (BEM) is normally used to calculate a numerical solution. FEM and FDM discretise the sensing region inside an ET sensor into many small elements and a constant permittivity or conductivity is assumed in each element. They use interpolation between the specified nodal values with a polynomial basis to approximate the potential at a certain position and convert the integral equation into a large set of linear equations to solve. BEM only requires the surface of the sensing region to be discretised and uses the boundary integral equation to formulate the governing equation for the electric field. COMSOL Multiphysics can be used to obtain the electric field distribution of ET sensors for simulation purposes. In COMSOL Multiphysics, Electrostatic mode can be chosen to solve the equation (2.2) for ECT while the Conductive Media DC in Electromagnetic module can be used to solve the equation (2.4) for ERT. Besides the governing equations, the boundary conditions need to be defined to obtain a unique solution to the electric field distribution inside an ET sensor. For ECT, the boundary conditions are defined as (Alme and Mylvaganam 2006):

$$\begin{cases} V_0 & Potential\ V_0\ at\ the\ excitation\ electrode \\ 0V & Ground\ at\ all\ the\ detection\ electrodes \\ 0V & Ground\ at\ the\ outer\ screen \end{cases} \tag{2.5}$$

For ERT, if the electrodes E_i and E_j are the current-injection and sank electrodes, respectively, the boundary conditions are defined as (Alme and Mylvaganam 2006):

$$\begin{cases} \oint_{E_i} n \cdot J = I_0 & At\ current\ injection\ electrode\ E_i \\ \oint_{E_j} n \cdot J = -I_0 & At\ current\ sank\ electrode\ E_j \\ n \cdot J = 0 & At\ all\ other\ electrodes \\ n \cdot J = 0 & At\ the\ nonconductive\ boundaries\ between\ electrodes \end{cases} \tag{2.6}$$

where n is the norm direction of the electrode surface, J is the current density, and I_0 is the magnitude of the injected current. In the Conductive Media DC mode, these boundary conditions are called floating potential and electric insulation respectively. This FEM model does not account for the influence of the contact impedance between the electrodes and electrolyte on the ERT measurement since the contact impedance in an industrial application can be ignored with the current-injection strategy and a measurement circuit of high input impedance (Szczepanik and Rucki 2007). For a complete electrode model of ERT sensors including the contact impedance, one can refer to Somersalo *et al*. (1992) and Giguère *et al*. (2008).

If the conductivity of the material inside the sensing region of an ECT sensor cannot be neglected, or the effect of the excitation frequency on the simulation needs to be considered, the governing equation of the electric field becomes (Alme and Mylvaganam 2006):

$$\nabla \cdot [(\sigma(x,y) + j\omega\varepsilon(x,y))\nabla\varphi(x,y)] = 0 \tag{2.7}$$

where ω is the excitation frequency with unit $[rad/s]$, and $\varphi(x,y)$ is the 2D complex potential distribution. The equation (2.7) is also applicable to calculate the electric field distribution for the ECT/ERT dual-modality measurement as discussed by Marashdeh *et al*. (2007) and Li and Soleimani (2013). It can be solved using the "In-Plane Electric Currents" mode of AC/DC module in COMSOL Multiphysics with the same boundary conditions as in equation (2.5). In this case, the inter-electrode impedance between excitation electrode i and detection electrode j can be calculated by (Alme and Mylvaganam 2006):

$$Z_{i,j} = \frac{V_i}{I_j} = \frac{V_i}{\iint_{\Gamma_j} \sigma(x,y)\nabla\varphi(x,y)d\Gamma + j\omega \iint_{\Gamma_j} \varepsilon(x,y)\nabla\varphi(x,y)d\Gamma} \tag{2.8}$$

where V_i is the voltage phasor on electrode i, I_j is the current phasor into electrode j, and Γ_j is a surface enclosed by electrode j. The equivalent capacitance and conductance are then formulated as:

$$C_{i,j} = \frac{1}{\omega} Im(\frac{1}{Z_{i,j}}) \tag{2.9}$$

$$G_{i,j} = Re(\frac{1}{Z_{i,j}}) \tag{2.10}$$

where $Im(Z_{i,j})$ is the imaginary part of $Z_{i,j}$ and $Re(Z_{i,j})$ is the real part of $Z_{i,j}$. Equations (2.3) and (2.8) for inter-electrode capacitance and impedance can be calculated using boundary integration of the post-processing utility in COMSOL Multiphysics. FDM and BEM were adopted by Li and Yang (2008) and Ren *et al.* (2014), respectively, to solve the forward problem. Other two different solvers for the forward problem with ECT were proposed by Marashdeh *et al*. (2006a) and Mirkowski *et al*. (2008), where the feed-forward neural network and a capacitor-mesh model were used respectively.

With FEM or other solvers shown above, a numerical solution of the electric field inside an ECT or ERT sensor can be obtained. This solution can be used to calculate the sensitivity maps, which are needed for image reconstruction or the inter-electrode capacitance for simulation purposes. In many occasions, it is also exploited to estimate the capacitance vector or update the sensitivity maps for a reconstructed permittivity distribution with an non-linear iterative reconstruction algorithm to improve the image quality (Marashdeh *et al*. 2006b, Li and Yang 2008, Mirkowski *et al*. 2008, Banasiak and Soleimani 2010, Ren *et al*. 2014). In many other iterative algorithms, a linear model based on the sensitivity matrix is established to estimate the capacitance vector for a reconstructed permittivity distribution, which will be shown later.

2.3 Hardware for ECT and ERT

2.3.1 Hardware for ECT

The hardware for ECT was reviewed by Yang (1996) and Yang and Peng (2003). Among those, there are mainly three types of hardware, which were developed at the University of Manchester: the charge/discharge circuit (Huang *et al*. 1988b and 1992), the AC-based circuit (Yang *et al*. 1994, Yang and York 1999, Yang 2001), and LCR (inductance/capacitance/resistance) meter (Yang *et al*. 2002). A new multi-channel impedance-analyser-based ET system has been developed by Yang (2007a) and used in different applications e.g. by Hu *et al*. (2008).

With the charge/discharge circuit, the charge transfer principle is applied (Huang *et al*. 1992). The capacitor to be measured is charged and discharged repeatedly by a voltage source through the combined action of four switches and transformed into a voltage by

an op-amp circuit. There are several disadvantages for the charge/discharge circuit: (1) baseline drift due to the DC operation (2) charge injection problems from CMOS switches (3) measuring the combination of capacitance and loss conductance (Yang 1996, Yang 2001).

With the AC-based circuit, a sine-wave voltage with a single frequency is applied for excitation, which can enable narrow-band filters after phase-sensitive demodulation (PSD) to be used. This can significantly reduce the measurement noise and to distinguish between capacitance and loss conductance (Yang 1996, Yang and York 1999). Therefore, the AC-based circuit is adopted in many ECT systems developed up to now for its low drift, high signal-noise-ratio (SNR) and ability to measure both capacitance and loss conductance.

The tomography system based on an HP LCR meter (HP4284A) can be used for both ECT and ERT because either current or voltage signal can be generated for sensor excitation (Yang *et al*. 2002). But it suffers from some drawbacks, e.g. when it is used for ECT with voltage excitation, the measurement sensitivity and accuracy is limited by the large standing capacitance induced by the large coupling capacitance of the used switches. The structure and features of this system are similar to those of the impedance-analyser-based system as shown in Figure 2.4.

The impedance-analyser-based ET system consists of three parts: a multiplexer box, an impedance analyser (HP4192) and a PC as shown in Figure 2.4 (Yang 2007a, Hu *et al*. 2008). The multiplexer box can have 256 channels at the maximum to measure the inter-electrode impedance between specified electrode pairs. Each electrode can be configured in one of the following four modes: (a) excitation, (b) detection, (c) floating, (d) grounded. Due to the keyboard configuration of the reed relay switches inside the multiplexer box, both single-electrode excitation/detection and multi-electrode excitation/detection can be achieved (Yang 2007a), i.e. the data acquisition protocol is very flexible with this system.

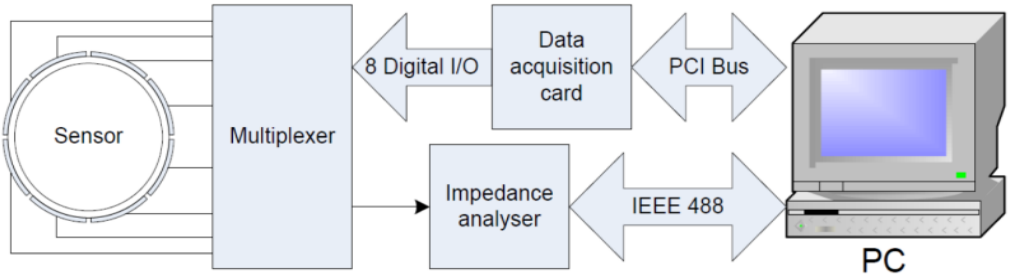

Figure 2.4 An impedance-analyser-based ET system (Yang 2007a)

The impedance analyser used in the system enables the capacitive and resistive components of the impedance to be measured simultaneously, which indicates that the system can be applied for ECT/ERT dual-modality measurement. Hu *et al*. (2008) further extended the use of the system to the mutual inductance measurement between different coil pairs of a planar magnetic sensor. Since the frequency and amplitude of the excitation signal are programmable, the system can also be exploited for spectroscopy or multi-frequency measurement. A MATLAB-based graphical user interface (GUI) was designed for the initial system configuration, data acquisition, image reconstruction and post-processing (Yang 2007a). The performance of the system was evaluated for capacitance, conductance and mutual inductance measurements, and compared with the AC-based ECT system and a Solartron impendence analyser (SL1260) in terms of measured parameter, measurement range and resolution, number of channels, spectroscopy, data acquisition rate and sensing modality by Hu *et al*. (2008). It was concluded that the impedance-analyser-based ET system performs better in most of the aspects, except for that its data acquisition rate is lower than the AC-based ECT system and its resolution is lower than SL1260. The impedance-analyser-based ET system will be used in the experiment of this study.

2.3.2 Hardware for ERT

Boone and Holder (1996) gave a simplified representation of an electrical impedance tomography (EIT) measurement as shown in Figure 2.5 and reviewed the analogue instrumentation design in EIT. They analysed the specific factors in instrumentation, which cause measurement errors in EIT, and suggested the requirements on current source and differential voltage measurement circuit as the most essential parts of EIT instrumentation. They also presented the techniques for the design of the current source,

e.g. two Howland current sources with well-matched component values between them (Jossinet *et al*. 1994), and differential voltage measurement circuit, e.g. the use of an instrumentation amplifier in conjunction with a technique for reducing the common-mode voltage (Toumazou and Lidgey 1989, Trillaud and Jossinet 1992, Zhu *et al*. 1992).

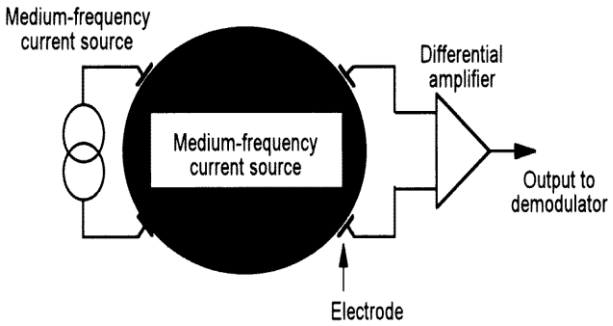

Figure 2.5 A simplified representation of an EIT measurement (Boone and Holder 1996)

Dickin and Wang (1996) described their developed ERT data acquisition system, including the voltage-controlled current source with dual op-amp and positive feedback (Wang 1994), and the use of an instrumentation amplifier (PGA202) with the grounded floating measurement technique to reduce the common-mode voltage (Wang and Dickin 1994). Besides the use of analogue current source, a bi-directional current pulse technique was applied in ERT to simplify the data acquisition system and eliminate the need for demodulation (Cilliers *et al*. 2001). In this study, an ERT experimental system will be established based on some of the techniques reviewed above, which will be described in details in Chapter 4.

2.4 Sensitivity matrix calculation and data normalisation

2.4.1 Sensitivity matrix calculation

Most algorithms for solving the inverse problem of ECT or ERT are based on a sensitivity-matrix, which needs to be calculated first before image reconstruction. The sensitivity vector corresponding to each electrode or electrode pair combination of the sensor in the sensitivity matrix is called a sensitivity map. Each sensitivity map describes the sensitivity of the measured capacitance or potential difference change to

the permittivity or conductivity change inside the sensing domain for the specified electrode or electrode pair combination. For example, an 8-electrode ECT sensor needs 28 sensitivity maps and a 16-electrode ERT sensor needs 104 sensitivity maps. The sensitivity maps for an ECT sensor can be obtained with the following four methods:

(1) geometry dependence (Wajman *et al*. 2004);
(2) perturbation-based measurement (Xie *et al*. 1992, Yang and Conway 1998);
(3) a numerical solution to the electric field (Liu *et al*. 2001);
(4) calculation along electric field lines by analogy to hard-field tomography (Loser *et al*. 2001).

The methods (2) and (3) can generate similar sensitivity maps for an ECT sensor. Wajman *et al*. (2004) gave a brief overview of those four methods and illustrated the reconstruction results with Landweber iteration for three object distributions and different sensitivity maps by those methods. The methods (1) and (4) or (2) and (4) were also combined for the calculation of sensitivity matrix (Kim *et al*. 2006, Kim *et al*. 2007, Zhang and Wang 2009). Among those methods, however, the most convenient and popular one is that by calculation with a numerical solution. With the numerical solution of the electric field, the element in a 2D sensitivity map for an ECT sensor, i.e. the sensitivity of electrode pair $i-j$ to the permittivity change of the pixel at position (x, y) with an area of $P(x, y)$, is defined as (Lionheart 2001, Liu *et al*. 2001):

$$S_{i,j}(x,y) = \int_{P(x,y)} \frac{E_i(x,y)}{V_i} \cdot \frac{E_j(x,y)}{V_j} dx\, dy \quad (i = 1 \ldots N, j = i+1 \ldots N) \quad (2.11)$$

where $E_i(x, y)$ and $E_j(x, y)$ are the electric field strength at (x, y) when the i_{th} and j_{th} electrodes are applied voltages V_i and V_j respectively for excitation in turn, and N is the number of electrodes.

Similarly, the element in the 2D sensitivity maps for an ERT sensor, i.e. the sensitivity of electrode pairs i and j to the conductivity change of the pixel at position (x, y) with an area of $P(x, y)$, is defined as (Dickin and Wang 1996):

$$S_{i,j}(x,y) = \int_{P(x,y)} \frac{E_i(x,y)}{I_i} \cdot \frac{E_j(x,y)}{I_j} dx\, dy \quad (2.12)$$

where $E_i(x, y)$ and $E_j(x, y)$ are the electric field strength at (x, y) when the i_{th} and j_{th} electrode pairs are injected with currents I_i and I_j respectively for excitation in turn.

Before applying reconstruction algorithms, which can be non-iterative or iterative methods as described by Yang and Peng (2003), it is a general practice to normalise the sensitivity matrix to control its level suitable with the normalised measurements for an ECT or ERT sensor, which is completed by the normalisation of sensitivity maps. The sensitivity map $S_{i,j}$ for electrode pair $i - j$ or electrode pairs i and j can be normalised as (Kim *et al*. 2007, Giguère *et al*. 2008):

$$S_{i,j}^{*} = \frac{S_{i,j}}{\sum_{k=1}^{N} S_{i,j}(k)} \tag{2.13}$$

where $S_{i,j}^{*}$ is the normalised sensitivity map for electrode pair $i - j$ or electrode pairs i and j, and $S_{i,j}(k)$ is the sensitivity of electrode pair $i - j$ or electrode pairs i and j to the permittivity or conductivity change of the k_{th} pixel inside the sensor. All the sensitivity maps for possible electrode or electrode pair combinations can be normalised according to equation (2.13), and then integrated to be a normalised sensitivity matrix according to the data collection strategy, which can be used for image reconstruction.

2.4.2 Data normalisation

An ECT system is usually calibrated with a normalisation process based on a low permittivity material and a high permittivity material, which is essential for reconstructing the high and low permittivity material distribution. Three different permittivity models for ECT, i.e. the parallel, series and Maxwell models, were examined by Yang and Byars (1999) and McKeen and Pugsley (2002) to show their influences on image reconstruction using iterative linear-back projection (LBP). It was concluded that the parallel permittivity model gave the best results for all the simulation setups specified (McKeen and Pugsley 2002). Chaplin *et al*. (2005) proposed another model: Bottcher model, but it only gives good measurement results in specified cases, not for general applications. Based on the parallel and series models, a combined model was attempted by Zhang and Wang (2009). Good results can be obtained with all the specified distributions. However, the normalisation process is complicated and time-consuming. Therefore, a normalised capacitance vector based on the parallel permittivity model is usually used for image reconstruction.

In the parallel model, a parallel material distribution was assumed and the normalised capacitance was a linear function of measured capacitance, which can be expressed as (Xie *et al*. 1992):

$$\lambda(i,j) = \frac{C_m(i,j) - C_l(i,j)}{C_h(i,j) - C_l(i,j)} \qquad (i = 1 \dots N, j = i+1 \dots N) \tag{2.14}$$

where N is the number of electrodes, $\lambda(i,j)$ is the normalised capacitance for electrode pair $i-j$, $C_m(i,j)$ is the measured capacitance for electrode pair $i-j$, $C_l(i,j)$ and $C_h(i,j)$ are the capacitances for electrode pair $i-j$ when the sensor is filled with low and high permittivity materials, respectively.

For ERT, the voltage differences measured for image reconstruction are normalised by calculating their relative changes with respect to the reference voltage differences which are obtained when an ERT sensor is filled with the conductive background medium. It can be termed as (Dickin and Wang 1996, Giguère *et al*. 2008):

$$V(i,j) = \frac{V_m(i,j) - V_r(i,j)}{V_r(i,j)} \tag{2.15}$$

where $V(i,j)$ is the normalised change of voltage difference for injection electrode pair i and measurement electrode pair j, and $V_m(i,j)$ and $V_r(i,j)$ are the measured and reference voltage difference for injection electrode pair i and measurement electrode pair j respectively.

2.5 Inverse problem and popular reconstruction algorithms

Solving the inverse problem of ECT or ERT is to obtain the permittivity or conductivity distribution from the measured inter-electrode capacitance or potential differences on the boundary of a sensor. Because the same algorithms can be applied to ECT and ERT to solve their respective inverse problem (Yang and Peng 2003, Giguère *et al*. 2008), the following will discuss ECT only.

Generally, the relationship between the measured inter-electrode capacitance and the permittivity distribution is complicated and non-linear as shown by equation (2.3). To make it simple to implement, the sensing domain of an ECT sensor is normally divided into a large number of small pixels assuming a constant permittivity in each pixel, e.g. 1024 pixels for a square sensor and about 800 pixels for a circular sensor generated by a

32×32 grid. Then a linear approximation can be made between the measured capacitance change and the permittivity change in a discrete form (Yang and Peng 2003):

$$\Delta C = J\Delta\varepsilon \tag{2.16}$$

where $\Delta C \in \mathbb{R}^M$ is a vector of the measured capacitance change, $\Delta\varepsilon \in \mathbb{R}^N$ is a vector of the permittivity change, $J \in \mathbb{R}^{M\times N}$ is a Jacobian matrix, i.e. the sensitivity matrix before normalisation, M is the number of independent measurements, and N is the number of pixels defined inside the sensing domain. This linear approximation is only valid when the permittivity perturbation is small. In its normalised form, equation (2.16) is generally rewritten as:

$$\lambda = S^* g \tag{2.17}$$

where $S^* \in \mathbb{R}^{M\times N}$ is the normalised sensitivity matrix, $\lambda \in \mathbb{R}^M$ is the normalised capacitance vector, $g \in \mathbb{R}^N$ is the normalised vector of the grey scalar image of the permittivity distribution. For ERT, a similar linear equation can be generated to describe the relationship between the normalised change of inter-electrode potential difference and the normalised conductivity change (Giguère *et al*. 2008). To reconstruct the permittivity distribution g from the measured capacitance λ, equation (2.17) needs to be solved while the sensitivity matrix S^* is assumed to be constant in most cases. Note that the sensitivity matrix S^* changes with the permittivity distribution due to the "soft-field" effect. If the inverse of the sensitivity matrix S^* can be obtained, the permittivity distribution g can be expressed as:

$$g = (S^*)^{-1}\lambda \tag{2.18}$$

However, the analytical inverse of S^* does not exist because the number of unknowns or pixels N is much larger than the number of independent capacitance measurements M, which means that S^* is not a square matrix and the solution to equation (2.17) is not unique. Another challenge associated with equation (2.17) is that it is ill-conditioned. It means that a small perturbation in λ may induce a very large change in the solution of g. As a result, numerical techniques are usually used to derive the approximation of $(S^*)^{-1}$ and deal with the ill-conditioning of equation (2.17). The choice of the approximation of $(S^*)^{-1}$ in equation (2.18) results in different image reconstruction

algorithms as summarised by Giguère *et al*. (2008). In general, the reconstruction algorithms can be classified into two categories: non-iterative and iterative algorithms.

2.5.1 Non-iterative algorithms

Linear-back projection (LBP)

Non-iterative algorithms are single step reconstruction methods, among which the simplest and most popular one is the linear-back projection (LBP) algorithm. In LBP, the transpose of the sensitivity matrix is used to approximate its inverse and the normalised form of the algorithm can be formulated as (Yang and Peng 2003):

$$\hat{g} = \frac{S^T \lambda}{S^T \mu_\lambda} \tag{2.19}$$

where $\hat{g}$ is the approximated solution of equation (2.17), S is the sensitivity matrix of an ECT sensor, S^T is the transpose of S, λ is the normalised capacitance vector, and μ_λ is the identity vector, i.e. $\mu_\lambda = [1,1,1, \dots ,1]$. Although the LBP algorithm can only give qualitative image, it finds wide application in online reconstruction and measurement because it is simple and less computationally intensive.

Singular value decomposition (SVD)

If the measurement noises are considered, equation (2.17) is rewritten as

$$Sg = \lambda + e \tag{2.20}$$

where e is the measurement noise vector.

To solve equation (2.20), it is a common practise to minimise the L_2 norm $\frac{1}{2}||Sg - \lambda||^2$, which gives:

$$S^T S g = S^T \lambda \tag{2.21}$$

Because the inverse of $S^T S$ does not exist, the equation (2.21) cannot be solved directly (Yang and Peng 2003). Based on singular value decomposition (SVD) analysis, the sensitivity matrix for an ECT sensor can be expressed as:

$$S = U \Sigma V^T \tag{2.22}$$

where

$$U = [u_1, u_2, \dots, u_M] \, , V = [v_1, v_2, \dots, v_N]$$

$$\Sigma = diag[\delta_1, \delta_2, \dots, \delta_p] \tag{2.23}$$

U is an $M \times M$ orthogonal matrix, V is an $N \times N$ orthogonal matrix, Σ is an $M \times N$ diagonal matrix with the non-zero elements p singular values of S ($\delta_1 \geq \delta_2 \geq \cdots \geq \delta_{p-1} \geq \delta_p > 0$), M is the number of independent measurements, N is the number of pixels in the reconstructed image, and p is the rank of S.

The so-called pseudo-inverse of S (an approximation of S^{-1}) can now be represented by $V\Sigma^{-1}U^T$, where

$$\Sigma^{-1} = \ diag[\tfrac{1}{\delta_1}, \tfrac{1}{\delta_2}, \dots, \tfrac{1}{\delta_p}] \tag{2.24}$$

and the approximated solution of equation (2.17) or (2.20) in the least square sense can be expressed as:

$$\hat{g} = V\Sigma^{-1}U^T\lambda \tag{2.25}$$

Because the inverse problem for ECT is ill-posed, this solution is not unique and can only be accepted mathematically (Yang and Peng 2003). As suggested by Pan and Yagle (1992), Polydorides and McCann (2002) and Tang *et al*. (2002), the largest singular values of S mainly contribute to the main features (lower "spatial" frequency components) of the reconstructed image, while the smallest ones to the detailed features (higher "spatial" frequency components). Since S is severely ill-conditioned, its smallest singular values are nearly zero and have the minimum effect on the sensitivity. However, they are very vulnerable to noises in the measured data. It means that it is essential to eliminate the noises and to reduce the influences of measurement noises on the reconstruction. For this purpose, truncated singular value decomposition (TSVD) can be applied (Polydorides and McCann 2002). The basic principle of TSVD is described by Yang and Peng (2003) that a spectral filter is included in the conventional SVD to lower the sensitivity of the reconstruction to high-frequency noise in the measurement. This idea can be extended for generalised filtering solution of equation (2.17) or (2.20), which is defined as (Lionheart 2001, Yang and Peng 2003):

$$\hat{g} = Vf(\delta)\Sigma^{-1}U^T\lambda \tag{2.26}$$

where $f(\delta)$ is the spectral filter with $\delta = \Sigma$ for simplicity. The choice of $f(\delta)$ leads to different algorithms.

Tikhonov regularisation

Because the image reconstruction for ECT is an ill-posed inverse problem, regularisation tools can be used to find a regularised solution. Some additional assumptions and prior information about the material distribution must be added as constraints to an optimisation problem associated with equation (2.17) or (2.20). As a popular regularisation tool, Tikhonov regularisation has been applied to solve the ill-posed inverse problem for ECT (Peng *et al*. 2000, Lionheart 2001). If the spectral filter in equation (2.26) is chosen to be (Lionheart 2001, Yang and Peng 2003):

$$f(\delta) = \frac{\delta^2}{\delta^2+\mu} \tag{2.27}$$

where μ is the regularisation parameter, which must be positive and is determined empirically in most cases. The standard Tikhonov regularisation solution of equation (2.17) or (2.20) can then be formulated as:

$$\hat{g} = (S^TS + \mu I)^{-1}S^T\lambda \tag{2.28}$$

where I is an identity matrix. Equation (2.28) seems the approximated solution of the modified problem of equation (2.21) by changing S^TS into $S^TS + \mu I$ to make the inverse exist. The more general Tikhonov regularisation has been discussed by Lionheart (2001) with a more generalised SVD filter method.

Other non-iterative reconstruction techniques for ECT have also been reported, e.g. the multiple linear regression and regularization method (Yan *et al*. 2001), the Calderon's method (Cao *et al*. 2009 and 2011a), the dbar method (Cao *et al*. 2010), the enclosure method (Cao and Xu 2011), and the factorization method (Cao *et al*. 2011b, Cao and Xu 2013).

2.5.2 Iterative algorithms

Non-iterative reconstruction algorithms can provide qualitative images only, because they are based on the simplified linear model of ECT and the relationship between permittivity and capacitance is actually non-linear. As reported in the literature, iterative algorithms are generally adopted to reconstruct quantitative images since the discrepancy between the measured capacitance and the estimated capacitance from the current image is used to modify the reconstruction iteratively until it is sufficiently small. As discussed previously, different solvers for the forward problem of ECT can be used to estimate the capacitance, e.g. FEM and sensitivity matrix-based method. Meanwhile, different methods, e.g. based on the optimisation theory, can be applied to rectify the image with the discrepancy between the measured and calculated capacitances. The choice of the forward solver and image rectification method leads to different algorithms. Generally, iterative algorithms are more computationally intensive than non-iterative ones and only applied for off-line application.

Landweber iteration

Landweber iteration method (Yang *et al*. 1999) is derived from the steepest gradient descent method in the optimisation theory. With the image rectification method similar to the LBP in each iteration, it can be expressed as (Yang and Peng 2003):

$$g_{k+1} = g_k - \alpha_k S^T(Sg_k - \lambda) \tag{2.29}$$

where g_k and g_{k+1} are the normalised permittivity vector for k_{th} and $k+1_{th}$ iteration, α_k is the gain or relaxation factor, which is used to determine the convergence rate. Note that Sg_k is used to estimate the capacitance of the current image g_k. Actually, equation (2.29) can also be derived by replacing the spectral filter in equation (2.26) with (Lionheart 2001):

$$f(\delta) = 1 - (1 - \alpha_k \delta^2)^k \tag{2.30}$$

To improve the convergence rate, a modified Landweber iteration is (Yang and Peng 2003):

$$g_{k+1} = P[g_k - \alpha_k S^T(Sg_k - \lambda)] \tag{2.31}$$

where P is a projection operator and

$$P[f(x)] = \begin{cases} 0 & if\ f(x) < 0 \\ f(x) & if\ 0 < f(x) < 1 \\ 1 & if\ f(x) > 1 \end{cases} \quad (2.32)$$

In the iteration process, the relaxation factor α_k can keep constant or be updated in each iteration step as discussed by Peng *et al*. (2000) and Liu *et al*. (1999). To start the Landweber iteration process, the initial permittivity distribution g_0 is normally reconstructed by LBP. Even though it is popular, the Landweber method suffers from its semi-convergence behaviour (Yang and Peng 2003, Hansen and Saxild-Hansen 2012). The image error would decrease in the initial stage. After a certain number of iterations, however, it would increase. Therefore, it is essential to stop after an appropriate number of iterations for convergence of the reconstruction with the Landweber method.

Algebraic reconstruction technique (ART)

ART has been applied to ECT for image reconstruction by Reinecke and Mewes (1996). Unlike the Landweber iteration, it is a row-action method and treats the projection data one at a time during the iterations. ART can be formulated as:

$$g_k = g_{k-1} - \frac{(S_k g_{k-1} - \lambda_k)}{S_k S_k^T} \cdot S_k^T \quad (2.33)$$

where g_k and g_{k-1} are the results for k_{th} and $k - 1_{th}$ iteration, S_k is the k_{th} row vector of the sensitivity matrix S, and λ_k is the k_{th} normalised capacitance from the measured capacitance vector.

The drawback of ART lies in that it is sensitive to noises in the measured capacitance since only one projection data is involved in each iteration (Yang and Peng 2003). To overcome this problem, simultaneous iterative reconstruction technique can be applied (Su *et al*. 2000), which is also a type of descent gradient method and has similar performance as the Landweber method regarding the quality of the reconstructed image.

Other iterative reconstruction algorithms for ECT or ERT have also been reported, including:

(1) Newton-Raphson and modified Newton-Raphson (Yang and Peng 2003);

(2) Krylov subspace (i.e. conjugate gradient) (Wang 2002 and Wang *et al*. 2005);
(3) Hybrid by combining the Tikhonov regularisation and Landweber method (Lionheart 2001);
(4) Model-based iteration (Isaksen and Nordtvedt 1993, Khambampati *et al*. 2012);
(5) Reconstruction with iteratively updated sensitivity matrix or non-linear forward solver (Li and Yang 2008, Xue *et al*. 2012, Marashdeh *et al*. 2006a and 2006b, Banasiak *et al*. 2010);
(6) Non-linear reconstruction with total-variation regularisation (Fang 2004, Soleimani and Lionheart 2005).

2.5.3 Evaluation of algorithms

Three criteria can be employed to evaluate the performance of reconstruction algorithms, which are relative image error, capacitance residual and correlation coefficient between the true image and the reconstructed image (Peng *et al*. 2000, Yang and Peng 2003).

$$RIE = \frac{\|\hat{g}-g\|}{\|g\|} \tag{2.34}$$

$$CR = \frac{\|\lambda - S\cdot\hat{g}\|}{\|\lambda\|} \tag{2.35}$$

$$CC = \frac{\sum_{i=1}^{N}(\hat{g}_i-\bar{\hat{g}})(g_i-\bar{g})}{\sqrt{\sum_{i=1}^{N}(\hat{g}_i-\bar{\hat{g}})^2\sum_{i=1}^{N}(g_i-\bar{g})^2}} \tag{2.36}$$

where RIE is the relative image error, CR is the capacitance residual, CC is the correlation coefficient, λ is the normalised capacitance vector, S is the sensitivity matrix of the sensor, g is the true permittivity distribution, $\hat{g}$ is the reconstructed permittivity distribution, $\bar{\hat{g}}$ and $\bar{g}$ are the mean values of g and $\hat{g}$ respectively.

These three criteria can be used to compare the quality of reconstructed images by different algorithms with respect to the same permittivity distribution. The better image quality means smaller relative image error and capacitance residual as well as larger correlation coefficient. However, smaller capacitance residual does not necessarily guarantee better images.

2.6 Summary

This chapter presented a brief review of the fundamentals of ECT and ERT, mainly regarding their basic principles, data acquisition systems, and the forward and inverse problems. An ECT or ERT sensor generally has a certain number of electrodes in a ring around the exterior or interior periphery of a pipe section. According to the specified measurement protocol, an AC signal is applied to the sensor for excitation and the resultant responses can be measured through suitable hardware. Finally, an image can be reconstructed with an appropriate reconstruction algorithm based on the acquired data. To do the image reconstruction, the forward problem needs to be solved by FEM or other methods for the electric potential distribution inside the sensor, which can be used to calculate the relevant sensitivity maps, and capacitance/resistance values with the specified permittivity/conductivity distribution. To solve the inverse problem, i.e. reconstruct an image from the measured or simulated impedance data, various non-iterative or iterative algorithms (e.g. LBP and Landweber iteration) can be applied, the performance of which can be evaluated with certain criteria.

The governing equations for the electric field in ECT and ERT are similar except for different boundary conditions. This indicates that the corresponding solutions to the forward problems are different from each other. The same algorithms can be used to solve the inverse problems for ECT and ERT. Non-iterative algorithms are fast but can only give qualitative images, while iterative algorithms can reconstruct quantitative images but are usually computationally intensive. Because the inverse problems for ECT and ERT are non-linear in nature, non-linear iterative algorithms, e.g. with updated sensitivity matrix or non-linear forward solver, can improve the quality of reconstructed images. By incorporating more prior knowledge in the reconstruction, the image quality can also be improved, e.g. model-based and regularisation-based methods. To reduce the time consumption of image reconstruction, especially by nonlinear iterative algorithms, parallel computing based on graphics processing units (GPU) may be applied to implement the algorithms.

Chapter 3: Fringe effect of ECT and ERT sensors due to their sensor design

This chapter will discuss the fringe effect of ECT and ERT sensors due to the limited length of electrodes and the use of grounded end guards. The voltage-excitation strategy and the grounded guards are adopted for ERT so that the fringe effect can be minimised and ECT and ERT sensors can be integrated together to optimise an ECT/ERT dual-modality measurement.

3.1 Introduction

As discussed in Chapter 1, the fringe effect will occur to the both ends of electrodes for ECT and ERT sensors with limited electrode length, i.e. the electric field is axially non-uniform and spreads to a large volume outside the supposed sensing plane. The fringe effect results in that: (1) the sensitivities of the sensor are not uniform along the axial direction (Yan *et al*. 1999, Peng *et al*. 2005); (2) the sensor can sense and reconstruct the objects outside the imaging volume of interest, which are not supposed to appear in the reconstructed 2D image (Yan *et al*. 1999). The above discussion implies that the fringe effect of ECT and ERT sensors is complicated and subject to the sensor design and axial material distribution inside the sensing volume of the sensor.

As mentioned in Chapter 1, the fringe effect would be minimal for an ECT sensor under two conditions: (1) sufficient long measurement electrodes and appropriate guards; (2) axially uniform permittivity distribution. In this chapter, the axial permittivity distribution is assumed to be uniform to exclude its influence on the fringe effect. Sufficient long measurement electrodes can ensure the axial electric field distribution of the sensor to be approximately uniform, while the guards can help constrain the electric field distribution to the electrode plane. Grounded end guards has been applied in ECT sensors (Yan *et al*. 1999, Peng *et al*. 2005, Alme and Mylvaganam 2006b) and proved to be effective in narrowing the axial sensing range (Yan *et al*. 1999). In contrast, driven guard electrodes may be used below and above measurement electrodes in the axial direction to reduce the fringe effect (Ma *et al*. 1997, Yan *et al*. 1999, Ma *et al*. 1999). Although some simulation and experimental results seem promising, the effectiveness of driven guards was suspected (Wang 1999, Alme and Mylvaganam 2006b, Yang

2010). From these points of view, it is necessary to investigate the impact of electrode length and grounded end guards on the fringe effect.

In this chapter, the fringe effect of ECT and ERT sensors with variable electrode length is quantified against the corresponding 2D models (used as references) for both symmetric and non-symmetric object distributions. Voltage-excitation for ERT will be discussed preceding the quantification process of fringe effect in ERT sensors. Image reconstruction will be implemented based on the previous results to investigate the impact of fringe effect. Grounded guard electrodes will be evaluated to see its effectiveness for reducing the fringe effect. The feasibility of voltage-excitation for ERT will be verified by experiment. Finally, a common structure will be proposed for ECT and ERT sensors to reduce their fringe effect and integrate the two types of sensors together for dual-modality measurement.

3.2 Fringe effect of ECT sensors with voltage-excitation

It was suggested that the optimal length of electrodes in an ECT sensor should be the same as the inner diameter of a round-shape pipe or vessel or the width of square-shape pipe or vessel (Peng *et al*. 2005). This conclusion is merely qualitative, without quantitative verification. From the application point of view, it is desired to use shorter electrodes to achieve a narrower sensing range. Therefore, it is necessary to investigate the fringe effect on the normalised capacitance when the electrode length is much shorter than the dimension of the pipe or vessel diameter. It is also necessary to investigate to what extent the fringe effect would distort the reconstructed images. For those purposes, 3D simulation for ECT sensors with different electrode lengths, with or without guard electrodes, were carried out. Because the frequency of the excitation signal for ECT is in the order of 100 kHz to 1 MHz, the corresponding wavelength is larger than the sensor size by several orders of magnitudes. This means the potential distribution inside an ECT sensor can be approximated by the electrostatic field. This assumption is also applicable to ERT sensors. Thus the electrostatic mode in COMSOL Multiphysics is adopted for the simulation of ECT sensors and the conductive media DC mode for simulation of ERT sensors, as described in Chapter 2.

3.2.1 Simulation models for ECT sensors without grounded end guards

An ECT sensor without end guards and the object distribution for simulation are shown in Figure 3.1.

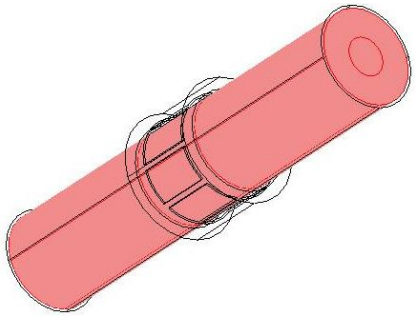

(a) 3D sensor model without end guards

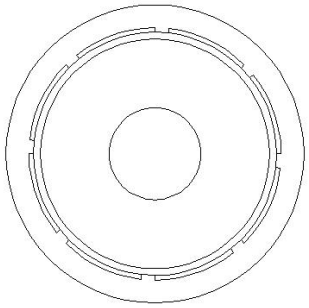

(b) 2D sensor model with object distribution

Figure 3.1 2D and 3D ECT sensor models without end guards

Some parameters of the ECT sensor model are:

- Diameter: 10 cm
- Electrode size: 35 mm × 30 mm × 2 mm
- Thickness of pipe wall: 3 mm
- Distance between shield and electrodes: 10 mm

While different electrode lengths are used to evaluate the fringe effect, the length of shield is always chosen to be 3 cm longer than that of electrodes to ensure the validation of modelling. Note that any object distribution simulated in this chapter is always axially uniform.

For calibration purpose, the ECT sensor is first filled with air ($\varepsilon_r = 1$) as the lower reference, and then material of relative permittivity 3.0 as the higher reference. Note that the object to be imaged in Figure 3.1 (b) has a relative permittivity of 3.0. To measure the capacitance, each time one electrode is applied a voltage and all other electrodes are kept at ground potential for detection. This process is repeated until all possible electrode pairs are measured, i.e. all independent measurements are taken.

To ensure numerical accuracy (i.e. the difference in normalised capacitance between a mesh and a finer mesh is below 2%), the mesh density is increased until the simulated

capacitance or conductance after normalisation converges. At the same time, the length of the pipe is increased in different cases until it has almost no influence on simulation results. In the simulation, tetrahedral type of elements and direct solver (SPOOLES) are used. The number of elements in each case is in the order of 100,000. Take the ECT sensor model as shown in Figure 3.1 (a) with an electrode length of 12 cm as an example to show the influence of mesh size on simulation. The first coarse mesh consists of 66,549 tetrahedral elements, and a finer one consists of 112,736 elements, which are shown in Figure 3.2 (a) and (b) respectively. Note that, in these two meshes, a denser mesh is generated close to the electrodes of the sensor.

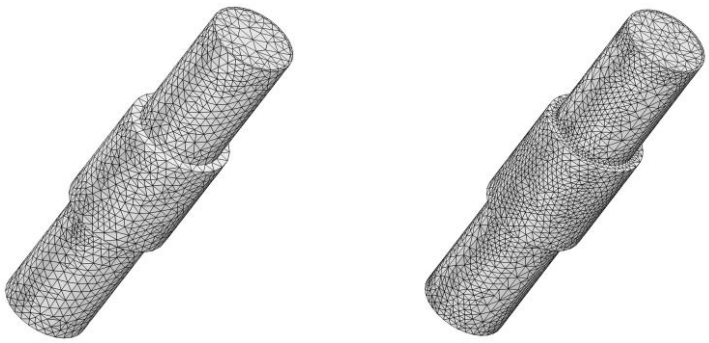

(a) Coarse mesh (b) Fine Mesh

Figure 3.2 Meshes

The simulated capacitance values after the normalisation with the two meshes have the maximum difference of 1.1%, as shown in Figure 3.3 (a), with the first 7 values of a whole measurement frame. Note that all simulation was done on a PC with an Intel CoreTM i7-2600 3.4 GHz CPU, 64-bit Windows 7 Operation System and 8 GB memory. In the simulation, the thickness of electrodes is 2 mm, which is larger than reality (around 1 mm or less), and it affects the simulation results slightly. This can be verified by comparing the simulated capacitance after normalisation when the thicknesses of electrodes are 2 mm and 1 mm, respectively. The first 7 values in both cases are shown in Figure 3.3 (b). The difference in normalised capacitance between these two cases is below 2%.

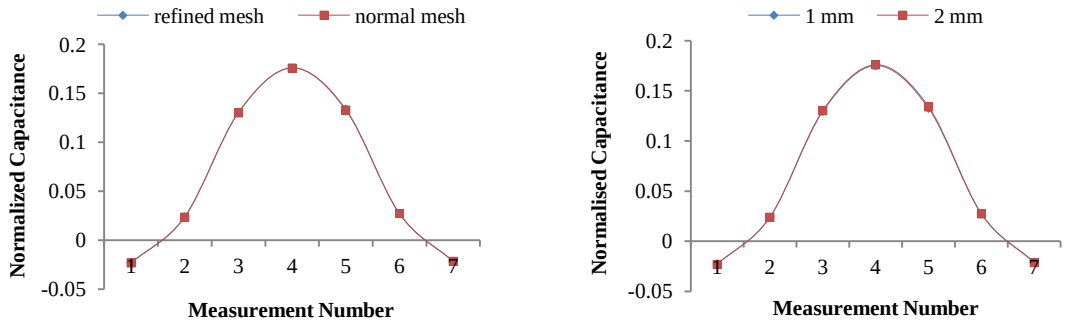

(a) With different meshes (b) With different electrode thickness

Figure 3.3 Comparison between normalised capacitance obtained with different meshes or different electrode thicknesses

3.2.2 Simulation results for ECT sensors without end guards

The ECT sensor model used in this part is the same as shown in Figure 3.1 (a). By exciting each electrode in the sensor in turn, the resultant electric potential distributions when the sensor is filled with air can be obtained by simulation using FEM in COMSOL Multiphysics. Using the post-processing function in COMSOL Multiphysics, the axial potential distributions for the above ECT sensor model with two different electrode length, i.e. 1 cm and 12 cm, are calculated and shown in Figure 3.4. Note that different colour represents different potentials, e.g. red for 1 V and dark blue for 0 V as shown in the colour bar. Figure 3.4 actually shows the axial distributions of equi-potential lines in the two cases. Note that the negative gradient of the electric potential distribution generates the electric field distribution.

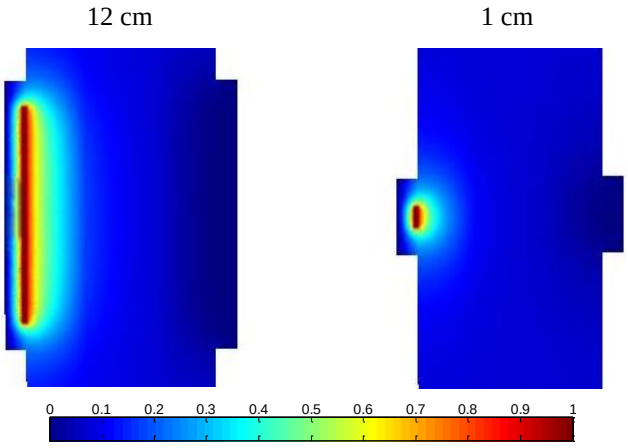

Figure 3.4 Axial electric potential distribution for ECT sensors with two different electrode lengthes

From Figure 3.4, the fringe effect of the ECT sensors with different electrode lengths can be seen qualitatively. It is obvious that the long electrodes can generate more uniform axial field distribution, as indicated by the fact that more equi-potential lines are almost in parallel with the axis of the sensor. In this case, the 3D field distribution can be simplified to 2D. This means that an ECT sensor with long electrodes (12 cm) presents less fringe effect than that with short electrodes (1 cm). The non-uniform axial field distribution in the case of pin electrodes would cause a non-uniform axial sensitivity distribution, because the sensitivity at certain point inside the sensor is closely related to the 3D electric field distribution generated by exciting one of the electrodes (Peng *et al*. 2005). This non-uniform sensitivity distribution would further cause different responses from the sensor when the same object is placed at different axial positions inside the sensor, as described in (Wang 1999).

Besides the sensitivity distribution, an essential factor for image reconstruction affected by the fringe effect is the normalised capacitance because the absolute inter-capacitance between an electrode pair is related to the electric field distribution. Therefore, the normalised capacitance for 3D ECT sensor models with different electrode lengths is compared with their 2D reference to see the fringe effect quantitatively. The normalisation procedure is the same as described previously in Chapter 2.

The first 7 capacitance values after normalisation of a whole measurement frame for the 3D sensor models are shown in Figure 3.5, indicating that the normalised capacitance becomes closer and closer to their 2D reference when the length of electrodes increases. This phenomenon can also be observed from the images reconstructed using the normalised capacitance and the 2D sensitivity maps calculated as described in Chapter 2 where the 2D ECT sensor model in Figure 3.1 (b) is used with the sensing domain filled with a low permittivity material. The reconstructed images using LBP are shown in Figure 3.6. Note that the white circle in figures indicates the location of the tube wall in the image, the inner of which is the domain of interest.

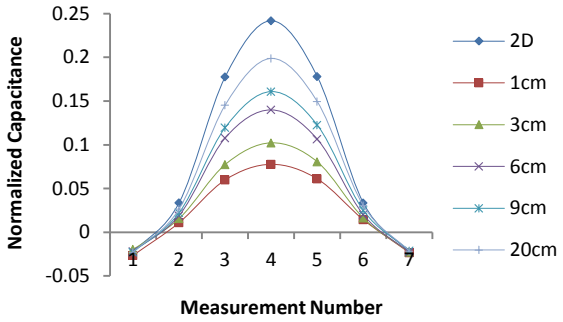

Figure 3.5 Comparison between normalised capacitance for 2D and 3D ECT sensor models with different electrode length and without end guards

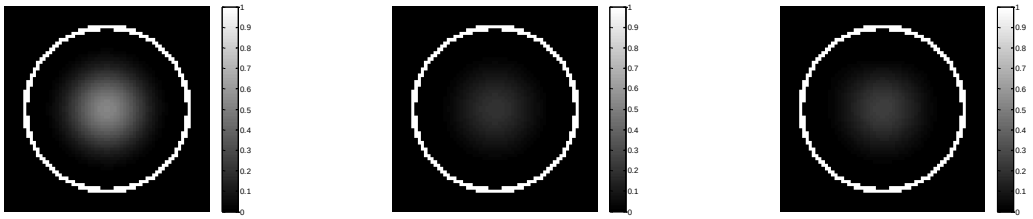

(a) 2D ECT model

(b) 3D ECT model with 1 cm electrodes

(c) 3D ECT model with 3 cm electrodes

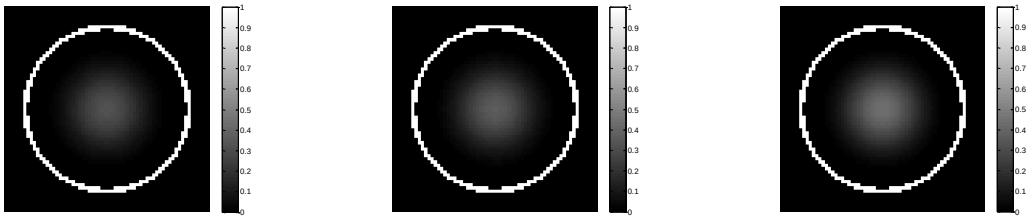

(d) 3D ECT model with 6 cm electrodes

(e) 3D ECT model with 9 cm electrodes

(f) 3D ECT model with 20 cm electrodes

Figure 3.6 Reconstructed images of distribution in Figure 3.1 (b) for 2D and 3D ECT models with different electrode length and without end guards

In Figure 3.6, the reconstructed images become more and more similar to the 2D result when the electrode length increases. To evaluate the image error induced by the fringe effect, the reconstructed image for the 2D ECT sensor model is used as the reference image, and the relative image errors of Figure 3.6 (b)~(f) are calculated as described in Chapter 2 and shown in Figure 3.7. It shows that the relative image errors of the 3D models decrease with the increase in electrode length. This means that the fringe effect is reduced when longer electrodes are used.

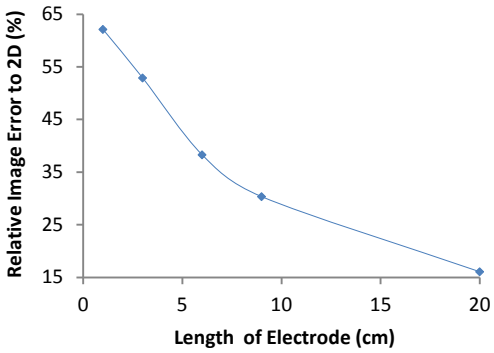

Figure 3.7 Relative image errors of reconstruction results for 3D ECT models with different electrode length and without end guards regarding the 2D one

However, the difference between the 3D normalised capacitance and the 2D one is still large (maximum 25%) even when the length of electrodes is twice the inner diameter of the pipe (10 cm). From this point of view, the 3D normalised capacitance will approach to the 2D one, only after the electrode length becomes infinite relative to the inner diameter of the pipe, because of the electric field distortion at both ends of the sensor and the effect of the objects outside the sensor on the capacitance measurement, even though the uniformity of axial electric field distribution inside the sensor has been improved to a large extent.

3.2.3 Simulation models and results for ECT sensors with end guards

In practice, grounded guards are always used at both ends of an ECT sensor, with which the sensor would have the narrower sensing range in the axial direction (Yan *et al*. 1999) and the fringe effect would be reduced. To investigate the fringe effect of ECT sensors with grounded guards at both ends, simulation was carried out. The 3D simulation model is shown in Figure 3.8.

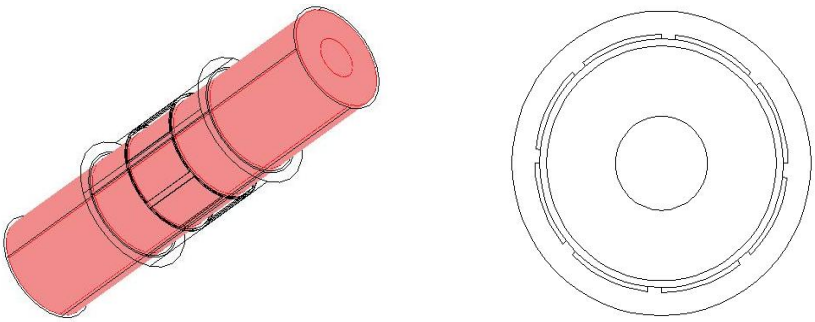

(a) 3D sensor model with end guards

(b) 2D sensor model with object distribution

Figure 3.8 2D and 3D ECT sensor models with grounded end guards

Some parameters of the 3D ECT sensor model with grounded end guards are:

- Thickness of end guard: 2 mm
- Length of end guard: 50 mm
- Gap between end guard and electrode: 1 mm

Other parameters of this 3D ECT sensor model are the same as the previous one except for the length of shield, which is equal to the sum of electrode length, end guard length and the gap between them. The length of end guards is chosen to be half the sensor diameter as Peng *et al*. (2005) suggested that this is the optimal length to reduce the fringe effect. Similar simulation and calibration were carried out. For qualitative illustration of the fringe effect in ECT sensors with grounded end guards, the axial electric potential distribution for the ECT sensors with 9 cm long electrodes and with or without grounded end guards are shown in Figure 3.9 for comparison.

As mentioned previously, grounded end guards would help narrow the axial sensing range of an ECT sensor, i.e. the axial range of the electric field distortion (represented by the equi-potential line distortion) at both ends of the sensor would be reduced, as shown in Figure 3.9. Figure 3.9 also shows that the uniformity of axial electric field distribution (represented by the number of equi-potential lines almost in parallel with the axis of the sensor) in this case is changed slightly compared to that for the sensor without end guards. This combination of uniform axial electric field distribution and confined axial sensing range makes it permissible to approximate the 3D electric field

distribution within the sensing volume by the corresponding 2D distribution with less error caused by the fringe effect.

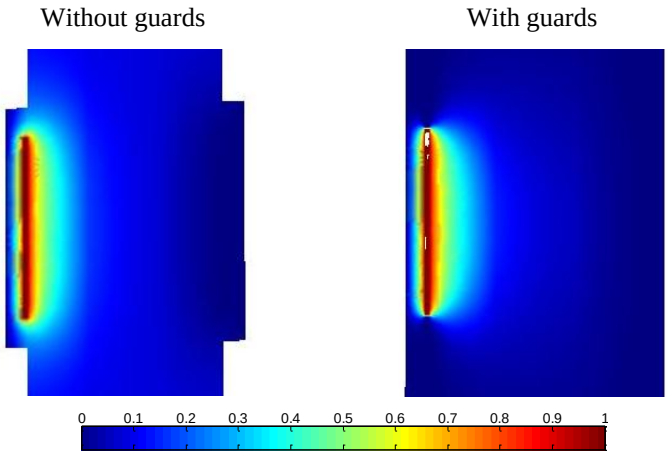

Figure 3.9 Axial electric potential distribution for ECT sensors with 9 cm long electrodes and with or without grounded end guards

Similar to the previous discussion, the first 7 capacitance values after normalisation of a whole measurement frame for the 3D ECT sensor models are obtained and shown in Figure 3.10, in comparison to the 2D reference. By comparing Figure 3.5 and Figure 3.10, it can be concluded that the normalised capacitance for each specified electrode length is closer to the 2D reference when the grounded guards are applied, i.e. the grounded guards can reduce the fringe effect in the normalised capacitance, even though the electric field would be slightly distorted at both ends of the sensor in this case. Images are reconstructed using the normalised capacitance and the sensitivity maps for the 2D ECT model. The reconstructed images using LBP are shown in Figure 3.11. It shows that the reconstructed images with the 3D ECT models become more and more similar to the 2D result as well, when the electrode length increases, and each is more similar to the 2D one than the reconstruction with the corresponding 3D ECT model without end guards, as discussed previously.

Similar to the previous subsection, the reconstructed image with the 2D ECT sensor model is used as the reference image, and the relative image errors of Figure 3.11 (b)~(f) are calculated and shown in Figure 3.12. From Figure 3.12, it can be seen that when grounded end guards are applied, the relative image errors for the 3D sensor models are much less than their counterparts in Figure 3.7, and also decrease with the

increase in the electrode length. This indicates that longer electrodes and grounded end guards should be combined together to reduce the fringe effect in ECT sensor design.

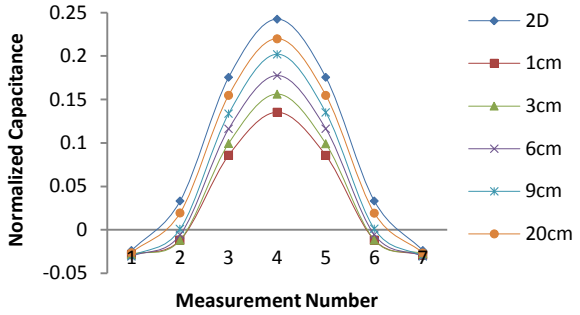

Figure 3.10 Comparison between normalised capacitance for 2D and 3D ECT sensor models with end guards and different electrode lengths

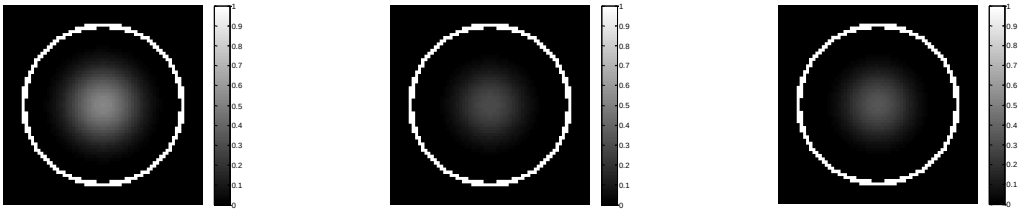

(a) 2D ECT model

(b) 3D ECT model with 1 cm electrodes

(c) 3D ECT model with 3 cm electrodes

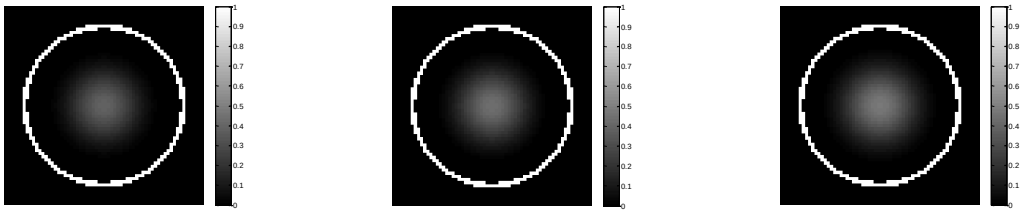

(d) 3D ECT model with 6 cm electrodes

(e) 3D ECT model with 9 cm electrodes

(f) 3D ECT model with 20 cm electrodes

Figure 3.11 Reconstructed images of the distribution in Figure 3.8 (b) for 2D and 3D ECT models with different electrode lengths and end guards

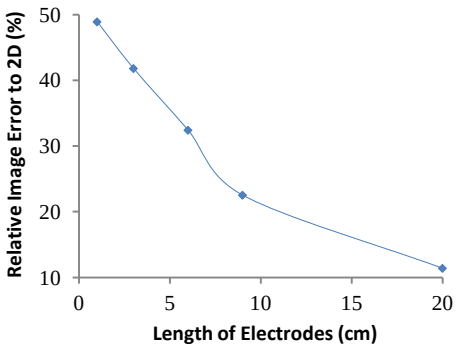

Figure 3.12 Relative image errors for 3D ECT models with different electrode length and end guards regarding the 2D one

3.3 Fringe effect of ERT sensors with voltage-excitation

Sun and Yang (2011) reported that the electric field distribution along the axial direction of an ERT sensor is extremely non-uniform, which leads to the large difference between 2D and 3D simulation results before normalisation, i.e. large "absolute" fringe effect. This was confirmed by Ma *et al*. (1997), Fransolet *et al*. (2002) and Alme and Mylvaganam (2006a), as discussed in Chapter 1. It is critical to reduce the fringe effect of ERT sensors so that the 3D electric field distribution can be simplified into 2D. To achieve this with axially uniform object distribution, two steps are needed: (1) improving the uniformity of electric field distribution along the axial direction of ERT sensors and (2) confining the axial sensing range of ERT sensors. Similarly, the first step can be accomplished by increasing the length of electrodes, and the second step by applying grounded end guards. The reason for the use of grounded end guards in ERT sensors is that the driven guards proposed by Ma *et al*. (1997 and 1999) were proved to be less effective by Wang (1999), since there was no evidence that the sensing range of an ERT sensor with driven guards was narrowed compared to the normal one without guards. However, a conventional ERT sensor does not allow people to do so. Thus the first subsection of this section will illustrate the reason and discuss the change needed for ERT sensors to apply the grounded end guards. Then, the effectiveness of long electrodes and grounded end guards on reducing the fringe effect in ERT sensors will be presented.

3.3.1 ERT sensor with voltage-excitation

In the previous section, it has been suggested that grounded end guards can reduce the fringe effect in an ECT sensor, but it is not applicable to ERT sensors when current-injection is adopted because part of the injected current would flow from the injection electrode to the ground directly.

To apply the grounded end guards in an ERT sensor, voltage-excitation (similar to ECT) can be adopted since the electric fields of ECT and ERT sensors are governed by Laplace equations with exchangeable coefficients but different boundary conditions, which indicates that they are similar to each other if both ERT and ECT sensors are excited by voltage signals and measured with the same strategy or protocol. The application of voltage-excitation in ERT was claimed by Lidgey *et al*. (1992) and Hartov *et al*. (2002), but the voltage signal was applied to generate their desired current patterns. It means that these systems are still current-excited. Jia *et al*. (2010) reported the use of a voltage source and current sensing in an ERT system to output a current with large amplitude (more than 300 mA) to highly conductive flows for more accurate measurement. However, in principle this is still the conventional current-injection strategy.

There are two main reasons for the popularity of current-injection for ERT. The first one is the consideration of safety for human body since ERT was originated for detection of diseased human organs of unknown conductance, and the applied current must be within the safety range. For most industrial applications, however, this is no longer the case. The second reason is the influence of contact impedance between the electrodes and human skin or electrolyte on the conductance measurement. This can be ignored in the case of current-injection with proper measurement electronics, but much more significant in the case of voltage-excitation, as less optimal for ERT measurement than current-injection (Saulnier *et al*. 2006).

To reduce this influence, there are two possible solutions. The first one is the combination of four-electrode and two-electrode impedance measurement techniques to measure the contact impedance directly, as described by Cardu *et al*. (2012). The second one is the use of capacitive-coupled conductivity detection method to avoid direct contact of electrodes and electrolyte and reduce the influence of the contact impedance

by parallel or series resonance (Shih *et al*. 2006, Huang *et al*. 2009) or by increasing the coupling capacitance between the sensor and the electrolyte (Wang *et al*. 2010, Hayes *et al*. 2012). With these solutions, ECT and ERT measurements can potentially be taken by just using one common sensor. Similarly, with voltage-excitation, ECT and ERT sensors can share a common structure to reduce their fringe effect, which is another reason why the voltage-excitation (not current-injection) is chosen for ERT. Some experimental results for the verification of ERT with the voltage-excitation will be presented in section 3.5.

3.3.2 Simulation models and results for ERT sensors without end guards

Based on previous discussion, it is assumed that the influence of the contact impedance can be minimised as some promising results using the above solutions have been obtained. Because the main purpose of this section is to evaluate the effectiveness of grounded end guards on the reduction of the fringe effect in ERT sensors with voltage-excitation, the fringe effect of an ERT sensor without guards is investigated first. 2D and 3D ERT sensor models without guards are shown in Figure 3.13, and each sensor is made up of 12 electrodes. Note that the contact impedance is not included in the sensor models. Some parameters of the 3D ERT sensor model are:

- Diameter: 10 cm
- Electrode size: 70 mm × 18 mm × 2 mm
- Conductive medium inside: Saline with $\sigma = 0.02\ S/m$

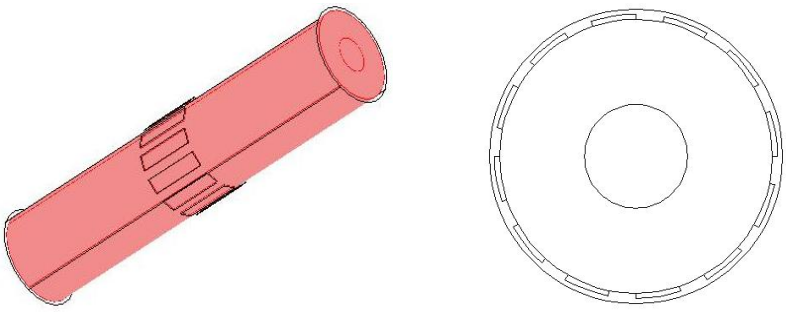

(a) 3D sensor model without guards (b) 2D sensor model with distribution

Figure 3.13 2D and 3D ERT sensor models without end guards

To examine the fringe effect, different electrode lengths are used. Similar to ECT, each time one electrode is applied a voltage signal and all other electrodes are kept at ground

for detection. This process is repeated until all the independent measurements are taken. Because the voltage-excitation and current-measurement method is used for the conductance measurement, the exactly same calibration and normalisation procedure as ECT can be adopted. Also, sensitivity maps for ERT sensors can be generated in a similar way to that for ECT sensors. Since the object to be imaged in Figure 3.13 (b) is non-conductive ($\sigma = 0\ S/m$), the lower reference for conductance measurement is 0. The higher reference is acquired when the simulation model is filled with homogeneous saline of conductivity listed above, and then the normalisation process is taken after the measurement data are obtained. The first 11 values of normalised conductance for 2D and 3D ERT sensor models with different electrode length and without end guards are shown in Figure 3.14.

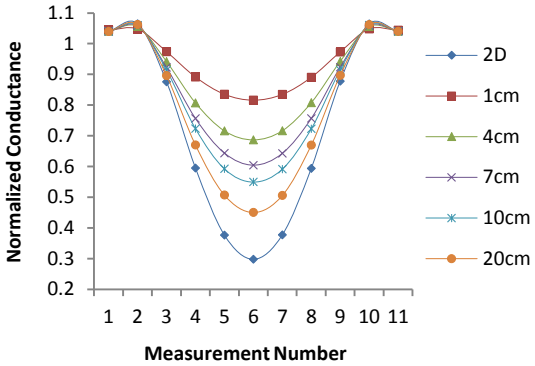

Figure 3.14 Comparison between normalised conductance for 2D and 3D ERT sensor models with different electrode lengths and without end guards

Similarly, the normalised conductance for the 3D ERT models would become closer and closer to that for the 2D model when the electrode length increases. Based on the normalised conductance of a whole measurement frame for each 3D ERT sensor and sensitivity maps of the 2D ERT sensor model generated in the same way as ECT, images are reconstructed for the distribution in Figure 3.13 (b) using LBP, and the results are shown in Figure 3.15. With the reconstruction result for the 2D sensor model as the reference image, the relative image errors of Figure 3.15 (b)~(f) are calculated and shown in Figure 3.16. As expected, the relative image errors for the 3D ERT sensor models decrease with the increase in electrode length, which is similar to the corresponding results for the 3D ECT sensors. This also confirms that the electric fields

of ECT and ERT sensors are similar to each other and similar fringe effect exists in term of the normalised measurement when both are excited in the same way.

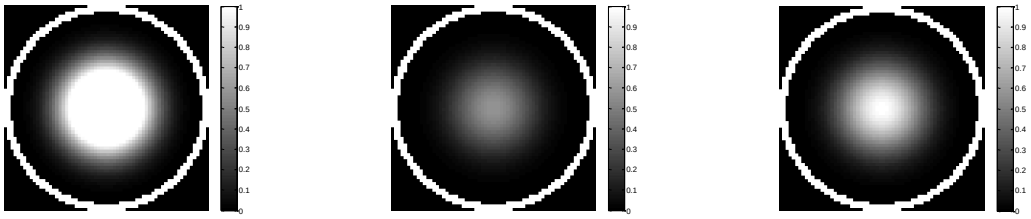

(a) 2D ERT model

(b) 3D ERT model with 1 cm electrodes

(c) 3D ERT model with 4 cm electrodes

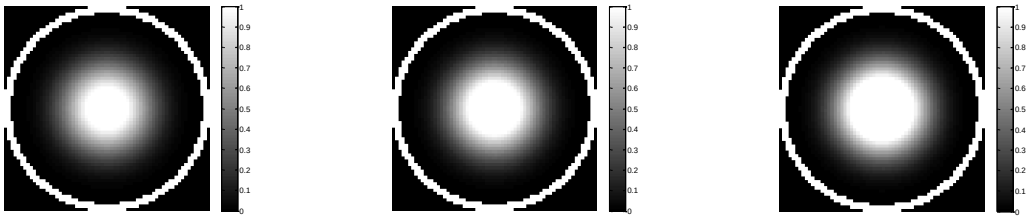

(d) 3D ERT model with 7 cm electrodes

(e) 3D ERT model with 10 cm electrodes

(f) 3D ERT model with 20 cm electrodes

Figure 3.15 Reconstructed images of distribution in Figure 3.13 (b) for 2D and 3D ERT models with different electrode lengths and without end guards

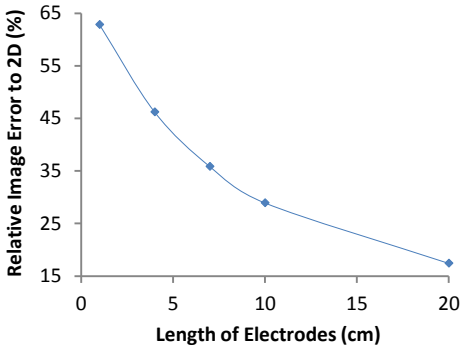

Figure 3.16 Relative image errors of reconstruction results for 3D ERT models with different electrode lengths and without end guards regarding the 2D one

3.3.3 Simulation models and results for ERT sensors with end guards

To compare with the previous results, grounded end guards are applied to the previous 3D ERT sensors, and the 2D and 3D sensor structures are shown in Figure 3.17. Some parameters of the 3D ERT sensor model with grounded end guards are:

- Thickness of end guard: 2 mm
- Length of end guard: 50 mm
- Gap between end guard and electrode: 5 mm

Other parameters are the same as the ERT sensors without guards. Note that unlike ECT sensors, no shield is included in the ERT sensor because no conductive medium exists between shield and pipe wall. Similar simulation and normalisation are carried out and the first 11 values of normalised conductance for the 2D and 3D ERT sensor models with different electrode length and grounded end guards are shown in Figure 3.18. The corresponding images reconstructed using LBP are shown in Figure 3.19, while the relative image errors for the 3D ERT models with different electrode length and grounded end guards are shown in Figure 3.20, referred to the reconstructed image for the 2D model.

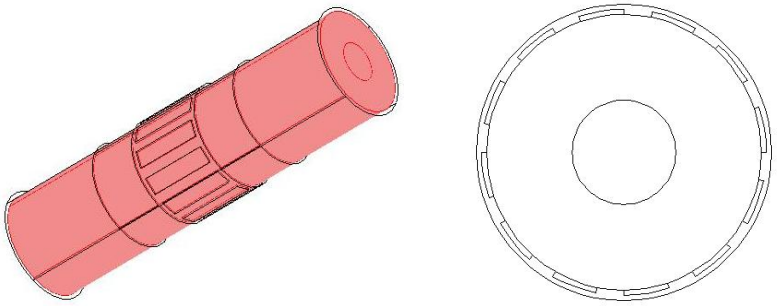

(a) 3D ERT sensor with end guards (b) 2D ERT sensor with distribution

Figure 3.17 2D and 3D ERT sensor models with grounded end guards

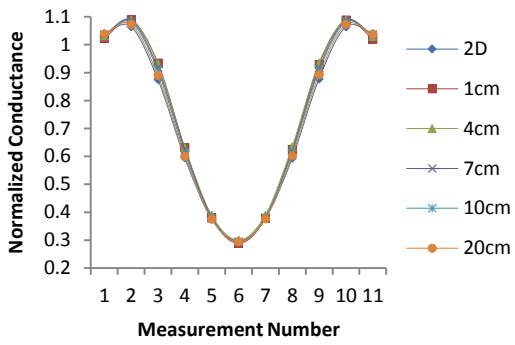

Figure 3.18 Comparison between normalised conductance for 2D and 3D ERT sensor models with end guards and different electrode lengths

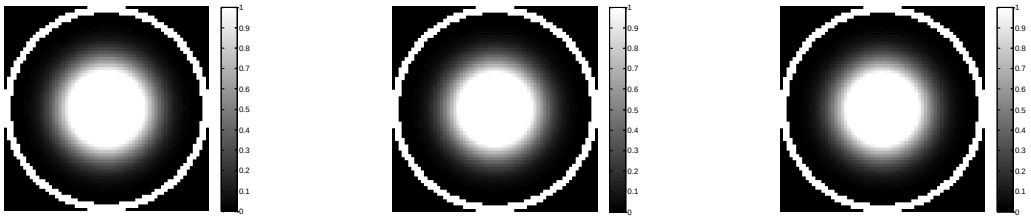

(a) 2D ERT model

(b) 3D ERT model with 1 cm electrodes

(c) 3D ERT model with 4 cm electrodes

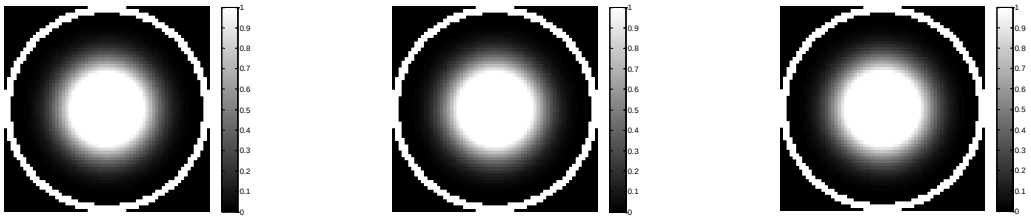

(d) 3D ERT model with 7 cm electrodes

(e) 3D ERT model with 10 cm electrodes

(f) 3D ERT model with 20 cm electrodes

Figure 3.19 Reconstructed images of distribution in Figure 3.18 (b) for 2D and 3D ERT models with different electrode lengths and end guards

Note that the relative image errors for all 3D ERT sensor models with end guards are well below 6% regardless of the electrode length as shown in Figure 3.20, although the relative image error of the 3D ERT sensor model with electrode length of 4 cm is slightly larger than the 3D sensor model with electrode length of 1 cm. This is very different from the results for 3D ECT sensors with end guards in Figure 3.12. The possible reason for this phenomenon is that the object being imaged is non-conductive, i.e. much smaller conductivity than the background. This non-conductive object placed

along the middle axis of the pipe would cause the current to flow around the pipe wall and the grounded end guards, which are mounted on the inner surface of the pipe wall and absorb almost all the current that tends to flow outside the sensor plane. In ECT, however, the permittivity contrast of the object to the background is much lower than the conductivity contrast in ERT and the high permittivity object would draw the electric field to itself. Therefore, a significant part of the electric field lines can still penetrate the high permittivity material and spread along the middle axis of the pipe with only a few of them drawn to the grounded end guards. This is verified by changing the conductivity of the object to be imaged in Figure 3.17 (b) from $\sigma = 0\ S/m$ to be $\sigma = 0.06\ S/m$, with which the conductivity contrast of the object to the background is 3:1 the same as the permittivity contrast in ECT simulation. Note that both the non-zero lower reference and higher reference need to be acquired in this case for normalisation of measured conductance. The first 11 values of normalised conductance in this case are shown in Figure 3.21.

The comparison result shown in Figure 3.21 is similar to that for the ECT sensor in Figure 3.10, confirming the explanation above. The conclusion is that a similar fringe effect exists in ECT and ERT sensors with the same permittivity or conductivity contrast of object to background. Since there is a much larger difference between the normalised conductance for 2D and 3D ERT sensors with electrode length of 20 cm in Figure 3.21 than in Figure 3.18, the normalised conductance for other 3D ERT sensors with electrode length less than 20 cm should have even larger difference than those in Figure 3.18, as indicated by previous simulation results.

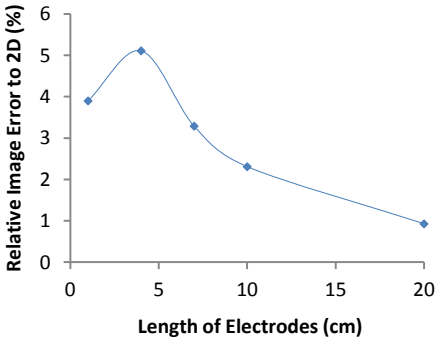

Figure 3.20 Relative image errors of reconstruction results for 3D ERT models with different electrode lengths and end guards regarding the 2D one

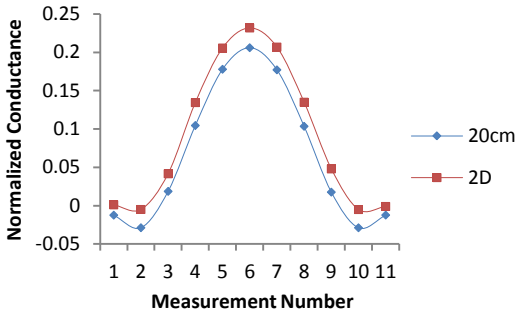

Figure 3.21 Comparison between normalised conductance for 2D and 3D ERT sensor models with electrode length of 20 cm and end guards when object being imaged is conductive

3.4 Test case: Fringe effect of ECT/ERT sensors with non-symmetric object distribution

All the previous results are based on the simulation models with the symmetric object distribution, i.e. the object is situated in the centre of the sensor. To further investigate the fringe effect of ERT sensors, simulation was carried out with a non-symmetric object distribution. The simulation models with or without grounded end guards are the same as in the section 3.3, but only for electrode length of 4 cm, 10 cm and 20 cm in each case. The 2D view of the object distribution is shown in Figure 3.22.

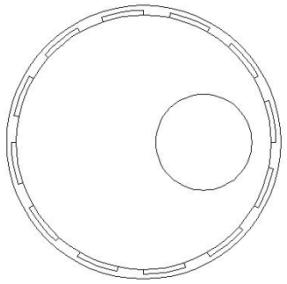

Figure 3.22 2D view of an ERT sensor with non-symmetric object distribution

Similarly, 66 normalised conductance values of a whole frame for the 2D and 3D ERT sensor models with different electrode length and with or without grounded end guards are shown in Figure 3.23 and Figure 3.24.

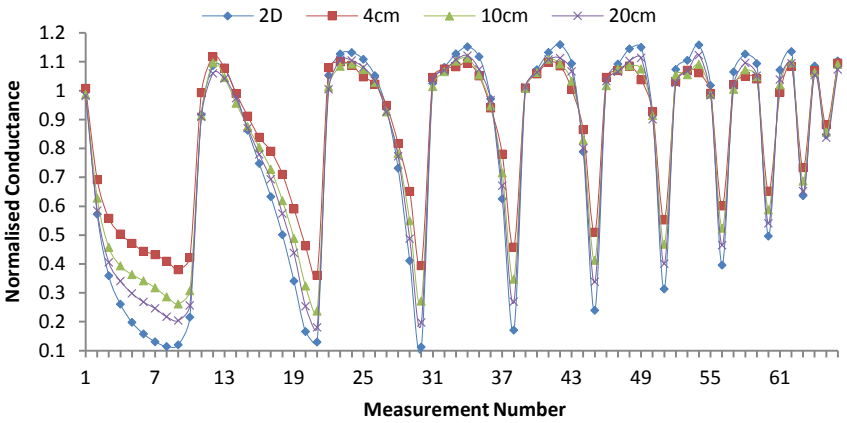

Figure 3.23 Comparison between normalised conductance for 2D and 3D ERT sensor models with non-symmetric object distribution and different electrode lengths and without end guards

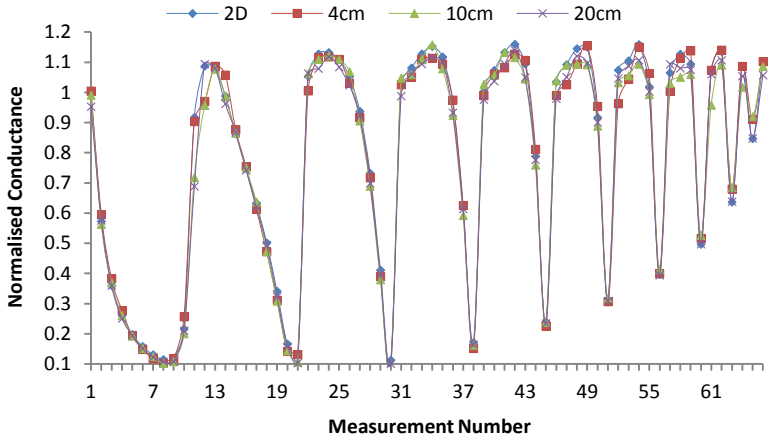

Figure 3.24 Comparison between normalised conductance for 2D and 3D ERT sensor models with end guards, different electrode lengths and non-symmetric object distribution

Similarly, Figures 3.23 and 3.24 show that the normalised conductance with the 3D ERT models would become closer and closer to their 2D reference when the electrode length increases or when the grounded end guards are applied. Based on those normalised conductance, images are reconstructed using LBP. Regarding the reconstructed image for the 2D ERT model as the reference, the relative image errors for the 3D ERT sensor models are given in Table 3.1.

Table 3.1 Relative image error of reconstruction results for 3D ERT models with non-symmetric object distribution regarding the 2D reference

	Relative image error (%)	
Electrode Length (cm)	Without end guards	With end guards
4	25.47	4.63
10	14.87	3.97
20	8.55	1.49

From Table 3.1, it can be seen that there is less fringe effect for the ERT sensors with the electrode length increased or the grounded end guards applied. However, compared with the corresponding results in the last section, the ERT sensors with the non-symmetric object distribution present less fringe effect for the same electrode length without grounded end guards. With this non-conductive object and specific distribution, all the normalised conductance related to the nearest electrodes to the object (the first and last electrodes excited in the simulation process) is greatly reduced except for those corresponding to adjacent electrode pairs (i.e. the detection electrode is adjacent to the excitation electrode) as shown in Figure 3.23. The non-conductive object also blocks part of the current path between each opposite electrode pair as well as some of those related to the electrodes near the object besides the two nearest electrodes. This means that the corresponding conductance between all those electrode pairs is reduced. As a result, more current flows into other electrodes, most of which are adjacent and nearly adjacent to the excitation electrode as indicated by Figure 3.14 and Figure 3.23. Because the current received by adjacent and nearly adjacent electrodes flows around the pipe wall, it can be absorbed easily by the grounded electrodes when it tends to flow outside the electrode plane, compared with the current received by the opposite or nearly opposite electrodes. All the above factors lead to less fringe effect. Therefore, with the end guards, the fringe effect becomes even less, as indicated by the smaller relative image errors of the reconstructed images in this case. Obviously, the end guards can absorb most current tending to flow outside the sensor plane. This test case shows that long electrodes and grounded end guards can reduce the fringe effect of the ERT sensors with the specified non-symmetric object distribution, which complies with the previous conclusions. This also applies to ECT sensors with the non-symmetric object distribution since ERT and ECT sensors behave similarly as indicated by previous simulation results.

It is interesting to investigate whether less fringe effect occurs in the case for the 2D and 3D ECT sensor models shown in Figure 3.1 or Figure 3.8, with the non-symmetric object distribution as shown in Figure 3.22. Figure 3.25 shows a comparison between 28 normalised capacitance values of a whole frame for the sensor models in Figure 3.8 with the distribution in Figure 3.22.

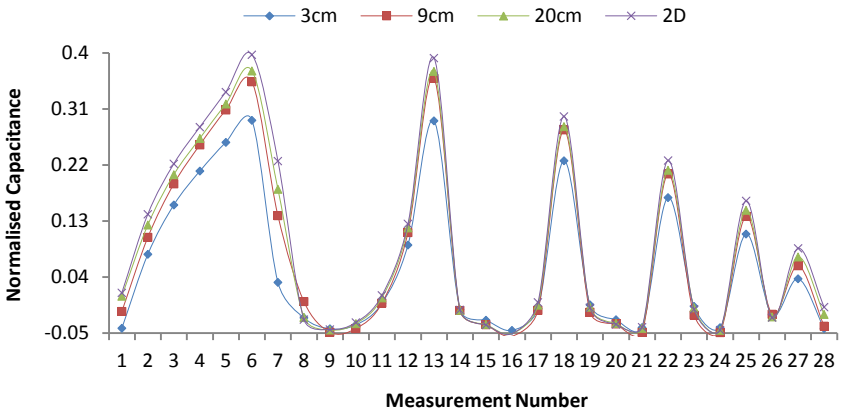

Figure 3.25 Comparison between normalised capacitance for 2D and 3D ECT sensor models with end guards, different electrode lengths and non-symmetric object distribution

Compared with Figure 3.10, Figure 3.25 shows that there is less fringe effect. A possible reason is that the high permittivity material (the object) would draw more electric field lines to itself, resulting in a larger proportion of electric field distributed near the pipe wall compared to the case with an object in the centre. Therefore, more electric field lines tending to spread outside the sensor plane can be drawn to the grounded electrodes or guards. This indicates less fringe effect in this case. This is also confirmed by the smaller relative image errors as shown in Table 3.2 for the reconstruction of the non-symmetric distribution using LBP and with 2D result as reference, compared with the corresponding results for the symmetric distribution in Figure 3.12.

Table 3.2 Relative image error of reconstruction results for 3D ECT models with non-symmetric object distribution and end guards regarding the 2D reference

Electrode length (cm)	Relative image error (%)
3	35.81
9	16.39
20	8.58

3.5 Experimental validation

3.5.1 Experimental setup and system calibration

To validate the above findings, e.g. the feasibility of ERT sensors with voltage-excitation, experiments were carried out using an impedance-analyser-based multi-channel imaging system. The performance and detailed information about this imaging system can be found in Chapter 2 and Hu *et al*. (2008). For this validation study, an available ECT sensor was used for both capacitance and conductance measurement. As shown in Figure 3.26 (a), the ECT sensor has 8 large inner electrodes, i.e. the electrodes are mounted on the inner surface of the tube wall, which directly contact with the substances inside the tube, while its end guards are mounted on the outer surface of the tube wall which are not in contact with the substances inside. Its 2D simulation model is shown in Figure 3.26 (b) with an object placed in the centre. Some parameters of the ECT sensor are listed below:

- Diameter: 7.4 cm
- Electrode size: 65 mm × 25 mm × 1 mm
- Thickness of pipe wall: 3 mm
- Distance between shield and electrodes: 11 mm
- Height of the tube and shield: 17.5 cm
- Length of grounded end guards: 2 cm
- Gap between the end guards and electrodes: 5 mm
- Thickness of tube bottom: 3 cm
- Distance between the tube bottom and bottom end guards: 1 cm

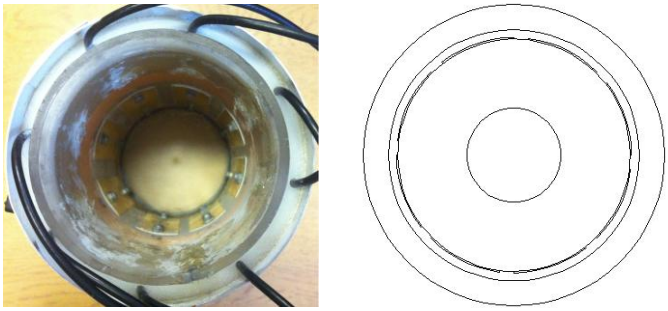

(a) Sensor photo (b) 2D simulation model

Figure 3.26 Photo of and 2D simulation model for the ERT sensor used in experiment

With an impedance analyzer HP4192, an ac voltage of 1.1 V is applied to one electrode of the ECT sensor and other electrodes are grounded for conductance or capacitance measurements one by one. During the experiment, it was found that a kind of resonance occurred in the measurement system when the excitation frequency is above 5 MHz, since the whole system can be equivalent to a RLC network. This resonance would affect the measured capacitance and conductance significantly (HP, 1987). Therefore, the excitation frequency below 5 MHz was chosen to see whether the frequency has significant impact on the fringe effect.

Before measurements were taken, a calibration was conducted for the impedance analyser. There are two steps to take in the calibration: (1) The conventional self-testing was carried out by pressing the BLUE key and then SELF TEST key after the impedance analyser was switched on to confirm the functional operation of the instrument as described in (HP, 1987); (2) ZERO (OPEN) and ZERO (SHORT) calibration for capacitance and resistance measurements was performed by following the procedure described in (HP, 1987), in which the residual impedance and stray admittance inherent to the test fixture used can be measured and their effects be offset to zero.

3.5.2 Experimental verification of ERT with voltage-excitation

After the calibration, the conductance (the real part of the impedance readings) was measured and used to reconstruct the distribution in Figure 3.26 (b) and to verify the feasibility of ERT with voltage-excitation. The excitation frequencies were chosen to be 100 kHz, 1 MHz and 5 MHz. The conductive background medium inside the sensing domain was saline ($\sigma = 1.045\, mS/cm$) with a non-conductive rod as the object. Note

that the large electrodes of the ECT sensor used can reduce the influence of contact impedance between electrodes and electrolyte on the conductance measurement, but the contact impedance is not measured and calibrated. 2D simulation based on the setup as shown in Figure 3.26 was conducted using the In-Plane Electric Currents (Quasi-statics, electric) mode in COMSOL Multiphysics as described in Chapter 2. Because the contact impedance is not considered in the simulation, the normalised conductance at the three frequencies from the 2D simulation is almost the same (below 2% difference). Thus only 2D simulation results at the excitation frequency of 100 kHz are shown in Figure 3.27 together with the experimental results at those three excitation frequencies. Note that the measured and simulated conductance are normalised in the same way as in section 3.3.

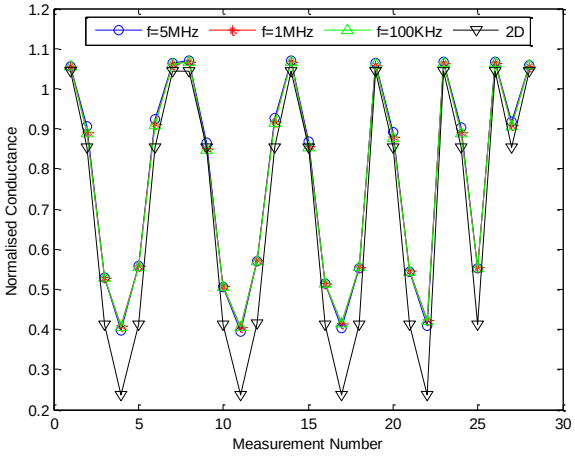

Figure 3.27 Comparison between normalised conductance from 2D simulation and experimental setup at different excitation frequencies

Apparently, the normalised conductance values at the three frequencies are close to each other, but significant difference exists between these three and the 2D reference. The main reason for this difference is the fringe effect. Although their length is 2 cm (a little more than 1/4 of the sensor diameter), the end guards in the ERT sensor used in the experiment are mounted on the outer surface of the tube wall, which has no effect on confining the axial sensing range of the ERT sensor (no contact with electrolyte). Therefore, the current can flow outside the sensor plane and then return to the detection electrodes. This shuttle effect increases the conductance between the detection electrode and the excitation electrode, especially when the detection electrode is opposite to the

excitation electrode. Note that this shuttle effect does not occur in the 2D simulation. In the previous simulation for the ERT sensor with grounded end guards, the guard length is half of the sensor diameter as suggested by Peng *et al*. (2005), and the guards directly contact with the electrolyte, reducing the fringe effect effectively as shown in Figure 3.18.

Another possible reason is the influence of contact impedance, which was claimed to be equivalent to a combination of a resistance and a capacitance (Webster 1998, McAdams *et al*. 1996, Boyle and Adler 2011). The impedance value of the capacitance depends on the excitation frequency while the resistance does not. The impedance values of these two parts would constitute part of the measured resistance or conductance, which would contribute to the difference between the experimental results at different excitation frequencies and their 2D reference. However, the contact impedance may not be a big issue because the normalised conductance for the ERT sensor is almost independent of the excitation frequency as shown in Figure 3.27, which was confirmed by Szczepanik and Rucki (2007) with simulation and experiment for an ERT sensor with insulating wall. By comparing the experiment result and the simulation result with 10 cm long electrodes in Figure 3.14, it was found that the fringe effect of the sensor in the experiment is less than expected from the simulation because the electrode length in the experiment (6.5 cm) is shorter than the tube diameter but the electrode length in the simulation (10 cm) equals to the pipe diameter. One possible reason may be the use of saline with different conductivity in the experiment. Also in the simulation both top and bottom of the sensor are open space and sufficiently far from the measurement electrodes, but in the experiment, the bottom of the sensor is near the measurement electrodes and sealed with plastic to keep the saline. Other reasons for the asymmetric distribution of normalised conductance with measurement number in Figure 3.27 would be the fabrication error of the sensor, the measurement noise and the experiment setup error.

With the normalised conductance from the 2D simulation and experiment setup at different excitation frequencies, the object distribution in Figure 3.26 can be reconstructed using LBP, and shown in Figure 3.28. Note that the sensitivity maps are generated from the above 2D simulation model in the same way as in section 3.2. Figure 3.28 shows that the correct position and shape of the object can be reconstructed at

different excitation frequencies, although image artefacts exist. This can verify the feasibility of the ERT sensor with voltage-excitation and current-measurement.

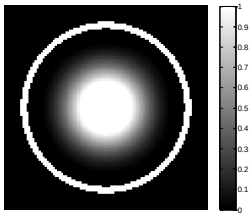

(a) 2D reference

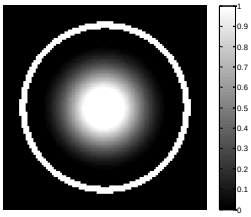

(b) 100 kHz

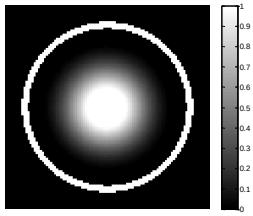

(c) 1 MHz

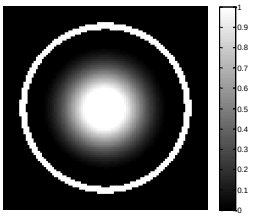

(d) 5 MHz

Figure 3.28 Reconstructed images of distribution in Figure 3.26 (b) with the 2D ERT simulation model and experimental setup at different excitation frequencies

3.5.3 Experimental validation of findings regarding ECT

To validate the findings regarding ECT, experiments were conducted using the same imaging system and sensor as in the previous subsection. In the experiment, air ($\varepsilon_r = 1$) is the background while salt powder ($\varepsilon_r = 3$, which is the estimated value by experiment), as the higher permittivity material, i.e. the object. The imaginary part of each reading from the impedance analyser (i.e. capacitance) is used for image reconstruction of the distribution shown in Figure 3.26 (b). Since the sensitivity of the impedance analyser for capacitance measurement at frequencies below 1 MHz is too low for the specified ECT sensor, higher excitation frequencies, i.e. 1 MHz, 2 MHz and 5 MHz, were chosen in the experiment. But excitation frequencies above 5 MHz were not used. As explained previously, they would induce a kind of resonance in the measurement system and cause significant errors in the capacitance measurements (several times increase in the measured capacitance for all the electrode pairs). 2D simulation at those excitation frequencies was conducted using the In-Plane Electric Currents (Quasi-statics, electric) mode in COMSOL Multiphysics as described in

Chapter 2. Because the 2D simulation at those three excitation frequencies almost gave the same normalised capacitance for the specified distribution (below 2% difference), only the results at 1 MHz are shown in Figure 3.29 together with the experimental results. Note that the measured and simulated capacitance are normalised in the same way as in section 3.2.

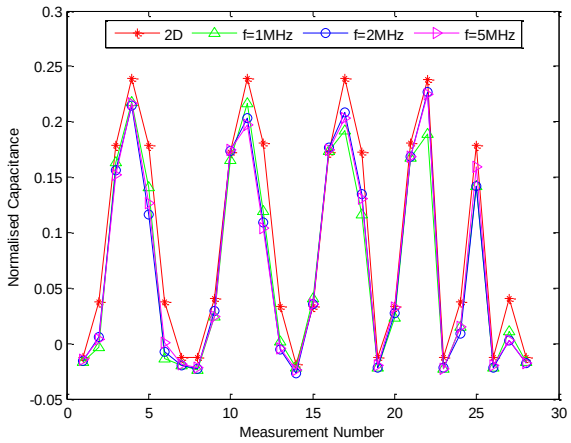

Figure 3.29 Comparison between normalised capacitance from the 2D simulation and experimental setup at different excitation frequencies

Figure 3.29 shows that certain fringe effect exists in the experimental results at different excitation frequencies. There are two crucial differences between the experiment setup and the simulation setup in sub-section 3.2.4: (1) The length of grounded end guards is only a little more than 1/4 of the sensor diameter, not half the sensor diameter as required in simulation; (2) The outer shield is longer than required in simulation (3.5 cm and 7.5 cm for the sections just below and above the electrode plane respectively). In principle, the shield sections above and below the electrode plane can function similarly as the grounded end guards, although a larger gap exists between them and the electrodes. Therefore, the longer shield could compensate the drawbacks caused by the shorter grounded end guards regarding the fringe effect, especially the section above the electrode plane, which is even longer than the sensor diameter, can reduce the fringe effect more effectively. This is why the fringe effect of the sensor used in the experiment seems more or less the same as the sensor with 9 cm electrodes and end guards used in the simulation of section 3.2. Another possible reason for this is that the electrode length in the experiment (6.5 cm) is close to the tube diameter (7.4 cm) and the electrode length in the simulation (9 cm) is almost equally close to the pipe diameter

(10 cm). Similarly, the reasons for the asymmetric distribution of normalised capacitance with measurement number in Figure 3.29 would be the fabrication error of the sensor, the measurement noise and the experiment setup error. Nevertheless, the experimental results at 1 MHz, 2 MHz and 5 MHz can partially verify the findings regarding the fringe effect of ECT sensors in the previous simulation.

To further illustrate the fringe effect of the ECT sensor used in the experiment, images were reconstructed for the distribution in Figure 3.26 (b) using LBP and shown in Figure 3.30. Note that the sensitivity maps are generated from the 2D simulation model in the same way as in section 3.2.

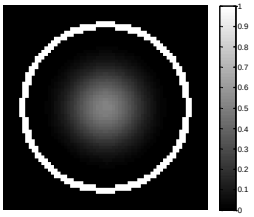

(a) 2D reference

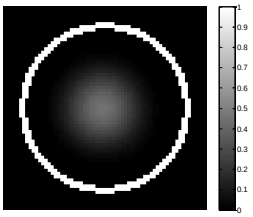

(b) 1 MHz

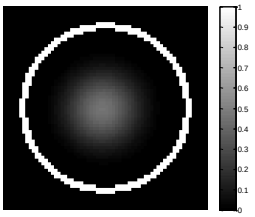

(c) 2 MHz

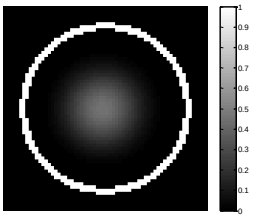

(d) 5 MHz

Figure 3.30 Reconstructed images of distribution in Figure 3.26 (b) with the 2D ECT simulation model and experimental setup at different excitation frequencies

Compared with the 2D reconstruction result, the fringe effect with the specified distribution is shown in Figure 3.30 for the ECT sensor used in the experiment at different excitation frequencies. Once again, this is similar to the corresponding simulation result in section 3.2. The results in this section suggest that a suitable range of the excitation frequency is 1~5 MHz for ECT/ERT dual-modality measurements with the sensor used in the previous experiment.

3.6 Common structure for ECT/ERT sensor

As discussed in sections 3.2 and 3.3, grounded end guards can be applied to both ECT and ERT sensors to reduce their fringe effect, if voltage-excitation is adopted for ERT. With voltage-excitation for ERT, only additional calibration and measurements need to be taken to reduce the influence of the contact impedance on the conductance measurement. From this point of view, ECT and ERT sensors can share a common structure similar to that shown in Figure 3.8 to narrow their sensing ranges in the axial direction. This is not only beneficial for reduction of the fringe effect, but also for dual-modality measurement needed in some industrial applications. Li and Yang (2009) discussed the necessity and development of multi-modality tomography systems, and did some initial simulation and experiment to investigate the feasibility of an ECT/ERT dual-modality system with voltage-excitation, and some promising results were obtained. This also confirms that an ERT system with voltage-excitation is feasible. However, they used two separate sensors for ECT and ERT measurements. Marashdeh *et al*. (2007) proposed a multi-modal system based on ECT sensors, which used capacitance measurements for permittivity imaging and power balance measurements for conductivity imaging. Although it is non-invasive and seems promising, there is no evidence that this kind of system can be applied in the situations with conductive background medium since the background medium was always set to be non-conductive in their experiment. Also, the proposed reconstruction technique is only valid when the capacitance signal is independent from the power signal, which is difficult to achieve in most industrial applications.

To avoid these drawbacks and reduce the fringe effect, the approach described in section 3.3 and verified in the section 3.5, with which only one sensor is needed, is suggested for both ECT and ERT measurements while related electronics can be designed in the same way as proposed by Li and Yang (2009). With this structure, the sensor design for ECT and ERT dual-modality measurements would be as simple as suggested by Marashdeh *et al*. (2007), and the interference between two separate sensors or two measurement signals can be eliminated. More temporally closely correlated ECT and ERT measurements can also be acquired at the same time, which is beneficial for dynamic measurements required in some industry processes.

3.7 Summary

Similar fringe effect exists in both ECT and ERT sensors if both of them adopt voltage-excitation. The 3D distribution of electric field would miscalculate the sizes and displace the positions of objects being imaged in a reconstructed 2D image. By comparing the simulation results of the 3D ECT and ERT sensor models after normalisation with the corresponding 2D one, it is concluded that long electrodes can improve the uniformity of axial electric field distribution and reduce the fringe effect in ECT and ERT sensors. The negative effect is that it would enlarge the axial sensing range. To solve this problem, grounded end guards are commonly used in ECT sensors to narrow the axial sensing range for a specified electrode length. Simulation suggested that grounded end guards can reduce the fringe effect contained in capacitance after normalisation, but it cannot be used in ERT sensors with current-injection. To apply grounded end guards in ERT sensors, the voltage-excitation and current-measurement strategy is introduced into ERT measurements, and validated by experiments. Simulation results indicate that grounded end guards can reduce the fringe effect in ERT sensors with voltage-excitation.

Images are reconstructed for both symmetric and non-symmetric object distributions in ECT and ERT sensors without or with end guards using LBP. It is shown that the reconstructed images for the 3D sensor models approach to the corresponding 2D reference when the electrode length increases or with grounded end guards applied in both cases. Finally, a common structure is proposed for ECT and ERT sensors to reduce their fringe effect, which has potential applications for improved dual-modality measurements required in some industrial processes.

Chapter 4: Fringe effect of ERT sensors due to axially non-uniform object distribution

This chapter will investigate the fringe effect of ERT sensors due to axial object distribution. An ERT sensor is excited with the conventional current-injection strategy in both simulation and experiment. The fringe effect is evaluated for typical distributions with objects of different lengths and conductivities and at different cross-sectional and axial positions. An experimental ERT system is established based on a commercial data acquisition unit to verify the findings from simulation. A simple compensation method for the fringe effect and an associated three-plane sensor scheme are proposed, which has been validated by simulation and experiment.

4.1 Introduction

The applications of ERT (often referred to as electrical impedance tomography (EIT)) have been extended from medical imaging to industrial monitoring and measurement, e.g. multi-phase flows with conductive medium inside cylindrical pipes or vessels. While the current-injection and voltage-measurement strategy is usually adopted for ERT, different protocols can be applied for data acquisition, e.g. adjacent, opposite and diagonal with non-conductive boundary for 2D ERT imaging (Dickin and Wang, 1996). Among those protocols, the adjacent strategy is the most popular and will be used for data acquisition in this chapter.

As discussed in Chapter 1, the fringe effect would occur with 2D ET imaging because certain conditions should be satisfied to make it permissible that the 3D reconstruction can be simplified to 2D with tolerable errors. The first condition is that the electric field should be approximately confined within an ERT sensor and axially uniform. The second one is that the object distribution is axially uniform. This can guarantee a 3D electric field to be represented by the corresponding 2D one with negligible errors. With axially non-uniform object distribution, however, the electric field distribution would become axially non-uniform even if the first condition above is satisfied, i.e. severe fringe effect may occur, since the electric field distribution depends on the object distribution due to the soft-field nature of ERT besides the sensor structure.

Up to now the fringe effect of ERT sensors for 2D imaging has not been investigated systematically, as described in Chapter 1. The image-forming mechanism of an EIT system was described by using equi-current perturbation hypothesis and axially extending an object from the sensor plane to a distant position, aiming at investigating the fringe effect with different electrode pairs (Rabbani and Kabir 1991). It was concluded that where the disturbed equi-current surface with the largest current density intersects the cross-section of the EIT sensor is where the largest change in the reconstructed image would take place. The images reconstructed for the extended objects covering the whole cross section would be circular, but for the extended objects not covering the whole cross section, the situation would be different because the corresponding analysis based on the equi-current perturbation hypothesis would be not as ideal as in the former case. Wang (1999) also conducted research into the fringe effect in EIT with experimental, simulation and analytical models. One of the findings was that the axial 3D attenuation range (3/4 attenuation) regarding the EIT sensor plane would be one third of the vessel's diameter. Another phenomenon discovered was that the image reconstructed for a small object in the halfway between the centre and the pipe wall and moving away from the sensor plane would move towards the centre of the cross section of the sensor. But these two findings did not account for the influences of the object length on the fringe effect since only a small non-conductive ball was taken as the test object in the experiment. In Chapter 3, it was found that a similar fringe effect exists in ECT and ERT sensors if both of them are excited by a voltage signal, and increasing the electrode length and grounded end guards would reduce the fringe effect in both cases. But the fringe effect of the conventional ERT sensors with the current-injection strategy was not investigated, e.g. the normalised potential differences or resistance with different measurement strategy. Therefore, it is worthwhile evaluating the fringe effect of single-plane ERT sensors with the current-injection strategy, especially with the normalised measurements as discussed in Chapter 1.

ERT can be applied to various industrial processes, e.g. multi-phase flow imaging and measurement, which normally involves a conductive fluid as the continuous phase and non-conductive material as the dispersed phase, e.g. in a bubble column (Fransolet *et al*. 2001, Fransolet *et al*. 2005, Toye *et al*. 2005, Jin *et al*. 2007, Vijayan *et al*. 2007). The dispersed phase is usually measured and imaged, with the distribution being axially non-uniform. In this case there may exist severe fringe effect. This brings the necessity

to study the fringe effect with axially non-uniform distribution. Because of many possible distributions, a specified ERT sensor with a typical distribution, i.e. core distribution, is investigated, aiming to compensate the fringe effect in 2D imaging. This involves checking whether the above two conditions are satisfied with different measurement strategies, evaluating how large the fringe effect is with objects of different lengths and conductivities and what the influence is when the objects are placed at different axial and cross-sectional positions. Based on the phenomenon discovered, a method is proposed to compensate for the fringe effect of the ERT sensor in different situations. Experimental verification of the findings and the proposed methodology is then presented. A three-plane sensor scheme is proposed to measure the fringe effect induced by objects outside the sensor plane with two auxiliary electrode planes. Simulation and experiment shows that this scheme is effective in reducing the fringe effect and the over-estimation of object size by Landweber iteration.

4.2 Difference between ECT and ERT sensor models

4.2.1 Simulation model for an ERT sensor

In Chapter 3, it was concluded that an ECT sensor with long electrodes would have less fringe effect with axially uniform distributions, because of smaller differences between the normalised capacitance from 3D and 2D simulations. Whether this is true for ERT sensors with current-injection will be discussed in this section. A simulation model for an experimental ERT sensor is established and shown in Figure 4.1 with its geometry parameters and material properties listed.

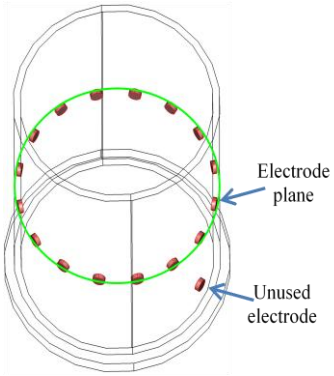

Figure 4.1 Simulation model of an ERT sensor

- Diameter of electrode: 9 mm
- Inner diameter:14.1 cm
- Gap between bottom and electrode plane: 10 cm
- Number of electrodes per electrode plane: 16
- Material of tube: Perspex
- Material of electrodes: Steel
- Gap between the unused electrode and sensor plane: 6 cm
- Height of the tube: 21 cm
- Depth of saline: 19.8 cm

Actually, the ERT sensor has five electrode planes, but only the middle one was used in the simulation as a single-plane ERT sensor as shown in Figure 4.1 (identified by the green circle, i.e. the middle cross-section of the electrode ring). The unused electrodes below the sensor plane in Figure 4.1 is grounded in the simulation to assemble the real situation in practical ERT measurements for the reduction of common mode signals. Note that saline with conductivity of 0.02 S/m was used as the background medium inside the ERT sensor in all the following 3D and 2D simulation. The 2D model of the single-plane ERT sensor with object distribution is shown in Figure 4.2:

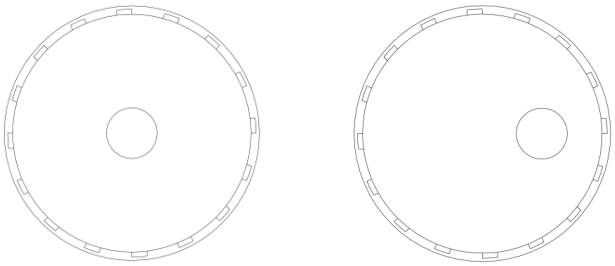

(a) Central core (b) Off-Central core

Figure 4.2 2D model of the single-plane ERT sensor with object distribution

The cross-sectional object distribution for the evaluation of fringe effect is shown in Figure 4.2, with a cylindrical rod of 3 cm in diameter in the centre or off-central midway. It is used as the reference distribution in the following 3D simulation while the rods are variable in axial length and position for different purposes. The 2D ERT sensor in Figure 4.2 (a) or (b) will also be used in all the following 2D simulation to obtain sensitivity maps and corresponding 2D results. Note that all the simulation was carried out in COMSOL Multiphysics with the "In-Plane Electric Currents" mode in the 2D case and "Electric Currents" mode in the 3D case, both of which are in AC/DC module with 10 kHz as the excitation frequency. In the 3D simulation, tetrahedral elements and direct solver (SPOOLES) were used. To ensure the numerical accuracy (i.e. the difference in normalised resistance between a coarse mesh and a finer one is below 2%), the mesh density is increased until the simulated resistance after normalisation converges. The number of elements used in the 3D simulation is of the order of 90,000. Taking the ERT sensor shown in Figure 4.1 as an example to show the influence of mesh size on simulation, the first coarse mesh (the used one) consists of 88,314 tetrahedral elements, and a finer one consists of 180,527 elements, which are shown in Figure 4.3 (a) and (b), respectively.

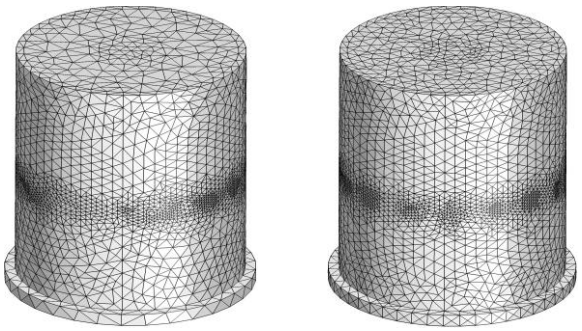

(a) Coarse mesh (b) Fine mesh

Figure 4.3 Meshes

The simulated potential differences before normalisation (i.e. the tube is filled with uniform background medium) and after normalisation (with an axially uniform object distribution as shown in Figure 4.2 (a)) with these two meshes are shown in Figure 4.4, which shows the first 13 values of a whole measurement frame in each case. They have the maximum difference of 1.4% with these two meshes in both cases. This verifies the numerical accuracy of the 3D simulation with the specified mesh. Note that the contact impedance is not included in all the ERT sensors for two reasons: (1) to isolate the fring effect from other error sources, and (2) because the contact impedance in an industrial application can be ignored with the current-injection strategy and a measurement circuit of high input impedance (Szczepanik and Rucki 2007).

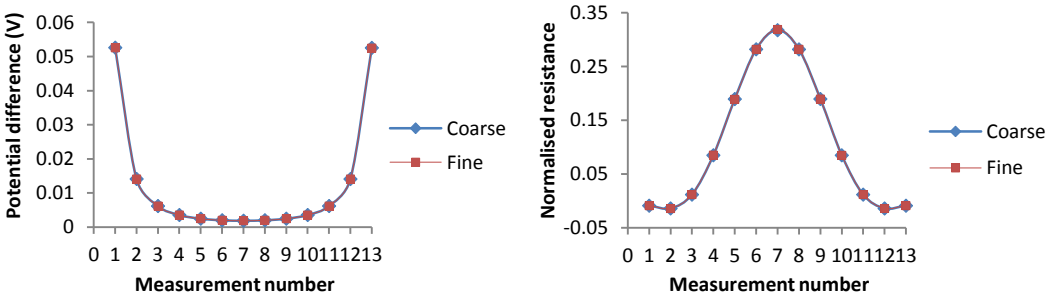

(a) Before normalisaion (b) After normalisation

Figure 4.4 Comparison between the simulated potential difference before and after normalisation with different meshes

4.2.2 Difference between ECT and ERT measurement models

A 2D and two 3D ERT sensors are considered in this subsection. The 2D and the first 3D model are the same as shown in Figure 4.2 and Figure 4.1, respectively. The second 3D

model was built by changing the small round electrodes of the first 3D model to be rectangle electrodes of 10 cm in length and the same width and axial position with other geometry parameters unchanged. To investigate the fringe effect with axially uniform distribution, the ERT sensors, no matter 2D or 3D, were first filled with the background medium, i.e. saline with conductivity of 0.02 S/m. Currents were injected into the three sensors with the same density of 0.55 mA/cm. The first 13 simulated potential differences for the two 3D models using the adjacent current-injection and voltage-measurement strategy are shown in Figure 4.5 (a) with the 2D result as the reference.

Figure 4.5 (a) shows that there is a very large difference between the simulated potential differences from the 2D and 3D ERT sensors with 9 mm long electrodes. This difference may be referred to as "absolute" fringe effect, which would be eliminated with infinitely long electrodes as in an ECT sensor. However, it is the normalised resistance that accounts in the ERT. An axially uniform distribution as shown in Figure 4.2 (a) was set up with a non-conductive rod of the same length as the tube depth (19.8 cm) intruding into the background medium along the middle axis of the tube with both the 2D and 3D sensors. The resultant normalised resistance is shown in Figure 4.5 (b). Note that all the objects inside the sensor in all the following 3D simulation and experiments were positioned axially symmetric to the sensor plane unless specified.

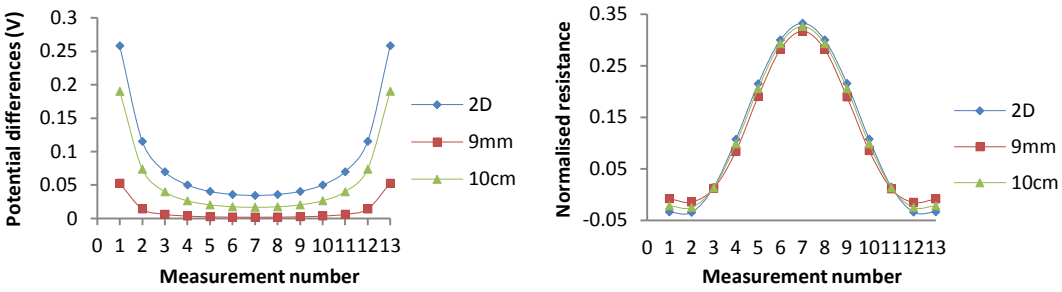

(a) Before normalisation (b) After normalisation

Figure 4.5 Comparison between simulated potential difference before and after normalisation for the 2D and 3D ERT sensors with two different electrode lengths

Unlike the potential difference in Figure 4.5 (a), Figure 4.5 (b) shows very small difference between simulated normalised resistance for the 2D ERT sensor and the 3D ERT sensors. It seems that the normalisation process for the ERT could reduce the fringe effect greatly. However, this does not agree with the corresponding conclusion with the

ECT sensors in Chapter 3. A possible reason is that the ECT adopts the voltage-excitation strategy while the ERT normally adopts the current-injection strategy and their boundary conditions are totally different as described in Chapter 2. The former can be referred to as "Low Z measurement" while the latter as "High Z measurement". The equivalent circuits in these two cases have been discussed by Neumayer *et al*. (2011). For the former there is a single coupling capacitance between the excitation and detection electrodes and for the latter there is actually a voltage divider involving all the impedances between possible electrode pairs. With the adjacent current-injection and voltage-measurement strategy, the detailed equivalent circuit for the ERT measurement is similar to that as described by Szczepanik and Rucki (2007) and is shown in Figure 4.6, which is for the 2D case only. In Figure 4.6 (b), Z_H, Z_L, Z_{V_1} and Z_{V_2} are the contact or electrochemical impedances at the injecting electrodes H and L and the measuring electrodes V_1 and V_2, respectively. The former two have no influence on the potential difference measurement while the latter two are negligible for a measurement circuit with a high input impedance. R_{H_1} to R_{H_n} and R_{L_1} to R_{L_n} represent the resistance between the equi-potential line V_1 and the injecting electrode H and between the equi-potential line V_2 and the injecting electrode L, respectively, which also do not affect the potential difference measurement. R_1 to R_n are the resistances to be measured.

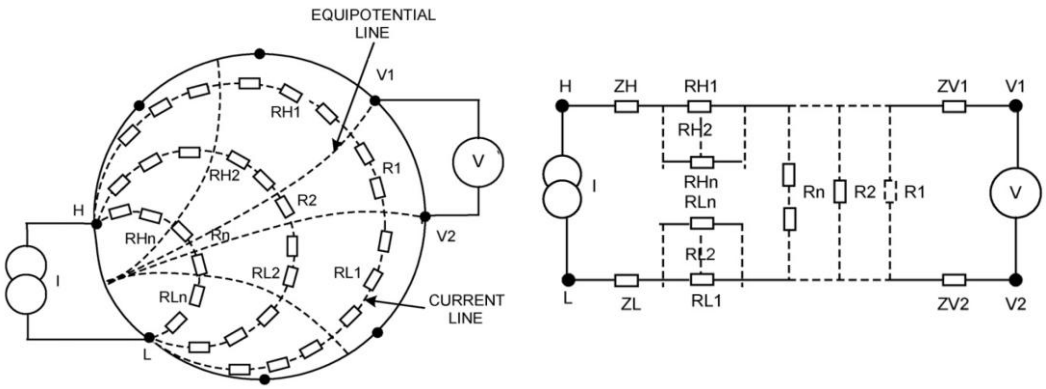

(a) Semi-distributed parameter model (b) Lumped parameter model

Figure 4.6 Electrical model of the ERT sensor proposed by Szczepanik and Rucki (2007)

In the 3D case with fringe effect, the equivalent circuit of an ERT sensor would be more complicated with each defined axial layer similar to the 2D case. If only a single resistance is used to denote the parallel summation of R_1 to R_n as shown in Figure 4.6

(b) in each defined axial layer, then the 3D equivalent circuit of the ERT would be as shown in Figure 4.7 (b). Similarly, the 3D equivalent circuit of the ECT is shown in Figure 4.7 (a).

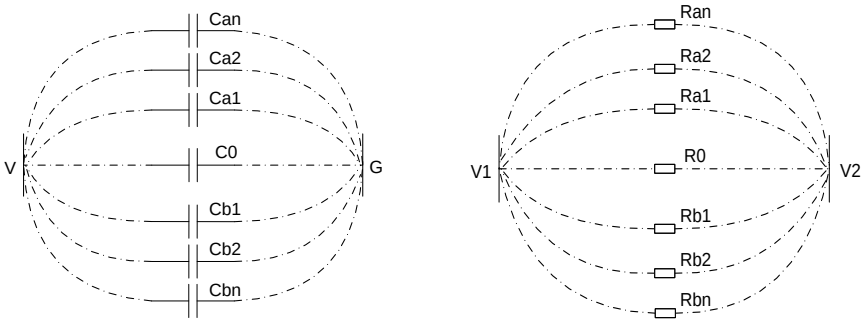

(a) ECT (b) ERT

Figure 4.7 3D electrical models for ECT and ERT measurements

In Figure 4.7 (a), C_0 stands for the elementary capacitance between the excitation electrode V and the detection electrode G, i.e. without the fringe effect. C_{a_1} to C_{a_n} and C_{b_1} to C_{b_n} denote the capacitance induced by the fringe effect above and below the ECT sensor plane, respectively. Similarly in Figure 4.7 (b), R_0 stands for the elementary resistance between detection electrodes V_1 and V_2 without the fringe effect. R_{a_1} to R_{a_n} and R_{b_1} to R_{b_n} represent the resistance induced by the fringe effect above and below the ERT sensor plane, respectively. Figure 4.7 shows that the 3D equivalent circuit of the ECT or ERT is a series of capacitors or resistors in parallel along the axial direction, respectively. For the ECT, the equivalent capacitance of the circuit in Figure 4.7 (a) can be expressed as:

$$C_{equ} = C_{a_1} + C_{a_2} + \cdots + C_{a_n} + C_0 + C_{b_1} + C_{b_2} + \cdots + C_{b_n} \tag{4.1}$$

For ERT, the equivalent resistance in Figure 4.7 (b) can be expressed as:

$$R_{equ} = R_{a_1} // R_{a_2} // \cdots // R_{a_n} // R_0 // R_{b_1} // R_{b_2} // \cdots // R_{b_n} \tag{4.2}$$

With an axially uniform distribution, the largest coupling capacitance in Figure 4.7 (a) is the one inside the ECT sensor plane (C_0), while the smallest resistance in Figure 4.7 (b) is the one inside the ERT sensor plane (R_0). The other coupling capacitance or resistance would attenuate with their distance from the electrode plane for axially

uniform distribution. The smaller the resistance when the tube is filled with a uniform background medium, the more impact its change would have on the related measurement after introducing an object. For an ECT sensor with enough long electrodes, say the same as or larger than the sensor diameter, the largest capacitance in Figure 4.7 (a) would be much larger than other capacitance, which would dominate the equivalent capacitance C_{equ} in equation (4.1), i.e. most electric field lines would be confined inside or within certain small axial range above and below the ECT sensor plane. This means the fringe effect is negligible since the electric field distribution is approaching to the 2D case. But this is not the case with much shorter electrodes than the sensor diameter. This is why the fringe effect of ECT sensors would become less and less with the increase in the electrode length. For an ERT sensor with the adjacent current-injection, however, the situation would be very different. As shown in Figure 4.6 (b), the measured resistance in the 2D case is a parallel summation of resistance between the two equi-potential lines defined by the two measurement electrodes. Since those two equi-potential lines both origin from somewhere between the two current-injection electrodes as shown in Figure 4.6 (a), the resistance between them and near the current-injection electrodes, like R_n, is much smaller than others even with very short electrodes (e.g. 9 mm as in Figure 4.1), which would dominate the equivalent resistance R_{equ} in equation (4.2), i.e. most current would flow inside or within certain small axial range above and below the ERT sensor plane. This means negligible fringe effect occurs in this case since the current distribution is approaching to the 2D case. With longer electrodes, only a little improvement can be achieved due to the very small distance between the current-injection electrodes, indicating that the electrical field of an ERT sensor with the adjacent strategy is more focused than that of an ECT sensor in terms of normalised measurements. This is why the conventional ERT sensor as shown in Figure 4.1 has a negligible fringe effect with the adjacent strategy in terms of the normalised resistance.

A direct proof for the above explanation is that different levels of fringe effect exist for an ECT sensor with certain length but different distribution. Normally, the adjacent electrode pairs with axially uniform distribution near the pipe wall have less fringe effect than the opposite ones with axially uniform distribution along the middle axis of the sensor, as discussed in Chapter 3, because the largest elementary capacitance normally exists between adjacent electrode pairs, while the smallest one between the

opposite ones. To further verify this, the opposite strategy was used for current-injection and voltage-measurement with the above two ERT sensors (9 mm and 10 cm), where the resistance between the two defined equi-potential lines is not as small as with the adjacent strategy. The normalised resistance with the opposite strategy for the above 2D and 3D ERT sensors with the same axially uniform distribution is shown in Figure 4.8. Note that only 6 out of the 7 normalised resistance values are shown in Figure 4.8 because the eliminated potential difference measurement is nearly zero with the opposite strategy, which induces very large errors after normalisation. Unlike in Figure 4.5 (b), Figure 4.8 shows that the normalised resistance for the 3D ERT sensor with electrodes of 10 cm is much closer to the 2D one, i.e. much less fringe effect. This can validate the above explanation.

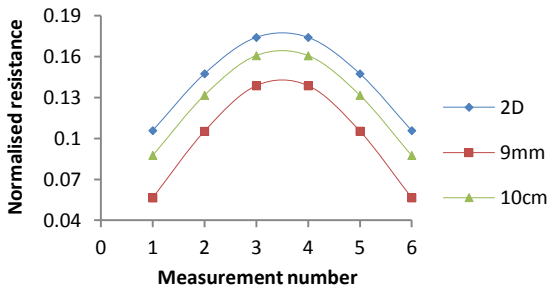

Figure 4.8 Normalised resistance for 2D and 3D ERT sensors with different electrode lengths and axially uniform distribution using opposite measurement strategy

The above discussion shows that there is negligible fringe effect for a conventional ERT sensor with very short electrodes and the specified axially uniform distribution using the adjacent strategy. However, the situation would be different with axially non-uniform distribution. A simple non-uniform distribution would be a non-conductive cylindrical rod shorter than the tube in length intruding into the background medium along the tube axis. In this case, some resistance inside the layers without the rod similar to those in Figure 4.7 (b) would be reduced, compared to the previous case with axially uniform distribution. This would result in the reduction of the equivalent resistance in equation (4.2), causing the normalised resistance to decrease due to the unchanged reference, i.e. more severe fringe effect in this case. To evaluate the fringe effect with non-conductive rods of different lengths and at different axial positions, 3D simulation was carried out and the corresponding results are presented and discussed in the following sections.

4.3 Fringe effect of ERT sensor with axially non-uniform distributions

4.3.1 Centred non-conductive or conductive perturbation inside sensor plane

In the first set of simulation, the distribution investigated was established with centred non-conductive or conductive objects, the same as in Figure 4.2 (a). They were positioned inside and axially symmetrically against the electrode plane with the 3D model in Figure 4.1, i.e. core distribution. Because the tube in Figure 4.1 has a limited length of 19.8 cm, the length of the centred rod was set to be 1, 4, 7, 10 and 19.8 cm, respectively, in the simulation to evaluate the fringe effect. The normalised resistance in these situations is shown in Figure 4.9 (a), (b) and (c) with the corresponding 2D result as the reference. Note that for comparison, the conductivity of the conductive rods was set to be 0.06 S/m and 2 S/m, which are identified by the captions "Conductive" and "Highly conductive" respectively in Figure 4.9.

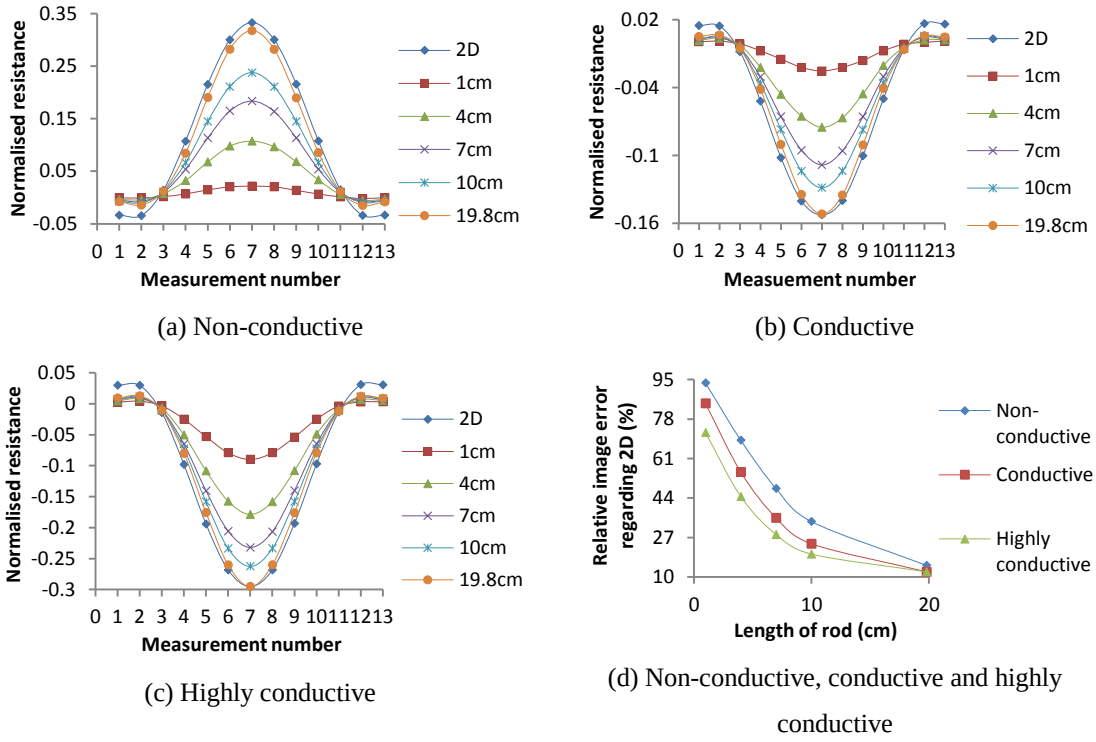

(a) Non-conductive

(b) Conductive

(c) Highly conductive

(d) Non-conductive, conductive and highly conductive

Figure 4.9 Normalised resistance (a-c) and relative image errors of reconstructions regarding 2D one (d) for non-conductive, conductive and highly conductive rods inside the sensor and with different lengths

Figure 4.9 (a) (b) and (c) show that the longer the centred rod, the more similar the normalised resistance to the 2D reference, i.e. longer object gives less fringe effect. To quantify the fringe effect with the above core distribution, images were reconstructed based on their normalised resistance using LBP and the sensitivity maps from the 2D model as shown in Figure 4.2. To evaluate the image error induced by the fringe effect, the image with the corresponding 2D model is used as reference and the relative image errors of reconstructions for the 3D models are calculated and shown in Figure 4.9 (d). It shows that the relative image errors for the central core distribution decrease with the object length in each case. This means that the fringe effect is reduced when longer object emerges inside and along the middle axis of the ERT sensor. This can be explained by the fact that the object distribution would become more and more uniform along the axial direction with the increase in the object length, eventually enabling the permissibility of the 3D electric field being represented by the corresponding 2D one with tolerable errors.

Figure 4.9 (d) shows that less fringe effect occurs with the highly conductive object, especially when the object length is very short, because the highly conductive object part within the sensor plane would reduce the elementary resistance R_0 in Figure 4.7 (b) and attract more current to itself, compared with non-conductive or less conductive object, which would result in the reduction of fringe effect. To illustrate how the fringe effect affects the reconstructed image, the reconstruction results corresponding to the results in Figure 4.9 (a) (for centred non-conductive objects) are shown in Figure 4.10. In Figure 4.10, the reconstructed images are very dim when the rod is very short, e.g. 1 cm and 4 cm long, and become more and more similar to the 2D result when the rod length increases. The reconstruction results for centred conductive objects are similar to those in Figure 4.10.

Since the variation of the fringe effect with the length of the conductive object along the middle axis of the sensor is similar to that of the non-conductive object, the following sections will only discuss the fringe effect for the latter, which is also the most common in the ERT. It is found that longer electrodes in an ECT sensor would induce a less fringe effect for axially uniform distribution. For axially non-uniform distribution, especially with a small object simulated above, long electrodes would average the effect of the object as indicated by the definition of capacitance. This makes the sensitivity decrease

or fringe effect increase. Similarly, an ERT sensor with long electrodes (like 10 cm) would further average the response of axially non-uniform object, i.e. the response would be smaller than the above result for each object length. This would result in more severe fringe effect, and hence short electrodes are preferred for small objects. Therefore, this chapter will mainly discuss the fringe effect of an ERT sensor with small size or "pin" electrodes, i.e. the conventional ERT sensor as shown in Figure 4.1.

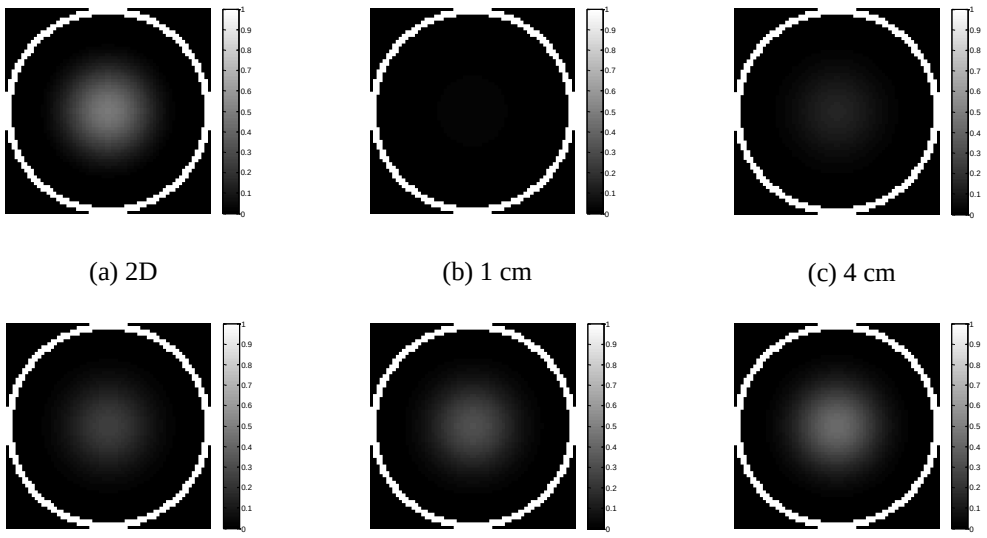

(a) 2D (b) 1 cm (c) 4 cm

(d) 7 cm (e) 10 cm (f) 19.8 cm

Figure 4.10 Reconstruction results for central core distribution inside the sensor and with different lengths

4.3.2 Centred non-conductive perturbation outside sensor plane

This subsection will investigate the fringe effect with centred non-conductive objects outside the sensor plane, which should not be sensed and reconstructed by an ERT sensor. However, the object would appear in the reconstructed images as artefacts due to the fringe effect. In the second set of simulation, centred non-conductive objects were positioned above the top end of electrodes by 0 cm, 1 cm and 3 cm along the middle axis of the sensor. Their lengths were set according to the length of the tube part above the sensor plane. The normalised resistance for the object distribution is shown in Figure 4.11 (a), (b) and (c).

Figure 4.11 (a), (b) and (c) show that long object outside the electrode plane can still have significant influence on the normalised resistance if the object is very close to the

sensor plane. This is due to the existence of severe fringe effect in this case. This kind of influence is undesirable and should be eliminated to obtain high axial resolution and measurement accuracy. To quantify how significant this kind of influence is for objects with the specified lengths, images are reconstructed based on the normalised resistance in Figure 4.11 and using LBP and the sensitivity maps from the 2D model. The norm ratios of the reconstructed images for those 3D models to that for the 2D model are calculated as in equation (4.3) and shown in Figure 4.11 (d). Note that this kind of norm ratio is not the relative image error since images for these objects are taken as undesirable artefacts.

$$NR = \frac{\|\hat{g}\|}{\|g\|} \tag{4.3}$$

where NR is the norm ratio of two images, $\hat{g}$ is the reconstructed image for a 3D model, and g is the reconstructed image for the 2D model.

Figure 4.11 (d) shows that the norm ratios increase with the increase in the object length when the object is placed above the sensor plane by certain distance. The norm ratio can reach 33.64% for the object of 10 cm in length above the sensor plane by 0 cm, which is a significant error. However, it would attenuate with the axial distance of the object head from the sensor plane for each specified length as shown in Figure 4.9 (d). It is less than 12% with 7 cm long object above the sensor plane by 3 cm. Further simulation shows that it is less than 5% when a similar object with a length of 5 cm (the longest) is placed above the sensor plane by 5 cm. A similar conclusion was drawn by Wang (1999) that the 3D attenuation range (3/4 attenuation) in the axial direction regarding the electrode plane is one third of the vessel's diameter (around 4.7 cm) with a non-conductive ball of small dimensions in the half-way between the pipe wall and the centre. In principle, the attenuation of the fring effect is due to the attenuation of the electric field strength or the equivalent resistance along the axial direction of the sensor, as concluded from the previous 3D electrical model for ERT.

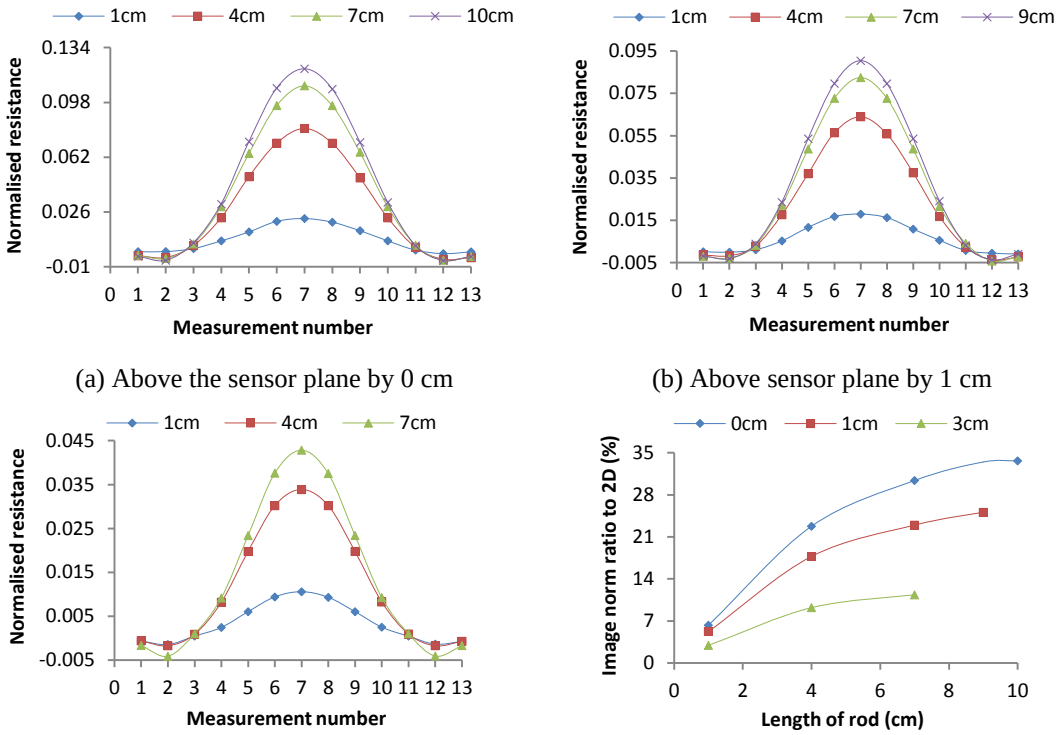

(a) Above the sensor plane by 0 cm

(b) Above sensor plane by 1 cm

(c) Above sensor plane by 3 cm

(d) Above sensor plane by 0 cm, 1 cm and 3 cm

Figure 4.11 Normalised resistance (a-c) and norm ratios of reconstructed images to 2D reference (d) for centred non-conductive object above the sensor plane by 0 cm, 1 cm and 3 cm and with different lengths

The above simulation results for a centred non-conductive object outside the sensor plane indicate that the further away the object from the electrode plane, the less impact it would have on ERT measurement, i.e. less fringe effect. This agrees with the deductions made from the 3D circuit model for ERT that the smaller the resistance in a defined axial layer when the tube is filled with a uniform background medium, the more impact there would be on ERT measurement after introducing a specified object in this layer.

4.3.3 Non-centred non-conductive perturbation inside or outside sensor plane

The previous sections discussed about the fringe effect for a centred object with different lengths and conductivity inside or outside the ERT sensor. For generality, it is needed to investigate the fringe effect with a non-centred object with a variable length inside or outside the sensor plane. In the third and fourth sets of simulation, non-conductive objects with the same diameter as in the previous simulation were simulated

for this purpose. The position of these objects in the cross section is shown in Figure 4.2 (b), which is nearly half-way between the center and the tube wall. In the third set of simulation, objects were placed inside the sensor plane and their axial lengths were set to be 1, 10 and 19.8 cm for comparison. The simulated resistance after normalisation is shown in Figure 4.12 (a) together with the 2D reference.

Figure 4.12 (a) shows that the fringe effect decreases with the object length. Certain fringe effect still exists when the object length is the longest (19.8 cm), which is also the case for the centered object, because the electric field cannot be completely confined within the ERT sensor plane and would be axially non-uniform even with this axially uniform object distribution. It shows that the fringe effect in this case would change with the relative position of the injection and measurement electrode pairs to the object. The closer the injection electrode pair to the object and the larger part of the object lies between the two equi-potential lines defined by the measurement electrode pair as shown in Figure 4.6 (a), the more severe fringe effect would be in the corresponding normalised resistance. This may be explained by the fact that the small distance between the injection electrode pair and the non-conductive object would make the small equivalent resistance near the injection electrode pair, e.g. R_n in Figure 4.6 (a), increase greatly, if most part of the object lie between the two corresponding equi-potential lines. This would increase the elementary resistance between the corresponding measurement electrode pair, i.e. R_0 in Figure 4.7 (b), significantly and some resistance induced by the fringe effect above or below the sensor plane would be comparable with it. This would result in more current flowing outside and further away from the sensor plane, i.e. more severe fringe effect. If the injection electrode pair is far away from the object or the equivalent resistance between the measurement electrode pair is only slightly affected, only a slightly more current would flow outside, which means less fringe effect.

As mentioned in section 4.1, Wang (1999) found that the images reconstructed for a small object in the half-way between the centre and pipe wall and axially moving away from the sensor plane would move towards the centre of the sensor's cross section. This means that the artefacts produced by the objects far away from the sensor plane may influence the reconstructed image near the sensor centre. To investigate this phenomenon, objects were placed above the sensor plane by 0, 3 and 5 cm in the fourth

set of simulation and all set to be 4 cm in length. The corresponding normalised resistance from simulation is shown in Figure 4.12 (b).

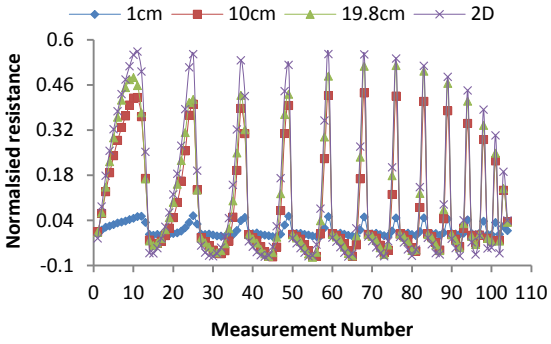

(a) Inside the sensor plane

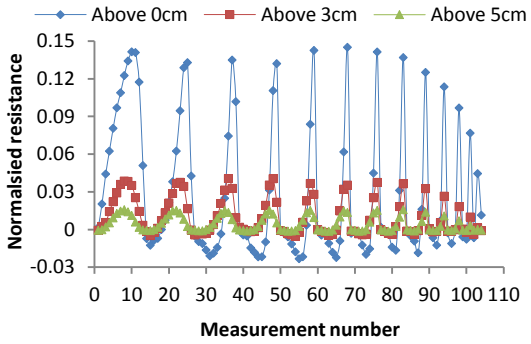

(b) Above the sensor plane

Figure 4.12 Normalised resistance for non-centred non-conductive object inside or above the sensor plane by different distance

Figure 4.12 (b) shows that with a fixed length, the further the object away from the electrode plane, the less fringe effect. This is consistent with the conclusion drawn from the previous simulation results. However, it is observed that the curve shape of the normalised resistance against the measurement number changes with the distance of the object from the sensor plane. With the distance of 0 cm, the shape of the curve is similar to that with the object inside the sensor plane as shown in Figure 4.12 (a). The further the object away from the sensor plane, the more similar the shape is to that with the centred non-conductive object inside the sensor as shown in Figure 4.9 (a), especially with the distance of 5 cm as shown in Figure 4.12 (b). This means that the reconstructed 2D image of the object would approach to the sensor centre with its axial distance from the sensor plane, which confirms the conclusion made by Wang (1999). However, the fringe effect would decrease rapidly with the increase in the distance of the object from the sensor plane, as indicated by the normalised resistance for the objects above the sensor plane by 0, 3 and 5 cm in Figure 4.12 (b). This makes it possible to reduce the fringe effect by compensation, which will be discussed in the next subsection.

4.3.4 Compensation for fringe effect in an ERT sensor

To reduce the fringe effect in ERT sensors, there are two possibilities: (1) incorporating guard electrodes to the sensor structure, e.g. driven or grounded end guards, and (2) using a compensation algorithm during image reconstruction. Since driven guards have

been proven to be ineffective in reducing the fringe effect of ERT sensors (Wang 1999) and the grounded end guards cannot be applied in ERT sensors with the current-injection and voltage-measurement strategy as discussed in Chapter 3, a possible compensation method is discussed in this subsection.

The previous simulation results, e.g. Figure 4.9 (a) and Figure 4.12 (a), show that it is possible to reduce the fringe effect by scaling the corresponding normalised resistance for non-conductive object of certain length inside the sensor, because those resultant curves of the normalised resistance have similar shape but different magnitudes, except for those with axially uniform distribution. In the case with an axially uniform distribution, there is a much less fringe effect. However, this is unlikely to happen in reality. For the object outside the sensor, they normally have less influence on the normalised resistance, compared with those with the same lengths but inside the sensor. Therefore, it is possible to reduce this kind of fringe effect by removing the resultant signals contained in the normalised resistance. To achieve both the above goals, selective scaling is a possible solution, to amplify signals after removing the small signal induced by the fringe effect. Note that the selective scaling is not necessary when the object is inside the sensor plane. For example, the normalised resistance for objects of 1 cm and 10 cm in Figure 4.9 (a) and Figure 4.12 (a) can be scaled directly by assigning the scaling factor with the ratio of the maximum values of the normalised resistance in the 2D and corresponding 3D cases. The results after scaling are shown in Figure 4.13. It shows that the fringe effect is reduced after scaling the normalised resistance accordingly. Reconstruction results reveal that the relative image errors after scaling is around 11% for both centred objects in Figure 4.13 (a), while the correlation coefficient reaches 99.9% in both cases. Compared with the corresponding results in Figure 4.9 (d), the relative image errors have been greatly reduced with negligible image distortion (indicated by the large correlation coefficients) after scaling. With the non-centred object, the relative image errors corresponding to the normalised resistance for 1 and 10 cm objects in Figure 4.12 (a) are 91.4% and 30.8%, respectively. After scaling, they are reduced to 36.4% and 15.3%, respectively, with correlation coefficients 91.5% and 98.8%, which means the image distortion is still negligible in both cases.

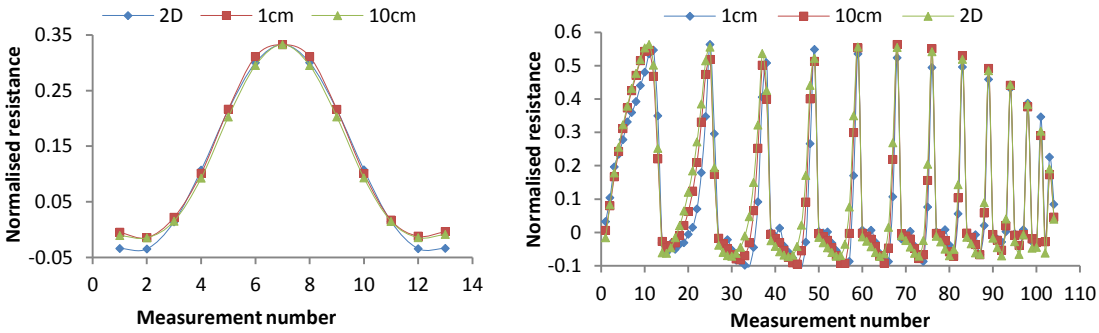

(a) Centred object

(b) Non-centred object

Figure 4.13 Normalised resistance after scaling for centred or non-centred non-conductive object inside the sensor

Another more difficult case is that two objects appear inside and outside the sensor plane at the same time. In this case, the selective scaling should be used to amplify the signal generated by the object inside the sensor plane and remove the unwanted signal induced by the object outside the sensor plane. Given a simple example, a centred non-conductive object with a length of 10 cm is placed inside the sensor plane while a non-centred non-conductive object with a length of 4 cm is positioned above the sensor plane by 3 cm, the cross-sectional and axial views of the two objects are shown in Figure 4.14.

With this object setup, the resultant normalised resistance is shown in Figure 4.15 (a) together with the 2D reference, the normalised resistance only with the centred non-conductive object of 10 cm inside the sensor plane (identified by "10cm" in Figure 4.15 (a) and the same as shown in Figure 4.9 (a)) and the normalised resistance only with the non-centred non-conductive object of 4 cm above the sensor plane by 3 cm (identified by "3cm" in Figure 4.15 (a) and the same as shown in Figure 4.12 (b)). Figure 4.15 (a) shows that the normalised resistance for the two objects is distorted due to the fringe effect, compared to that with the object of 10 cm inside the sensor plane. Apparently, the normalised resistance for the 2 objects is superposition of those identified by "10cm" and "3cm" in Figure 4.15 (a), but not exactly linear. It is natural to remove the fringe effect induced by the object outside the sensor plane by subtracting the resultant normalised resistance from the one for the 2 objects in Figure 4.15 (a). After subtraction, scaling is implemented (the scaling factor is the ratio of the maximum value of the normalised resistance in the 2D case to that in this case). The resultant normalised resistance is shown in Figure 4.15 (b) together with the 2D reference.

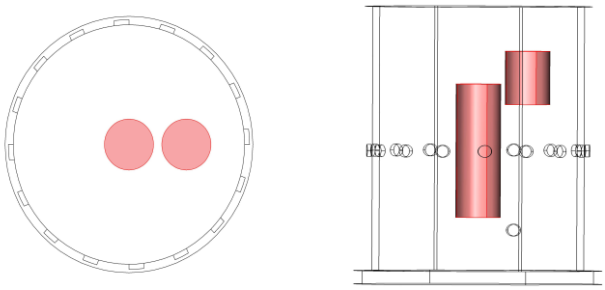

(a) Cross-sectional view (b) Axial view

Figure 4.14 Cross-sectional and axial views of two objects

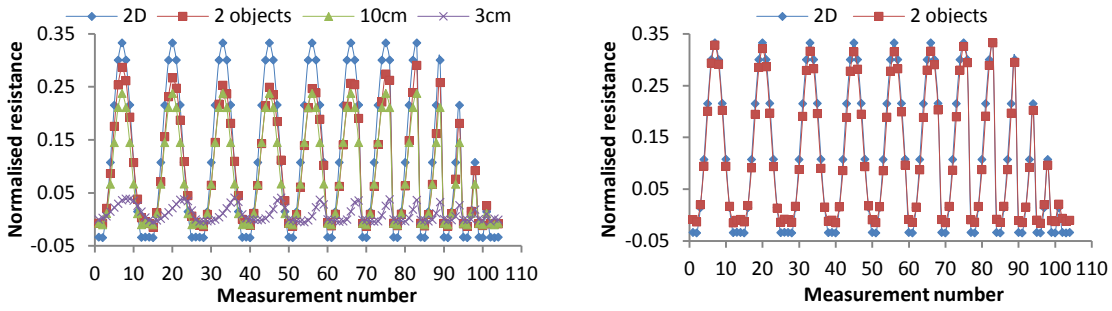

(a) Before compensation (b) After compensation

Figure 4.15 Normalised resistance for two objects before and after compensation for fringe effect

Figure 4.15 (b) shows that the fringe effect is reduced, compared with the corresponding results in Figure 4.15 (a). But small distortion for the normalised resistance still exists because the superposition is not exactly linear. Before the selective scaling, the relative image error corresponding to the normalised resistance for 2 objects in Figure 4.15 (a) is about 27%. It is reduced to about 13% with the correlation coefficient around 99.7% after the compensation when the image from the corresponding 2D model is used as the reference.

The above discussion indicates that the selective or direct scaling is effective in reducing the fringe effect. However, to obtain the fringe effect induced by the objects outside the sensor plane, another one or two auxiliary electrode planes are needed. Modelling of the flow patterns in an industrial process to be imaged is also necessary to acquire the 2D references for the related measurements, which is crucial for the calculation of the scaling factor. In some complicated and extreme circumstances, where the fringe effect

overwhelms or distorts the signal too much, it would be difficult to implement this compensation method.

4.4 Experimental verification of findings and proposed methodology

To validate the findings with the single-plane ERT sensor, experiment was carried out. For this purpose, an ERT system was built up, the block diagram of which is shown in Figure 4.16:

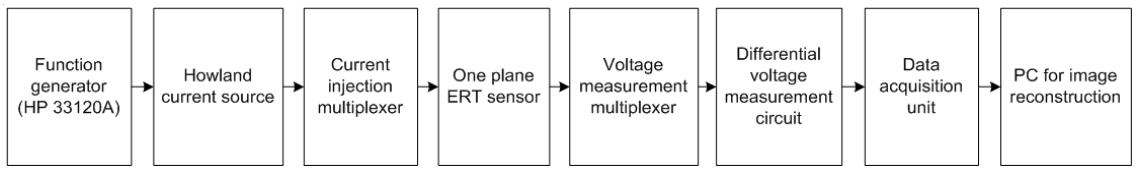

Figure 4.16 Experimental ERT system with a single-plane ERT sensor

As shown in Figure 4.16, the experimental ERT system is composed of 7 units:

- a function generator (HP 33120A),
- a Howland current source circuit,
- an ERT sensor,
- a differential voltage measurement circuit,
- a current-injection and voltage-measurement multiplexer module, the function of which is completed manually,
- a data acquisition unit (Agilent 34972A),
- a PC for data record and image reconstruction.

In this system, the adjacent current-injection and voltage-measurement strategy was adopted for data acquisition. The function generator was used to drive the Howland current source circuit to output a pair of differential sine-wave currents with almost the same amplitude. By multiplexing, this pair of differential currents is injected into a pair of adjacent electrodes of the ERT sensor. Again by multiplexing, the potential difference between each possible pair of adjacent electrodes is conditioned with a differential amplification circuit (amplified by 100 times through two stages with each stage 10 times) and then measured by the data acquisition unit. Note that the structure of the differential amplification circuit is the same as the internal structure of PGA202, which is

used as the second stage, while the first stage by two OPA602s to enhance the input impedance. Then each measurement is sent to the PC for image reconstruction via an USB interface. Finally an image is reconstructed in MATLAB using the data received.

In the experiment, the pair of differential currents has a peak-to-peak magnitude of around 1 mA, and nearly out of phase. The frequency of the injected AC current is 10 kHz. Note that the potential difference is also an AC signal and the data acquisition unit (Agilent 34972A) can only measure its root mean square (RMS) value. The amplitude of the AC voltage can be estimated from the measured RMS value by:

$$V_A = V_{RMS} \times Crest\ factor \tag{4.4}$$

where V_A is the amplitude of the AC voltage, V_{RMS} is the measured RMS value of the AC voltage, and $Crest\ factor$ is the ratio of the peak value to the RMS value of a waveform, which is calibrated to be 1.414 for the sine wave measured by the data acquisition unit (Agilent Technologies 2010).

Highly-matched resistors were used for the Howland current source circuit (10 kΩ resistors with 0.1% precision and manually matched with each other for a mutual difference less than 0.05%). Together with the high measurement accuracy of Agilent 34972A (maximum 6.5 digits), the measurement accuracy of the experimental system with the above simulation set-ups can be guaranteed. This will be confirmed by comparing with corresponding simulation results afterwards. Note that the common mode measurement error was reduced by the relatively high common mode rejection ration (CMRR) of PGA202 (around 70 dB at 10 kHz for a gain of 10) and grounding an unused electrode for reference. Also, high input impedance is guaranteed with the two op-amps OPA602s used in the first stage of differential amplification. The experimental set-up with two objects is shown in Figure 4.17 (the PC for image reconstruction is not shown). Note that before starting measurement with Agilent 34972A, a complete self-test was passed (Agilent Technologies 2010).

To validate the measurement accuracy of the experimental system, experiment was conducted when the tube was filled with the same uniform background medium as in the previous simulation, i.e. saline with conductivity of 0.02 S/m. The comparison between the 3D simulation and experimental results is shown in Figure 4.18.

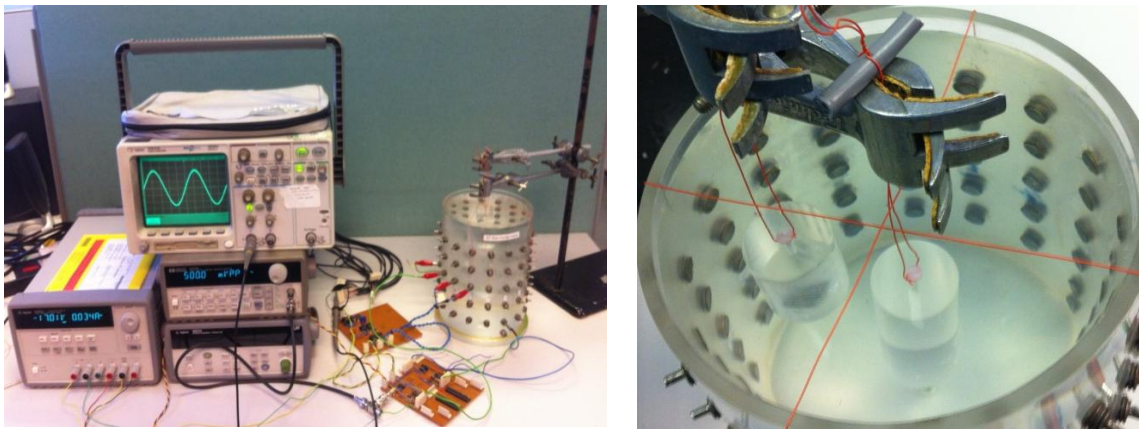

(a) System set-up (b) Two-object set-up

Figure 4.17 Experimental set-up with two objects

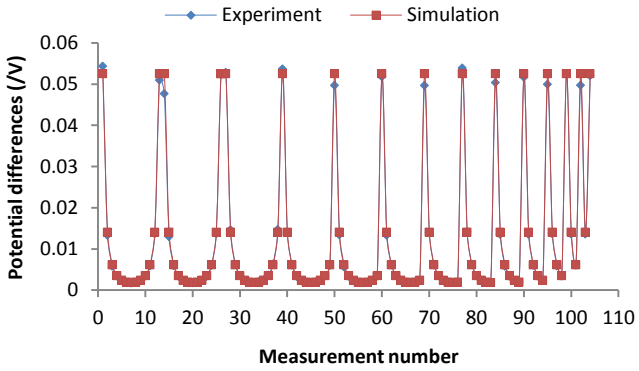

Figure 4.18 Comparison between 3D simulation and experimental results of potential difference with uniform background medium filling the tube

Figure 4.18 shows that there is a good agreement between the 3D simulation and experimental results of potential difference with a uniform background medium filling the tube. This confirms the measurement accuracy of the above experimental system and verifies that the contact impedance has negligible impact on the ERT measurement.

To verify the previous simulation results with centred and non-centred non-conductive objects inside or outside the sensor plane, experiment was carried out with similar set-ups as shown in Figure 4.2 (a) (centred) and Figure 4.2 (b) (non-centred) (referring to Figure 4.17 (b)). Perspex rods with certain lengths were placed at different axial and cross-sectional positions during the experiment accordingly. Note that for a non-centred distribution, the objects were placed at a different cross-sectional position from that in Figure 4.2 (b). The experimental results of normalised resistance are shown in Figure

4.19, where the legends like “4cm” indicate the lengths of the objects in the 3D simulation, “2D” indicates the result from the corresponding 2D simulation and those like “4cm(0)” suggest that the object with the specified length (4 cm) is placed above the sensor plane by the specified distance (0 cm from the top ends of electrodes). In Figure 4.19, the same conclusions can be drawn from those experimental results as from the previous simulation results. Apparently, the fringe effect for the objects inside the sensor plane, as shown in Figure 4.19 (a) and (b) can be compensated by direct scaling. The following part will focus on the compensation for fringe effect when the distribution with two objects as shown in Figure 4.17 (b) appears inside the tube. The experimental results of normalised resistance are shown in Figure 4.20 together with related 2D simulation and experimental results including that after compensation by selective scaling.

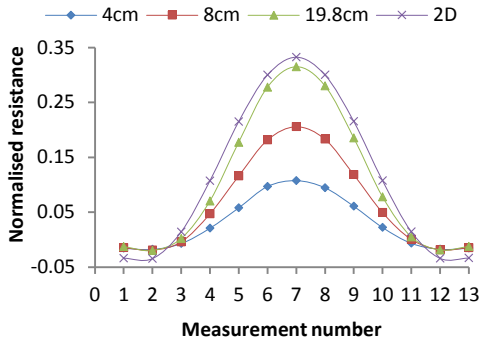

(a) Centred objects inside the sensor plane

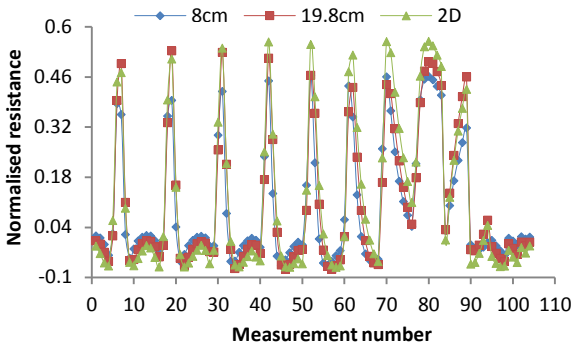

(b) Non-centred objects inside the sensor plane

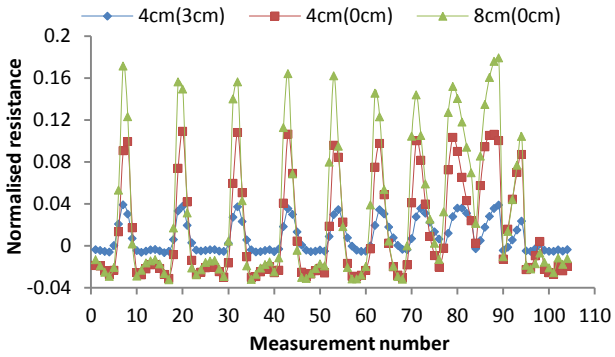

(c) Non-centred objects outside the sensor plane

Figure 4.19 Experimental results of normalised resistance for centred and non-centred non-conductive objects inside or outside sensor plane

In Figure 4.20, the legend “2 objects” represents the experimental result for the two objects. “8 cm(core)” is for the centred object with a length of 8 cm. “Compensated” indicates the normalised resistance after compensation for fringe effect. Other legends

have the same meanings as before. Note that the centred object ("8cm(core)") is not axially symmetric to the sensor plane but a little upward (by 1 cm), which explains why the normalised resistance in this case is a little different from that in Figure 4.19 (a). Figure 4.20 also shows that there is less fringe effect in the normalised resistance after compensation by selective scaling. This is consistent with the conclusions drawn from the previous simulation.

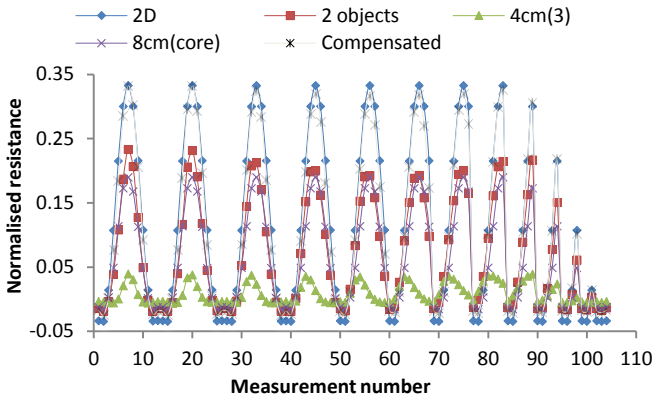

Figure 4.20 Experimental results of normalised resistance for the distribution with two objects and related 2D simulation and experimental results including the one after compensation

The above experimental results confirm that the previous 3D simulation results are valid, and validate the feasibility of the proposed methodology for the reduction of fringe effect. It is promising to use the direct or selective scaling to compensate for fringe effect, but difficulties still need to be addressed, e.g. the determination of the scaling factor by calibration and the more complicated distribution to be imaged in reality.

4.5 Test with three-plane ERT sensor scheme

As discussed previously, another one or two auxiliary electrode planes may be required to measure the fringe effect induced by objects outside the ERT sensor plane, which can be used to compensate for the fringe effect as described in the last section. This section will introduce a three-plane ERT sensor scheme for this purpose.

4.5.1 Simulation with three-plane ERT sensor scheme

A proposed sensor structure for ERT, i.e. a three-plane sensor scheme, is shown in Figure 4.21 with geometry parameters and material properties listed. The three electrodes planes of the ERT sensor can be denoted as the top, middle and bottom planes, respectively. The middle plane is mainly for image reconstruction, while the other two planes are auxiliary planes for compensation of the fringe effect induced by objects outside the sensor plane. Unlike the driven guards applied to ERT sensors, measurement is also taken from the top and bottom planes in the same way as in the middle plane. With the adjacent measurement strategy, a pair of adjacent electrodes in the middle plane is injected with a pair of differential current signal, while the two pairs of adjacent electrodes in the top and bottom planes above and below this electrode pair are injected with almost the same differential current signal, respectively. Note that the electrodes in the same column are injected with currents of the same polarity. Potential differences are measured in each electrode plane separately according to the measurement strategy. This process is repeated until all the independent measurements in each electrode plane are taken. In the simulation, each pair of differential currents has a peak-to-peak magnitude of 10 mA and exactly out of phase. The frequency of the injected AC current is 10 kHz.

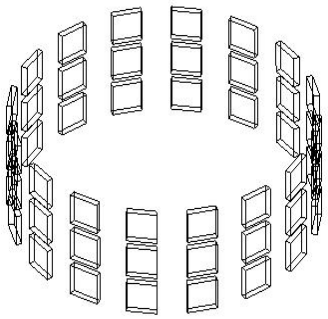

Figure 4.21 Three-plane ERT sensor

- Inner Diameter:10 cm
- Thickness of pipe wall: 3 mm
- Length of pipe: 50 cm
- Gap between adjacent planes: 5 mm
- Number of electrodes in each plane: 16
- Electrode size: 10 mm × 10 mm
- Number of electrode planes: 3
- Material of wall: Perspex
- Material of electrodes: Steel

From the electrical model shown in Figure 4.7 (b), it can be inferred that objects inside the middle plane of the above ERT sensor can be sensed by its three electrode planes at the same time. Objects above or below the middle plane can be sensed by the middle plane and top or bottom plane at the same time. Because these three electrode planes are

similar to each other in geometry and structure, it can be assumed that their responses towards the same object inside their sensing range are correlated to each other. Then, the fringe effect induced by objects above the middle plane may be compensated with the measurements from the top plane, while the fringe effect induced by objects below the middle plane may be compensated with the measurements from the bottom plane. The compensation can be made by subtracting the weighed measurement data before the normalisation for the top and bottom planes from the measurement data before the normalisation for the middle plane, as given in equation (4.5).

$$V_{ac} = V_m - WF * (V_t + V_b) \tag{4.5}$$

where V_{ac} is the measured vector of potential differences after compensation, V_m, V_t and V_b are the measured vectors of potential differences from the middle, top and bottom electrode planes, respectively, and WF is the weighting factor, which is a small positive scalar and initially determined based on trial-and-error for the optimum result.

The measurement data after the compensation is then normalised using the reference data acquired from the middle plane with conductive background medium filling the sensor. Note that the normalisation is done in the same way as in a conventional ERT (as described in Chapter 2). This compensation is only effective in reducing the fringe effect induced by objects outside the ERT sensor plane. For the axially non-uniform distribution with a single object inside the sensor, the fringe effect can be reduced by scaling as described in section 4.3. It was shown that the reconstruction algorithm with linear forward projection, e.g. LBP and Landweber iteration, tends to overestimate the size of a non-conductive object to be imaged when the distribution is axially uniform and this can be overcome with an FEM forward operator, which is computationally intensive (Giguère *et al*. 2008). The same goes for other non-linear forward operators as described in Chapter 2. It was found that the above compensation method can also help to reduce this kind of over-estimation by linear forward projection (e.g. Landweber iteration) at a less cost of time consumption when the distribution is axially uniform. Therefore, this section will only examine the axially uniform distribution with a single object or axially non-uniform distribution with multiple objects inside or outside the sensor plane. Unlike in the previous sections, the true distribution will be used as the reference image in this section instead of the qualitative image from the 2D simulation model using LBP, because the effectiveness of the compensation method needs to be

validated on reducing the over-estimation of the object size by Landweber iteration, not only the fringe effect.

With the above sensor structure, simulation was carried out. Three different setups were tested to evaluate the effectiveness of the three-plane ERT sensor on the reduction of fringe effect and overestimation by Landweber iteration. The cross-sectional views of the normalised true distributions for the three setups are shown in Figure 4.22.

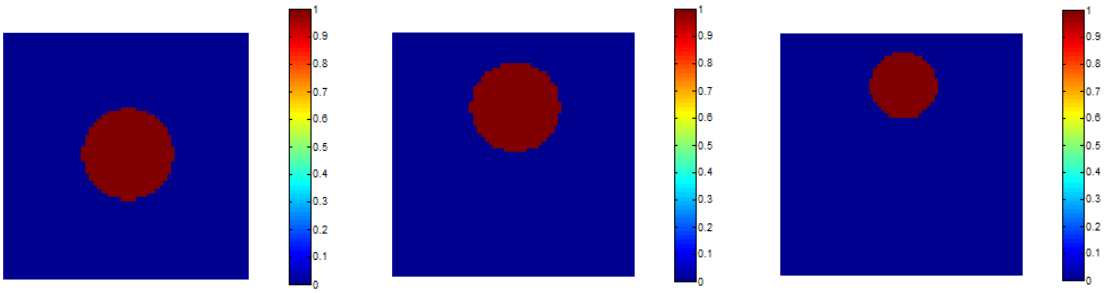

(a) A rod in centre (b) A rod near pipe wall (c) Three rods in different position

Figure 4.22 Normalised object distributions for simulation with three-plane ERT sensor

In Figure 4.22 (c), there are actually three rods distributed in different axial and cross-sectional positions, as shown in Figure 4.23 (a). But only the one marked with red colour in Figure 4.23 (b) is inside the middle plane for imaging with other two outside the middle plane. These three rods are of almost the same length and the same cross-sectional area. In all these setups, the rods are non-conductive with saline of conductivity 0.02 S/m as the background medium. The simulated potential differences acquired from the three sensor planes with the distribution in Figure 4.22 (c) are shown in Figure 4.24. It shows that the measurement data from different planes are correlated with each other. The fringe effect induced by objects outside the middle plane may be extracted from the measurements in the top and bottom planes. For the distribution in Figure 4.22 (a) or (b), the simulated potential differences acquired from the three sensor planes are similar to each other since the distribution is almost the same for all the planes.

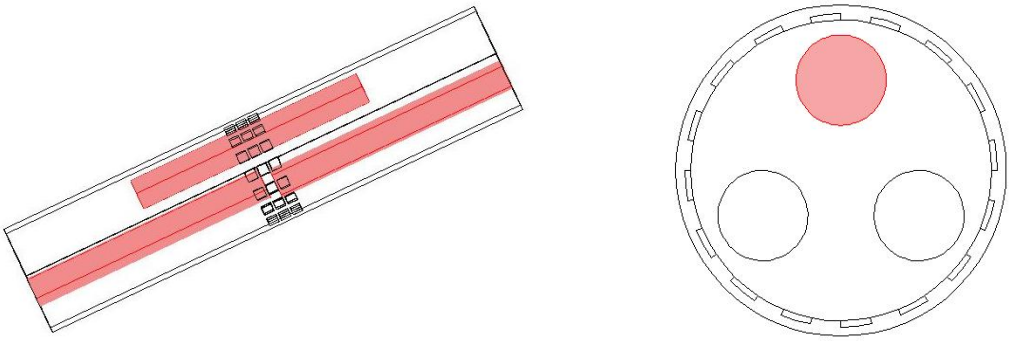

(a) 3D view (b) 2D view

Figure 4.23 3D and 2D view of three rods in different axial and cross-sectional positions with only one inside middle plane for imaging

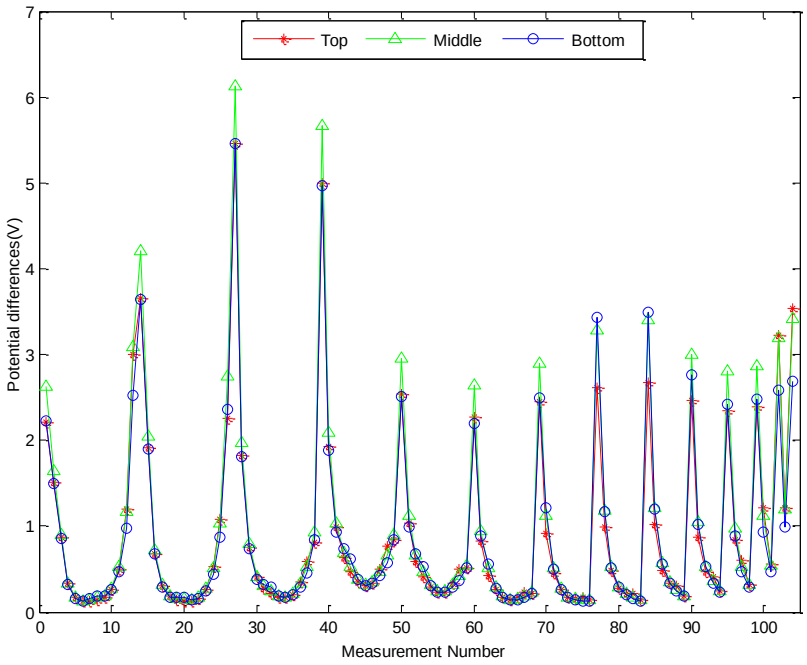

Figure 4.24 Simulated potential differences acquired from the three sensor planes with the distribution in Figure 4.22 (c)

Using the normalised data after the compensation and the projected Landweber iteration as described in Chapter 2, images are reconstructed for the above setups and shown in Figure 4.25 (a)~(c). For a comparison, the reconstruction results with a single-plane ERT sensor are shown in Figure 4.25 (d)~(f). Note that the single-plane ERT sensor is made up of only the middle electrode plane in the three-plane ERT sensor with other

geometry parameters unchanged. The weighting factors are 0.166, 0.101, 0.114 for the setups in Figure 4.22 (a), (b) and (c) respectively during the reconstruction.

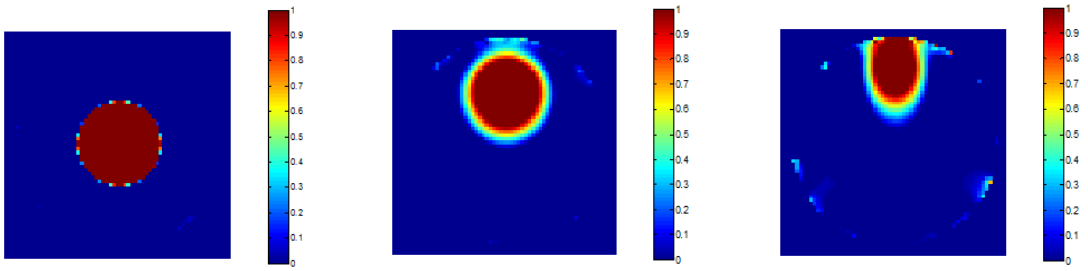

(a) A rod in centre (b) A rod near pipe wall (c) Three rods in different position

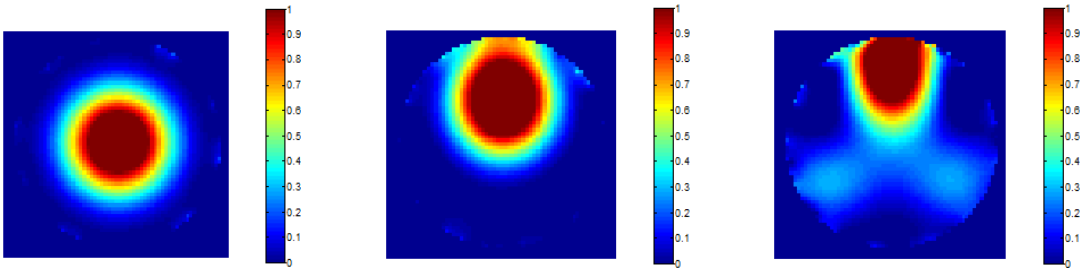

(d) A rod in centre (e) A rod near pipe wall (f) Three rods in different position

Figure 4.25 Reconstruction results for three simulation setups with the three-plane ERT sensor ((a)~(c)) or single-plane ERT sensor ((d)~(f))

The relative image errors and correlation coefficients of Figure 4.25 (a)~(f) regarding the respective true distribution are listed in Table 4.1 with the selection of relaxation factor and the number of iterations needed for each reconstruction using the projected Landweber iteration. Note that the relaxation factor is updated in each step according to the linear search method proposed by Liu *et al*. (1999) during the iteration. Figure 4.25 and Table 4.1 show that the over-estimation by Landweber iteration and the fringe effect induced by objects outside the measurement plane can be reduced with the three-plane ERT sensor scheme.

Table 4.1 The relative image errors and correlation coefficients of Figure 4.25 (a)~(f) regarding the respective true distribution

Subfigure number	(a)	(b)	(c)	(d)	(e)	(f)
Relaxation factor	α is updated in each iteration by linear search					
Number of Iterations	216	18	16	2	2	3
Relative image error (%)	6.7	34	57	57	65	93
Correlation coefficient (%)	99.7	93	81.8	85	81	73

Note that the stopping criterion for all the reconstructions is that the iteration will be stopped when the image error in current iteration step becomes larger than the one in the last iteration step. Therefore, those reconstructed images represent the local optimum for the corresponding distributions with the single-plane or three-plane ERT sensors. This indicates that the convergence is improved with the three-plane ERT sensor. From this point of view, the three-plane ERT sensor has the potential to reconstruct better images than the single-plane ERT sensor for non-conductive objects, although the number of iterations with the former may be much larger than that with the latter, especially for the first setup. However, it was found that if the required accuracy is not so high, e.g. 6.7% for the first setup with the three-plane ERT sensor, the iteration number can be reduced to a considerable extent (less than 100 iterations), which makes the fast and relatively accurate 2D reconstruction possible.

4.5.2 Experiment with three-plane ERT sensor scheme

An experimental system with a three-plane ERT sensor, as shown in Figure 4.26, is established to verify the simulation results. In this ERT system, the ERT sensor has three identical electrode planes with 3 cm gap between adjacent ones, the middle one of which is as shown in Figure 4.1. Other geometry parameters and material properties also stay the same as shown in Figure 4.1. Howland circuits are used to inject three pairs of differential currents into the three electrode planes at the same time with other electronics the same as in the previous experimental system. Each pair of differential currents has a peak-to-peak magnitude of around 1 mA and nearly out of phase. The frequency of the injected AC current is 10 kHz.

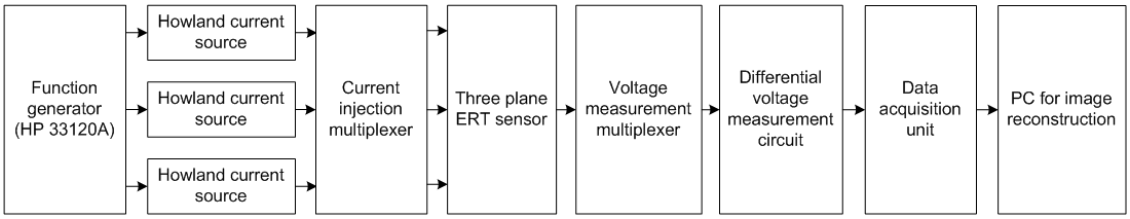

Figure 4.26 Experimental ERT system with a three-plane ERT sensor

Three object distributions similar to those used in the simulation were setup in the experiment, i.e. a rod in centre, a rod near pipe wall and three rods in different axial and cross-sectional positions. The cross-sectional views of the normalised true distributions in the three setups are shown in Figure 4.27.

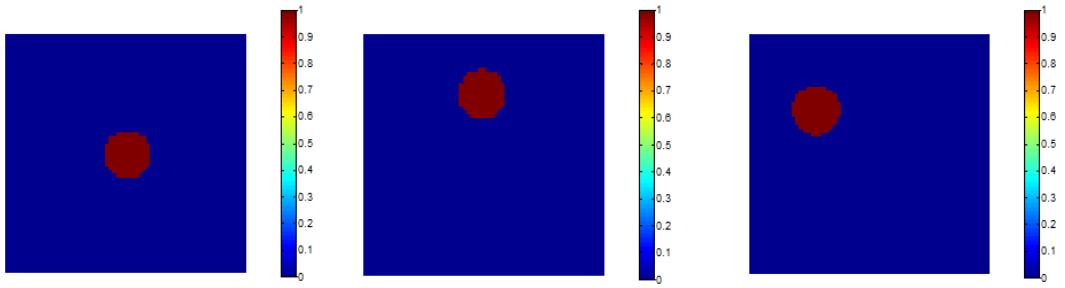

(a) A rod in centre (b) A rod near pipe wall (c) Three rods in different position

Figure 4.27 Normalised object distributions tested with three-plane ERT sensor

In Figure 4.27, all the rods are non-conductive with saline of conductivity 0.023 S/m as the background medium (the distance of the saline surface from the tube top is around 1.5 cm). These cylindrical rods for imaging have a diameter of 3 cm and a length of 20 cm. Note that in Figure 4.27 (c), only the rod inside the middle plane is shown, which has a length of 20 cm. The other two rods have the same diameter of 3 cm and a length of 8 cm and placed above and below the middle plane respectively and at different cross-sectional positions similar to that in Figure 4.23. They are away from the top or bottom ends of the electrodes in the middle plane by around 2 mm. With the proposed three-plane ERT sensor scheme, the reconstruction results using the projected Landweber iterations for those three setups are shown in Figure 4.28 (a)~(c). For comparison, the reconstruction results with a single-plane ERT sensor are shown in Figure 4.28 (d)~(f). Note that the single-plane ERT sensor is the same as shown in Figure 4.1. The weighting factors are 0.05, 0.09 and 0.03 for the setups in Figure 4.27

(a), (b) and (c) respectively during the reconstruction. The relative image errors and correlation coefficients of Figure 4.28 (a)~(f) regarding the respective true distribution are listed in Table 4.2 with the selection of relaxation factor and the number of iterations needed for each reconstruction using the projected Landweber iteration. Note that the relaxation factor is updated in each step according to the linear search method proposed by Liu *et al*. (1999) during the iteration.

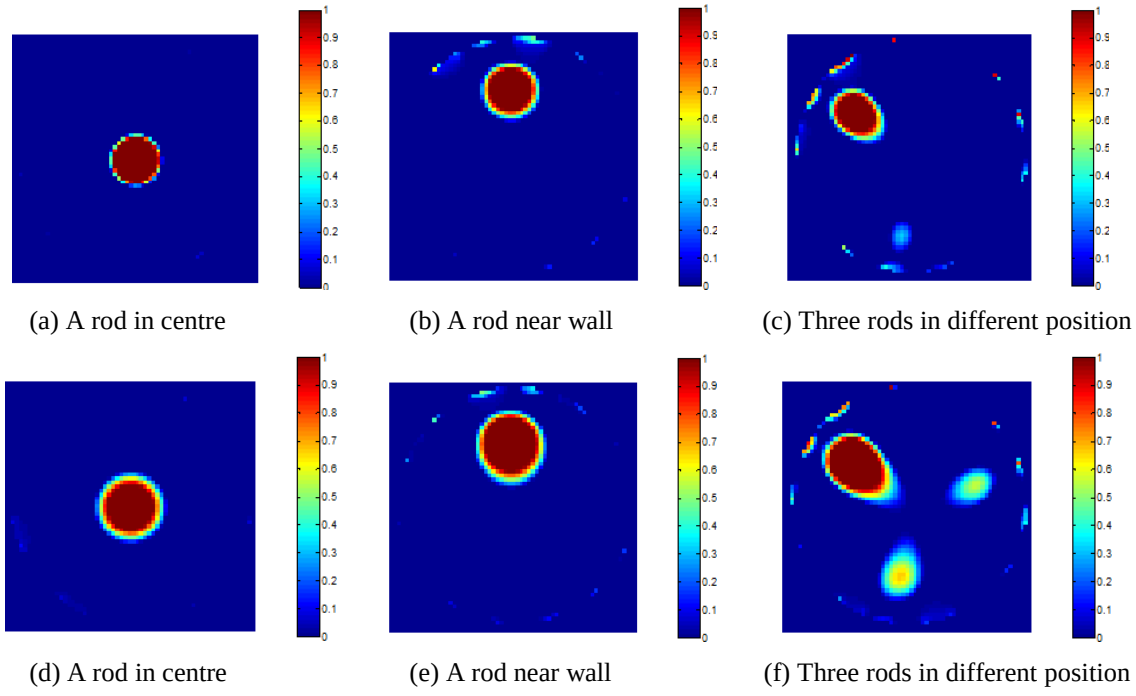

(a) A rod in centre (b) A rod near wall (c) Three rods in different position

(d) A rod in centre (e) A rod near wall (f) Three rods in different position

Figure 4.28 Reconstruction results for three experimental setups with the three-plane ERT sensor ((a)~(c)) or single-plane ERT sensor ((d)~(f))

Table 4.2 Relative image errors and correlation coefficients of Figure 4.28 (a)~(f) regarding respective true distribution

Subfigure number	(a)	(b)	(c)	(d)	(e)	(f)
Relaxation factor	α is updated in each iteration by linear search					
Number of iterations	200	100	100	200	100	100
Relative image error (%)	18.7	34.8	49.5	54.2	76	81.1
Correlation coefficient (%)	98.2	93.8	86.6	87.2	78.7	76.2

From Figure 4.28 and Table 4.2, it is obvious that the three-plane ERT sensor scheme can reduce the over-estimation by Landweber iteration with all the distributions and the fringe effect induced by objects outside the sensor plane, which improves the quality

and accuracy of reconstructed images greatly. This is consistent with the conclusion drawn from the previous simulation.

4.5.3 Determination of weighting factor by linear search

The compensation before the normalisation process is crucial for the reduction of the fringe effect and over-estimation by Landweber iteration. It is important to determine the weighting factors for the compensation adaptively, because all the weighting factors used previously are manually determined based on trial-and-error. A simple solution is to use a linear search method. It can be inferred that the weighting factor lies between 0 and 1 since the fringe effect or over-estimation only accounts for a portion of the measured signals from the auxiliary electrode planes. Therefore, the search can begin with an initial value 1 for the weighting factor, and the resultant potential residual is calculated after one iteration with Landweber iteration. Then the weighting factor is reduced by half. If the resultant potential residual with the current weighting factor after one iteration is smaller than that with the previous one, the search will continue by further reducing the weighting factor by half and calculating the resultant potential residual after one iteration. This process will continue until the potential residual with the present weighting factor after one iteration is larger than that with the previous one, which is taken as the final weighting factor. The potential residual can be expressed as:

$$\| V_r \| = \| V_n - S * g \| \tag{4.6}$$

Where V_r is the vector of potential residual, V_n is the normalised vector of potential differences after trial compensation, S is the sensitivity matrix of the ERT sensor, and g is the reconstructed image vector of the distribution after one iteration with Landweber iteration.

Simulation and experiment show that the weighting factor obtained in this way is not the optimal, but it is accurate enough to reduce the fringe effect of the sensor and the over-estimation by Landweber iteration to an acceptable level, which is a little higher than that with the optimum weighting factor obtained manually. It is also beneficial for the reduction in the number of iterations since less accurate images are reconstructed. However, further simulation and experiment are needed to verify the effectiveness of this technique.

4.6 Summary

The objective of this chapter was to evaluate the fringe effect with a single-plane ERT sensor for some simple but typical distributions, e.g. with objects centred or non-centred and inside or outside the sensor plane, which are also variable in axial length and not axially uniform in most cases. The goal was to illustrate to what extent an ERT sensor is affected by the fringe effect in these situations and try to draw some generalised conclusions, which may be used for compensation of the fringe effect. A 3D simulation model was established, and experiments were conducted to validate this model and the conclusions drawn from the related simulation results as well as the methodology proposed for compensation of fringe effect. Finally, a three-plane sensor scheme was also tested for reducing the fringe effect induced by objects outside the measurement sensor plane and over-estimation of object size by Landweber iteration.

In the beginning, the difference between the electrical models for ERT and ECT was analyzed to explain why an ERT sensor with “pin” electrodes has negligible fringe effect for an axially uniform distribution. This explanation was further confirmed by the corresponding simulation. For axially non-uniform distributions inside the sensor discussed in this chapter, i.e. centred or non-centred single object with a length shorter than that of the tube, less fringe effect would occur with longer objects while the curve of the normalised resistance against measurement number is of similar shape to the 2D one in all the cases. For a single non-conductive object outside the sensor plane, either centred or non-centred, its induced fringe effect would decrease with its distance from the sensor plane for a specified axial length, but increase with its axial length for a specified distance. For two non-conductive objects, one centred and inside the sensor plane while the other non-centred and outside the sensor plane, the resultant resistance after normalisation is the superposition of the normalised resistance when each object appears separately.

In view of the above conclusions, a compensation method for the fringe effect was proposed, i.e. selective scaling of the normalised resistance regarding the corresponding 2D reference. Both simulation and experiment proved the feasibility of the method using a simple setup with two objects. Accordingly, an ERT sensor scheme with two auxiliary electrode planes was proposed to compensate for the fringe effect induced by the objects outside the measurement sensor plane and reduce the over-estimation of

object size by Landweber iteration. Simulation and experiment manifested that the three-plane sensor can reconstruct much better image than the corresponding single-plane sensor. Further tests are still needed to validate this scheme with more complicated distributions, e.g. the fringe effect induced by objects outside the measurement sensor plane is more severe and overwhelms the signal.

Chapter 5: Application of fringe effect in 3D imaging with ECT

This chapter will explore the principle for fringe-effect-based 3D imaging of a single object of regular shape with a conventional single-plane ECT sensor. Fringe effect contained in the normalised capacitance is examined to estimate the axial position of the object to be imaged. Reconstruction is carried out to generate the 2D image of the object, the centre of which can be located with certain algorithms. Finally, the obtained 3D position of the object inside the ECT sensor is used to reconstruct the 3D image of the object by incorporating the prior knowledge about the object shape and size. This principle can also be applied to the 3D imaging with ERT or EMT since they have similar sensing principle and fringe effect to ECT.

5.1 Introduction

Although 3D imaging by a single-plane ECT/ERT sensor has been attempted, either the position or the shape of the object cannot be correctly reconstructed (Cao and Xu 2013, Soleimani *et al*. 2007). Usually, to implement 3D imaging with a reasonable resolution, a very large number of unknowns or voxel values need to be resolved with a small number of independent measurements from an ET sensor. With a single-plane ET sensor, the number of independent measurements is limited, e.g. 28 for an 8-electrode ECT sensor, which results in a severely ill-conditioned and ill-posed inverse problem. Therefore, multi-plane ET sensors are usually adopted by researchers to increase the number of independent measurements for improved 3D image quality. Soleimani *et al*. (2007) and Li (2008) showed that the increase in the number of electrode planes in an ECT sensor would improve the quality of 3D imaging since more independent measurements are acquired. On the other hand, more independent measurements would lead to a very large sensitivity matrix needed for reconstruction. It takes a very long time to obtain the approximated inverse of such a large sensitivity matrix as done in most conventional reconstruction algorithms. This means that the real-time performance is not satisfactory in this case. To reduce the number of unknowns for 3D imaging, a type of shape-based or model-based method was proposed (Banasiak *et al*. 2010, Ren *et al*. 2014). Banasiak *et al*. (2010) used FEM to calculate the capacitance from the reconstructed permittivity distribution, and a two-stage level set method to do the shape

reconstruction. Ren *et al*. (2014) used BEM to solve the forward problem and the Levenberg-Marquardt (L-M) method to do the reconstruction with a fast calculated Jacobian matrix, which is based on the shape parameterisation coefficients of the inclusion to be imaged using spherical harmonics. Although promising results were obtained along with the incorporation of a regularisation or constraint based on the prior knowledge during the reconstruction in both the researches, they adopted a multi-plane or true 3D ECT sensor for the 3D imaging and the FEM and BEM for solving the forward problem are still time-consuming during the iteration. The inspiration is that the incorporation of prior knowledge about the object to be imaged and the model-based methods can be adopted to reduce the number of unknowns to be solved during 3D reconstruction and improve the image quality.

In the last chapter, it was found that the fringe effect is related to the axial object distribution (i.e. the axial position and length of an object) for a conventional single-plane ERT sensor. Similar conclusions can also be drawn for a conventional single-plane ECT or EMT sensor as they have similar sensing principles to ERT. This indicates that the axial position of an object to be imaged may be derived by examining the corresponding fringe effect. Along with conventional 2D imaging techniques, it is possible to achieve accurate 3D imaging with a single-plane ET sensor for an object with regular shape and known size. This is different from all other 3D reconstruction methods in ET since fringe effect has never been exploited during the 3D imaging process. With this method, only a single-plane ET sensor is needed to determine the cross-sectional and axial positions of the object to be imaged using conventional 2D imaging techniques and calibration methods. The 3D image can then be reconstructed by incorporating the prior knowledge and the derived 3D position. Since the proposed method is simple and fast, it may find applications in the real-time visualisation and monitoring of certain processes. For example, an ageing population has led to a dramatic rise in the number of total hip replacements being carried out. Due to mechanical failures or other reasons, revision surgery is necessary for many patients, 10 years after the total hip replacement. To do the revision surgery, the bone cement must first be removed, which is a difficult and intricate procedure. Navigated drilling or milling tools are being developed to remove the bone cement efficiently and replace the hip prosthesis without injuring the bone (Brendle *et al*. 2012a). To do the real-time visualisation for navigation, ET may be applied since the milling bit is usually made of

metal, the electrical property of which is different from human tissues and bone cement, and the measurement of its movement can be regarded as a multi-phase flow measurement. Because the milling bit is regular in shape and its dimensions are known prior to the reconstruction, only its 3D position needs to be determined, which enables the method proposed above to be applied. In this chapter, the feasibility of the proposed 3D imaging method is investigated with a single-plane ECT sensor for the imaging of a metallic rod. In the beginning, the principle for imaging metallic objects with ECT is introduced. Simulation was conducted to illustrate the fringe effect with a centred dielectric or metallic rod at different axial position. After analysing the change pattern of the fringe effect with the axial position of a metallic rod, a strategy is proposed to determine its 3D position with a single-plane ECT sensor. With experimental data, the 3D imaging process of the metallic rod surrounded by table salt or deionised water is presented and related estimation errors of the 3D coordinates of the rod head are examined in each case with different derivation methods. Subsequently, the calibration issues regarding the determination of the axial position of the rod are discussed. Finally, an initial test is briefly introduced for the imaging of a metallic rod inside the main bone of a pig shank using the proposed 3D imaging method.

5.2 Principle of 3D imaging of dielectric or metallic rod with a single-plane ECT sensor

5.2.1 Forward simulation models for an ECT sensor

In ECT, the forward problem is to calculate the capacitance between different electrode combinations from the known permittivity distribution inside the sensor. As described in Chapter 2, FEM can be used for simulation, which can generate noise-free capacitance measurements and help discover the change pattern or prior knowledge contained in the measurements before conducting experiment. The simulation model of an ECT sensor is shown in Figure 5.1. Note that the bottom of this ECT sensor is actually sealed. The tube wall and electrodes are made of glass and copper respectively.

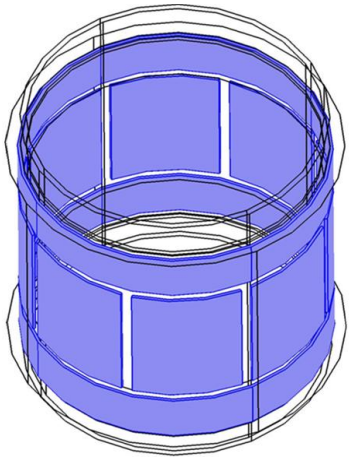

Figure 5.1 ECT sensor

- Inner Diameter:10.2 cm
- Thickness of wall: 2 mm
- Shield diameter: 11.6 cm
- Length of electrode: 6 cm
- Length of grounded guard: 2.2 cm
- Length of shield: 11.6 cm
- Length of wall: 14.6 cm
- Gap between adjacent electrodes: 4 mm
- Gap between electrodes and guards: 4 mm
- Number of electrodes: 8

To fully illustrate the change of fringe effect with the penetration depth of the object into the ECT sensor, three changes were made to the ECT sensor in Figure 5.1 for the simulation purpose:

(1) The length of the tube wall is extended symmetrically to 30 cm;
(2) Grounded end guards are removed to enlarge the axial sensing range;
(3) The outer shield is 1 cm longer than the electrodes at each end.

Other geometry parameters and material properties remain the same as in Figure 5.1. The 2D and 3D simulation models are shown in Figure 5.2 with object distribution.

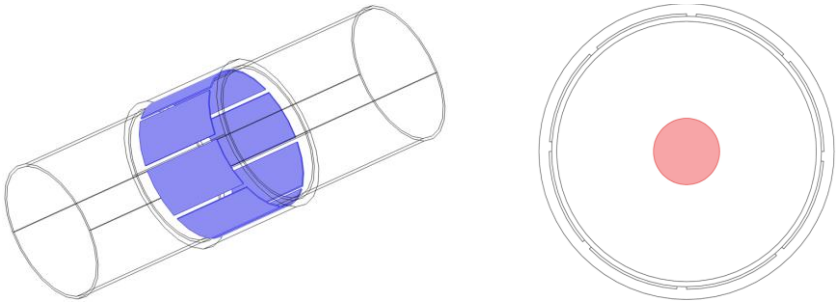

(a) 3D (b) 2D

Figure 5.2 2D and 3D simulation models with object distribution

With the object distribution shown in Figure 5.2 (b), the length of the object and the axial position of the object head in the 3D simulation change with respect to the axial dimension of the ECT sensor. The top end of the sensor electrodes is referred to as the axial origin. Two objects of two kinds of materials were chosen to be simulated, i.e.

dielectric and metallic rods, when surrounded by different background materials. The dielectric object (Perspex rod) has a diameter of 3 cm with a relative permittivity of 2.56, while the diameter of the metallic object (Aluminium rod) is 2.6 cm. For simulation with the dielectric rod, air acts as the background as well as the low permittivity material for calibration while the high permittivity material for calibration has a relative permittivity of 1.8. For simulation with the metallic rod, the low and high permittivity material for calibration remain the same while the latter is used as the background. The 2D ECT sensor in Figure 5.2 (b) is used in all the subsequent 2D simulation to obtain sensitivity maps and corresponding 2D references. Note that all the simulation was carried out in COMSOL Multiphysics with the "In-Plane Electric Currents" mode in the 2D case and "Electric Currents" mode in the 3D case, both of which are in AC/DC module with 1 MHz as the excitation frequency. In the 3D simulation, tetrahedral elements and direct solver (SPOOLES) are used. The number of elements used in the 3D simulation is of the order of 90,000.

5.2.2 Principle for imaging metallic object with ECT

ECT is usually used to image dielectric material distribution since the measured capacitance values between different electrode pairs are mainly determined by the dielectric property (i.e. permittivity) of the materials under investigation for a specified distribution. A type of planar capacitance sensor was once utilised to detect the dangerous metallic items placed above the sensor, e.g. a metallic knife hidden in airline passenger's shoes. Two different modes can be adopted during the detection: floating and shunt mode both of which have their respective merits (Hu 2009). Up to now, almost no literature reported the application of ECT sensors with circular shape in the imaging of metallic objects. Situations may be different in this case since different sensor structures and measurement principles are involved. According to our experimental results, the measured capacitance values change unstably and irregularly with the distance of the detection electrode from the excitation electrode when a floating metallic rod presents in the sensing domain. This may be because the electric potential on the metallic rod would change randomly with the changes of surroundings and the rod is a little far away from the sensor electrodes, which is not the case in the detection of metallic objects with a planar capacitance sensor. With the shunt mode, however, the measured capacitance values between different electrode pairs have a regular decrease

regarding the position of the grounded metallic rod inside the sensor, because the surface of the grounded rod acts as another capacitor plate, which blocks or sinks part of the electric field lines transmitted from the excitation electrode to the detection electrode. The simulated electric field and potential distribution with a grounded metallic rod in the centre of the 2D ECT sensor is shown in Figure 5.3 (a). Note that the background material in the simulation has a relative permittivity of 1.8 and an AC voltage signal of 1 V is applied to the excitation electrode.

In Figure 5.3 (a), the red lines scattered from the excitation electrode represent the electric field lines while the multi-coloured closed curves around the excitation electrode represent the equi-potential lines. Note that the colour bar shows the potentials represented. In view of the above points, the metallic rod is grounded in both simulation and experiment for effective measurement. With the grounded metallic rod in the centre of the 2D sensor as shown in Figure 5.3 (a), the first 7 values of the simulated normalised capacitance of a whole frame are illustrated in Figure 5.3 (b).

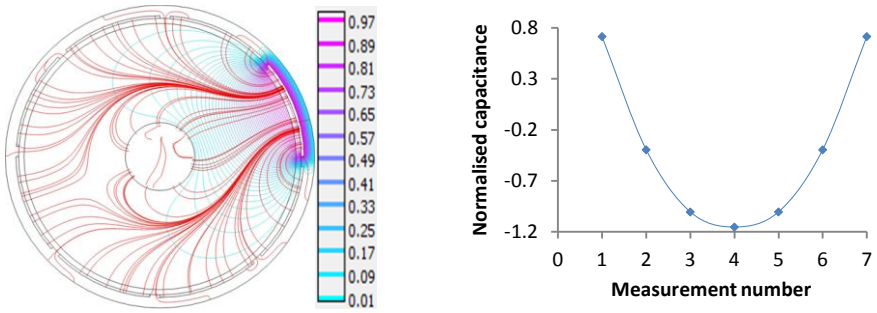

(a) Electrical field and potential distribution (b) Normalised capacitance

Figure 5.3 Simulated electric field and potential distribution and normalised capacitance for a grounded metallic rod in centre of a 2D ECT sensor

Because the high permittivity material is used as the background in the simulation, the value of 1.0 can be taken as the reference for the normalised capacitance between different electrode pairs. Figure 5.3 (b) shows that the absolute difference between the normalised capacitance and its reference is the maximum with the opposite electrode pair (indentified by measurement number 4 in Figure 5.3 (b)) and the minimum with the adjacent electrode pair (indentified by measurement number 1 or 7 in Figure 5.3 (b)). The further the detection electrode is away from the excitation electrode, the larger this absolute difference would be. This is similar to the case when a dielectric rod with high

permittivity is positioned in the centre of the same 2D ECT sensor with air (low permittivity material) as the background, except for the direction of capacitance change. This means that the cross-sectional position of the metallic rod can be reconstructed with a conventional algorithm for ECT.

5.2.3 Fringe effect for dielectric or metallic rod at different axial position

To examine the fringe effect at different axial positions, the head of the dielectric rod was placed from above the top end of the sensor electrodes by 4 cm to below the bottom end of the sensor electrodes by 4 cm with 2 cm as the interval. In this case, 8 axial positions were simulated, denoted as position 0 to 7 from the top to the bottom. The head of the metallic rod was positioned from above the top end by 10 cm to below the bottom end by 10 cm with 2 cm as the interval, denoted as position 0 to 13 similarly. With the 3D sensor model and distribution shown in Figure 5.2, the simulated capacitance after normalisation can be acquired for the dielectric or metallic rod at each specified axial position. To quantify the fringe effect, the corresponding 2D simulation result is obtained with the 2D sensor model as shown in Figure 5.2 (b) and used as the reference. To make it simple and straightforward for calculation, the averaged capacitance change after normalisation is used for the quantification of fringe effect. With the dielectric object, the fringe effect is evaluated by

$$C_f = (C_{2D} - C_{3D})/C_{2D} \tag{5.1}$$

where C_{2D} and C_{3D} are the corresponding averaged capacitance after normalisation of a whole measurement frame for the dielectric rod at specified cross-sectional and different axial positions with the 2D and 3D sensor models, respectively. With the metallic object, the fringe effect is defined as

$$C_f^{'} = ((1 - C_{2D}^{'}) - (1 - C_{3D}^{'}))/(1 - C_{2D}^{'}) \tag{5.2}$$

where $C_{2D}^{'}$ and $C_{3D}^{'}$ are the corresponding averaged capacitance after normalisation of a whole measurement frame for the metallic rod at specified cross-sectional and different axial positions with the 2D and 3D sensor models, respectively. The calculated fringe effect in each case is shown in Figure 5.4 (a) and (b), respectively:

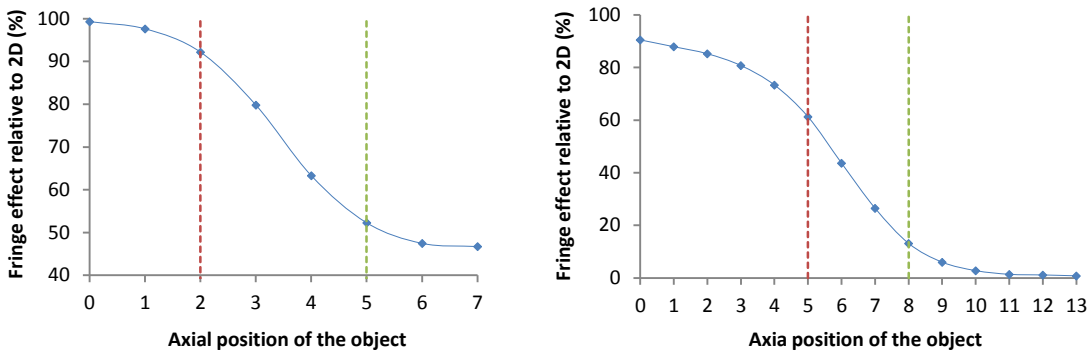

(a) Dielectric rod (b) Metallic rod

Figure 5.4 Change of fringe effect with axial position of dielectric (a) or metallic (b) rod in centre of sensor

In Figure 5.4, the dotted vertical lines represent the top (red) and bottom (green) ends of the sensor electrodes. It is shown that the fringe effect decreases when the rod moves downwards. The closer the rod head is to the middle cross-section of the sensor, the faster the fringe effect decreases with the downward movement. It is noticed that the change rate of the fringe effect with the movement of the rod above the top end of sensor electrodes is a bit larger than that below the bottom end of sensor electrodes regarding the axially symmetric positions to the sensor's middle cross-section. This may be because both dielectric and metallic rods would draw electric field lines to themselves. When the rod is above the top end of electrodes, the fringe effect would increase. When it is below the bottom ends, the fringe effect would decrease. This also results in the axial sensing range above the top end being larger than that below the bottom end. It shows that the axial sensing range for the metallic rod is larger than that for the dielectric rod, especially above the top end. This may be because the grounded metallic rod would act as a greater sank for electric field lines than the dielectric rod, i.e. it would draw more electric field lines to itself from a further distance. This leads to the fringe effect being much smaller when the head of the metallic rod reaches the bottom end of the electrodes (the green line in Figure 5.4 (b)) than that for the dielectric rod.

To reduce the interferences of surroundings in the capacitance measurement, grounded end guards are usually applied to ECT sensors as shown in Figure 5.1. This would narrow the axial sensing range of an ECT sensor (Yan *et al*. 1999), i.e. the dielectric or metallic rod cannot be sensed outside this axial range, which is smaller than the respective range for the horizontal coordinate shown in Figure 5.4 (a) and (b). In this

situation, it is not feasible to implement the 3D imaging with a single-plane ECT sensor based on fringe effect. Figure 5.4 implies that it had better determine the axial position of the rod in the nearly linear region of the curve, e.g. when the rod head moves from the top end (referred to as the axial origin) to the bottom end of the electrodes, with less error. To make it simple and accurate, the axial position of the rod head is measured when it moves axially within the volume enclosed by the electrodes. To achieve this, the change pattern of the fringe effect with the axial position of the rod needs to be determined before 3D imaging. By examining the curve part between the top and bottom ends of the electrodes in Figure 5.4 (a) and (b), it is found that the data may be well interpolated with a polynomial, the order of which needs to be determined by experiment. This means that only several calibration points of fringe effect with the rod at certain axial positions are needed to derive the interpolation polynomial, which describes the change pattern of the fringe effect with the axial distance of the rod head from the axial origin. However, the difficulty is that the change pattern would be different for the rod at different cross-sectional positions.

5.2.4 Change pattern of fringe effect with axial position of rod at different cross-sectional positions

To explore the change pattern of the fringe effect with the axial position of an object, a metallic rod is placed at three different cross-sectional positions as shown in Figure 5.2 (b) and Figure 5.5 (a) and (b), which are denoted as centre, midway1 and edge1 respectively. Both simulation and experiment were conducted. The impendence-analyser-based ECT system as described in Chapter 2 was used in the experiment. The detailed description of the experiment setups except for the distribution can be found in section 5.3. Note that because the experimental system has a limited accuracy for capacitance measurement (referred to Hu *et al*. (2008)) and is more sensitive to grounded metallic objects than dielectric ones, only 3D imaging of a metallic rod is discussed in the following sections. Dielectric objects can be reconstructed in a similar way with a more accurate measurement system.

(a) Midway1 (b) Edge1

Figure 5.5 2D views of two object distributions examined in simulation for change pattern of fringe effect with the axial position of the rod

With the object distributions shown in Figure 5.2 (b) and Figure 5.5 (a) and (b), the length of the rod and the axial position of its head change as required in each 3D simulation. The 3D simulation model is the same as shown in Figure 5.1 with grounded end guards applied. A material with relative permittivity of 1.8 and air are used as the high and low permittivity materials for calibration during the simulation. The acquired fringe effect with the rod at the centre or midway1 or edge1 in the cross-section of the sensor, is shown in Figure 5.6 (a) for comparison. Note that the rod head moves axially from the top end to the bottom end of the electrodes. Only the fringe effect at four test points is simulated because it is found that a third-order polynomial by data interpolation is good enough to describe the change pattern of the fringe effect with the axial distance of the rod head from the origin. This will be verified later by experiment.

Figure 5.6 (a) shows that the change pattern of the fringe effect with the axial distance of the rod head from the origin is slightly different when the rod is at different cross-sectional positions. The further the rod is from the sensor centre, the faster the change will be. This means that this change would depend on the cross-sectional distance of the rod from the sensor centre, which can be obtained by examining the reconstructed 2D image of the rod. Another interesting phenomenon is that the proportion of the fringe effect change within each interval of axial distance in Figure 5.6 (a) (i.e. 2 cm increase) to the total change within the whole measurement range, keeps constant. This makes it possible to determine the change pattern of the fringe effect with the axial position of the rod at any cross-sectional position by knowing the corresponding start (at 0 cm in Figure 5.6) and stop values (at 6 cm in Figure 5.6) of the fringe effect at this position and the change pattern of fringe effect with the rod at a specified cross-sectional position, e.g. in the sensor centre. The start value can be obtained by calibration in the

beginning of measurement. The stop value, however, is almost impossible to be attained through calibration since it has to be identified by measurement. However, the stop value does not change so much with the rod at different cross-sectional positions as shown in Figure 5.6 (a), i.e. 7.43%, 6.83% and 6.36% for the rod at the centre, midway1 and edge1 respectively. Thus one possible method to obtain the stop value is to assume that it is constant with the rod at any cross-sectional position, which can be acquired by calibration. This needs to be confirmed by experiment. The experimental results with the distributions similar to those shown in Figure 5.2 (b) and Figure 5.5 are shown in Figure 5.6 (b). Note that the high permittivity material is changed to be table salt ($\varepsilon_r = 3.0$) in the experiment for more stable measurements since the ECT system has a limited accuracy for capacitance measurement.

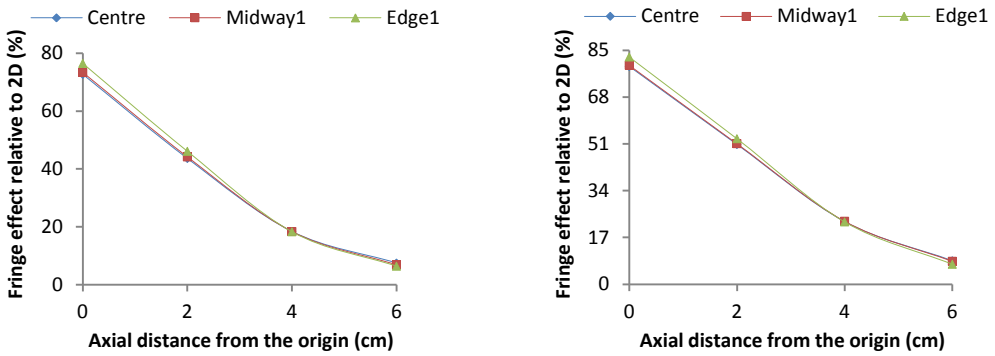

(a) Simulated (b) Measured

Figure 5.6 Change pattern of fringe effect with the axial position of the metallic rod at different cross-sectional positions

The experimental results in Figure 5.6 (b) are consistent with the findings discovered in the simulation, i.e. the proportion of the fringe effect change within each interval of axial distance to the total change, keeps constant. The difference between the simulation and experimental results may be because of the use of different high permittivity material and a longer aluminium rod as well as the inferences from the surroundings in the experiment, which cannot be modelled exactly in the simulation.

5.2.5 Circle centre location method

Once the normalised capacitance is acquired by the experimental ECT system, the corresponding object distribution can be reconstructed in 2D with the sensitivity maps for the 2D sensor model and a conventional reconstruction algorithm, e.g. LBP and

Landweber iteration as described in Chapter 2. As discussed previously, the cross-sectional centre of the reconstructed rod needs to be located to reconstruct the 3D image of the distribution. In the field of precise measurement with Gaussian laser spot, there are four popular centre location algorithms (Tang 2009): grey barycentre method, elliptical fitting, Gaussian distribution and cumulative Gaussian distribution fitting. Grey barycentre method is the simplest, but has the worst accuracy. Elliptical fitting is simple and the most efficient but with high location accuracy. Gaussian and cumulative Gaussian distribution fittings provide the highest location accuracy but are the most complicated and suitable for the precise centre location of very small laser spot. For the application in the centre location of the reconstructed 2D image of the metallic rod, the elliptical fitting is chosen for efficiency and sufficient accuracy. It needs three steps to locate the image centre: (1) Image binarization by thresholding; (2) Image de-noising or elimination of small harmful artefacts with circular shape; (3) Ellipse fitting and calculation of the centre coordinates. These steps are easy to be implemented in MATLAB with ready-made functions for image processing.

Up to now, 3D imaging of the metallic rod can be implemented in 3 steps:

(1) A 2D image of the metallic rod is first reconstructed with a frame of normalised capacitance from a single-plane ECT sensor, and the cross-sectional centre of the reconstructed image is located by applying the elliptical fitting algorithm;
(2) The axial distance of the rod head from the axial origin is derived by calculating the fringe effect contained in the normalised capacitance using Equation (5.2) and solving the interpolation polynomial, which describes the change pattern of the fringe effect at the located cross-sectional centre;
(3) The 3D image of the rod inside the sensor is reconstructed by fusing the results from step (1) and (2) and the prior knowledge about the object's shape and size.

Note that the change pattern of the fringe effect with the axial distance of the rod head from the axial origin is obtained by calibration before the 3D imaging process.

5.3 Experimental results and discussion

To verify the fringe-effect-based 3D reconstruction technique, a set of experimental setups has been established and tested using the impedance-analyser-based ECT system

(Hu *et al*. 2008). The background material, i.e. high permittivity material for calibration, has been selected to validate the feasibility of the proposed method in a large range of permittivity and characterise the 3D imaging in different situations. Table salt ($\varepsilon_r = 3.0$) and deionised water ($\varepsilon_r = 80$) are chosen to achieve this purpose. The background material with lower permittivity, e.g. air or packed plastic beads, would make the measurement less accurate because the resultant coupling capacitance is too small and the experimental system has a limited accuracy for capacitance measurement. Note that the low permittivity material for the calibration of the ECT system is still air.

5.3.1 Experimental setup

In the experiment, the metallic rod is placed at three different cross-sectional positions as shown in Figure 5.2 (b) and Figure 5.7 (a) and (b), which are denoted as centre, midway and edge respectively. The capacitance measurement with the rod in the centre is for calibration, while the ones with the rod at other two positions are for test.

(a) Midway (b) Edge

Figure 5.7 2D views of two object distributions tested in experiment for 3D imaging

In the experiment, the metallic rod is attached to the beam head of a x-y-z stand, the 3D position of which can be adjusted using three verniers with an accuracy of 0.1 mm for each coordinate, i.e. the x and y coordinates determine the cross-sectional position and z coordinate determines the axial position. At first, the height of the beam head is adjusted to make the rod head in the same axial level as the top end of the electrodes in the ECT sensor, which is the origin of the z coordinate. Then by moving the beam head horizontally, the rod centre is positioned in the centre of the ECT sensor, which is the origin of the x and y coordinates. The x and y coordinates of the beam head are then adjusted to place the rod in the desired cross-sectional positions as shown in Figure 5.2 (b) and Figure 5.7. Finally, the z coordinate of the beam head is varied for calibration and measurement. According to the definition of the above coordinate system, the x and

y coordinates of the cross-sectional centres of the rod in Figure 5.2 (b) and Figure 5.7 are (0,0), (1,1) and (2,2), respectively, with cm as the unit, which are the reference coordinates for the subsequent centre location. Note that the z coordinates 0, 2, 4 and 6 cm were implemented in the experiment for calibrating the change pattern of the fringe effect with the axial distance of the rod head from the origin in most cases when the rod was placed in the centre of the sensor's cross-section as shown in Figure 5.2 (b).

5.3.2 3D imaging of metallic rod with table salt as background material

Centre location of reconstructed rod in 2D

With table salt as the background material, the normalised capacitance with the two distributions in Figure 5.7 was acquired by the experimental ECT system when the rod was placed at different axial positions, which is shown in Figure 5.8. It shows that the normalised capacitance decreases with the increase in the axial distance of the rod head from the origin. Note that the legends "0cm", "2cm", "4cm" and "6cm" indicate the axial distance of the rod head from the axial origin.

With the use of the normalised capacitance acquired above, the corresponding 2D images of the rod at different cross-sectional and axial positions are reconstructed using LBP and the sensitivity maps for the 2D sensor model, which are shown in Figure 5.9. Note that the blue colour represents the grounded metallic rod while the red one represents the background material, i.e. table salt in this sub-section.

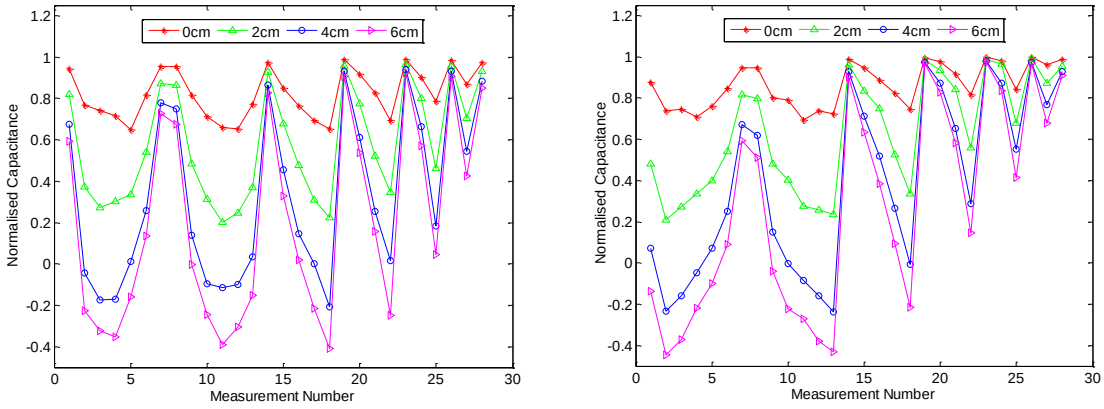

(a) Midway (b) Edge

Figure 5.8 Normalised capacitance with rod at different cross-sectional and axial positions with table salt as the background material

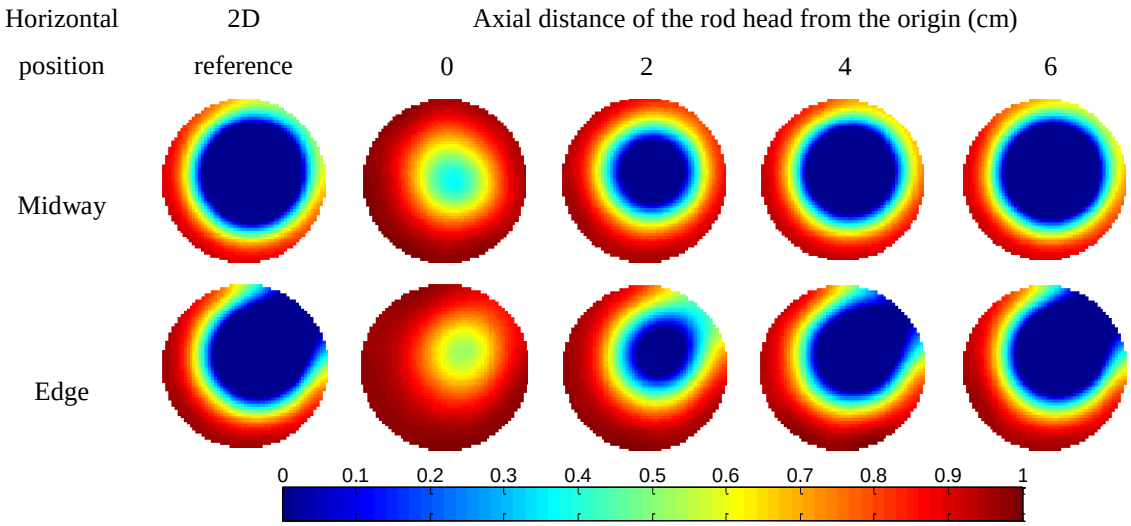

Figure 5.9 Reconstructed images of metallic rod at different cross-sectional and axial positions

Figure 5.9 shows that the reconstructed rod would become larger in the cross-sectional area and more and more similar to its 2D reference when the rod head approaches the bottom end of the electrodes, referred to as the end point for measurement in the following sections. This is consistent with the change pattern of the fringe effect with the axial distance of the rod head from the origin. The centre location algorithm mentioned previously was applied to those 2D images. The results are shown in Figure 5.10. Note that the green ellipse in each image represents the data fitting ellipse. The located cross-sectional centres of those reconstructed images are shown in Table 5.1.

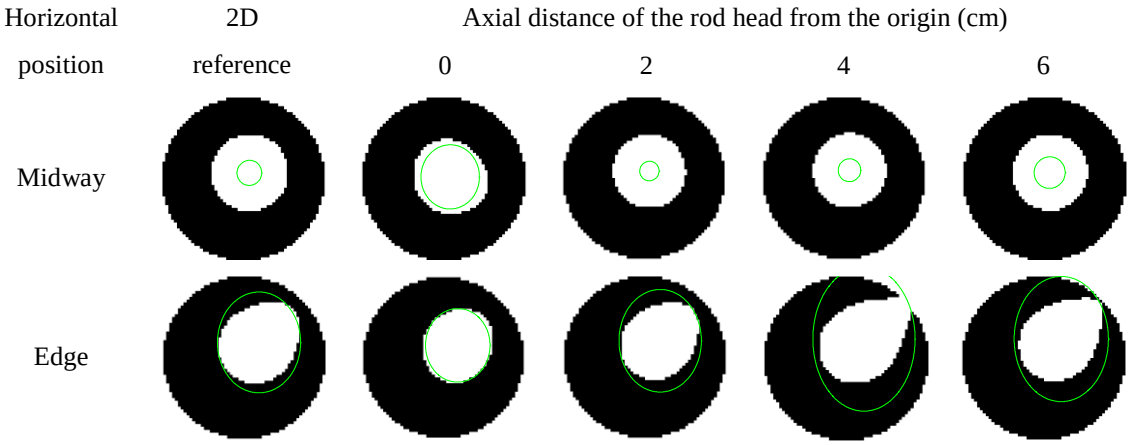

Figure 5.10 Centre location results for reconstructed 2D images of metallic rod at different cross-sectional and axial positions

Table 5.1 Located cross-sectional centres of reconstructed 2D images of metallic rod at different cross-sectional and axial positions with LBP

Horizontal position	Coordinates	2D	Axial distance of the rod head from the origin (cm)						
			0	0.93	2	2.43	4	5.43	6
Midway	x	0.48	0.46	0.43	0.43	0.44	0.45	0.43	0.42
	y	0.47	0.35	0.41	0.52	0.49	0.57	0.52	0.49
Edge	x	1.05	1.01	1.02	1.06	1.12	1.21	1.19	1.17
	y	1.05	0.86	1.02	1.13	1.18	1.29	1.26	1.29

Table 5.1 shows that the centre location error of the reconstructed rod at each specified axial position with LBP is rather large, because the reconstructed images with LBP are merely qualitative, as shown in Figure 5.9. A better location accuracy can be obtained when the rod is approaching the end point for measurement, e.g. 4 and 6 cm away from the axial origin, since a much larger response of capacitance change can be acquired in these cases, i.e. the SNR is relatively high. To improve the centre location accuracy, Landweber iteration was adopted to reconstruct the 2D images of the rod at different positions. The located cross-sectional centre of the reconstructed rod at different cross-sectional and axial positions with Landweber iteration is shown in Table 5.2. Note that the iteration number is 15 and the relaxation factor is updated in each step according to the method proposed by Liu *et al*. (1999) during the iteration.

Table 5.2 Located cross-sectional centre of reconstructed rod at different cross-sectional and axial positions with Landweber iteration

Horizontal position	Coordinates	2D	Axial distance of the rod head from the origin (cm)						
			0	0.93	2	2.43	4	5.43	6
Midway	x	0.75	0.51	0.65	0.66	0.69	0.69	0.67	0.67
	y	0.74	0.47	0.5	0.79	0.74	0.92	0.80	0.79
Edge	x	1.44	1.41	1.43	1.35	1.49	1.34	1.44	1.4
	y	1.44	1.28	1.49	1.51	1.63	1.43	1.57	1.66

Apparently, the centre location accuracy is enhanced greatly using the Landweber iteration, especially when the rod head is close to the axial origin, e.g. 0 and 2 cm away from the origin. By referring to the inner diameter of the ECT sensor wall, i.e. 10.2 cm, the maximum relative error for the centre location is around 7% for each coordinate after 15 iterations. With the located cross-sectional centre and known size of the rod, a

more accurate 2D image can be obtained. The reconstructed 2D images before and after using the prior knowledge are shown in Figure 5.11 with the rod at different cross-sectional and axial positions.

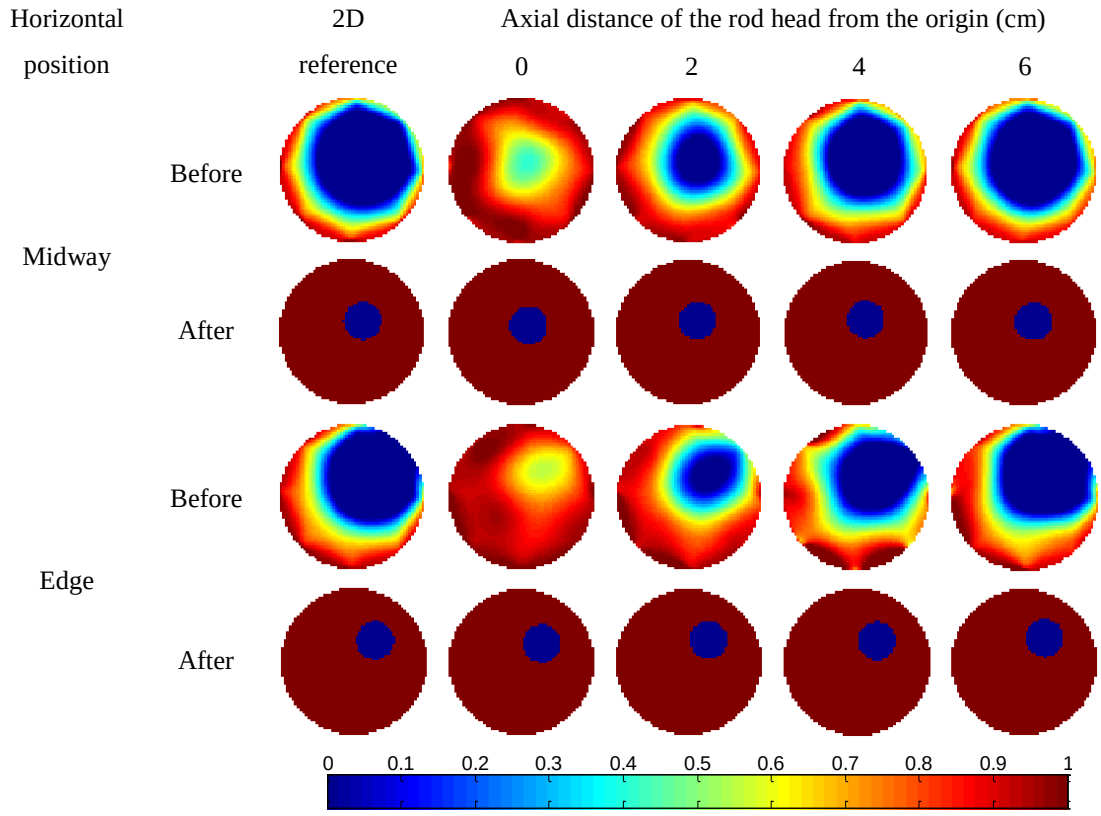

Figure 5.11 Reconstructed 2D images of rod inside table salt before and after using prior knowledge and proposed method

Figure 5.11 shows that much better images can be reconstructed after using the prior knowledge. Once the axial position of the rod is derived, 3D imaging of the metallic rod with a single-plane ECT sensor would be completely feasible.

Derivation of axial distance of rod head from origin

In the first experiment, the axial distances of the rod head from the origin were set to be 0, 0.93, 2, 2.43, 4, 5.43 and 6 cm for both of the distributions shown in Figure 5.7. As mentioned previously, the fringe effect with the rod head at the axial origin in each distribution was used to calibrate the interpolation polynomial for the derivation of the axial position of the rod. Using the previously proposed method, the axial distance of

the rod head from the origin can be estimated for each specified cross-sectional position of the rod and shown in Table 5.3.

Table 5.3 Derived axial distance of rod head from origin for each specified cross-sectional position of rod

Horizontal position	Axial distance of rod head from origin (cm)					
	0.93	2	2.43	4	5.43	6
Midway	0.95	2	2.42	3.99	5.31	6.14
Edge	0.94	2	2.46	4.07	5.41	6.27

Table 5.3 shows that the derivation accuracy of the axial distance of the rod head from the origin with the rod at the midway is higher than that with the rod at the edge, because the fringe effect at the end point with the rod in the edge is much less than that with the rod in the centre, which is used in the derivation and only slightly larger than that with the rod at the midway. It shows that the derivation accuracy with both the distributions deteriorates with the increase in the axial distance of the rod head from the origin, which is about 0.27 cm at the end point, because the fringe effect decreases more and more slowly when the rod head is approaching the end point, i.e. a relatively small change in the fringe effect (caused by the calibration and measurement errors) would derive a relatively large change in the estimated axial distance. This may be improved by calibrating the fringe effect with both the distributions when the rod head is at the end point. With the rod at the edge, the fringe effect at the end point is less than that with the rod in the centre by around 1% in both the simulation and experiment. If this small difference is calibrated, the derived axial position of the rod head at the end point is about 6 cm away from the origin, improving the accuracy. After the calibration, the derived axial distance of the rod head from the origin with the rod at the midway or edge is shown in Table 5.4. By referring to the axial measurement range of 6 cm, however, the maximum relative derivation error is less than 5% before the calibration.

Table 5.4 Derived axial distance of rod head from origin with rod at midway and edge after calibration

Horizontal position	Axial distance rod head from origin (cm)					
	0.93	2	2.43	4	5.43	6
Midway	0.95	1.99	2.41	3.98	5.28	6
Edge	0.93	1.98	2.44	4.02	5.29	6

Table 5.4 shows that after the calibration, the estimation accuracy for the axial distance of 5.43 cm is relatively large (0.15 cm for the maximum). This may be induced by the measurement error or data interpolation error. In a more detailed test, a fourth-order polynomial interpolation was attempted. It was calibrated by the measured fringe effect with the rod in the centre and with axial distances of 0, 2, 4, 5, 6 cm from the origin. The results from the fourth-order interpolation with the rod at the edge are indentified by the row No. 3 in Table 5.5. The rows No.1 and 2 are from the third-order interpolation before and after calibrating the fringe effect at the end point. It shows that the fourth-order interpolation does not improve the estimation result as expected, which become even worse at some test points. To examine the influence of piecewise interpolation on the estimation accuracy, a third-order piecewise interpolation was also attempted but still no significant improvement could be achieved. Based on this finding and the comparison shown in Table 5.5, it is concluded that the estimation error at the axial distance of 5.43 cm in the previous test as shown in Table 5.4 may be because of the measurement error since it is reduced in the new test while the derivation errors at some other test points become slightly worse.

Table 5.5 Derived axial distance of rod head from origin with rod at the edge before and after using fourth-order polynomial interpolation

Horizontal position	No.	Axial distance of rod head from origin (cm)											
		0.43	1	1.43	2	2.43	3	3.43	4	4.43	5	5.43	6
Edge	1	0.42	0.95	1.43	1.99	2.44	3.07	3.46	4.03	4.41	4.99	5.39	6.2
	2	0.42	0.95	1.43	1.98	2.43	3.05	3.44	4	4.38	4.95	5.33	6
	3	0.5	1.03	1.47	1.98	2.4	3	3.39	4	4.44	5.05	5.53	6

5.3.3 3D imaging of metallic rod with deionised water as background

In the previous section, the feasibility of the 3D imaging of a metallic rod with a single-plane ECT sensor is testified when table salt acts as the high permittivity background material. One may wonder whether it is possible for a background material with very high permittivity, such as deionised water, and what is the characteristics in this situation. In another test, deionised water was used as the high permittivity material and the two object distributions as shown in Figure 5.7 were established. The normalised capacitance for these two distributions with the rod at different axial position is shown

in Figure 5.12. The legends “0cm”, “2cm”, “4cm” and “6cm” indicate the axial distance of the rod head from the origin.

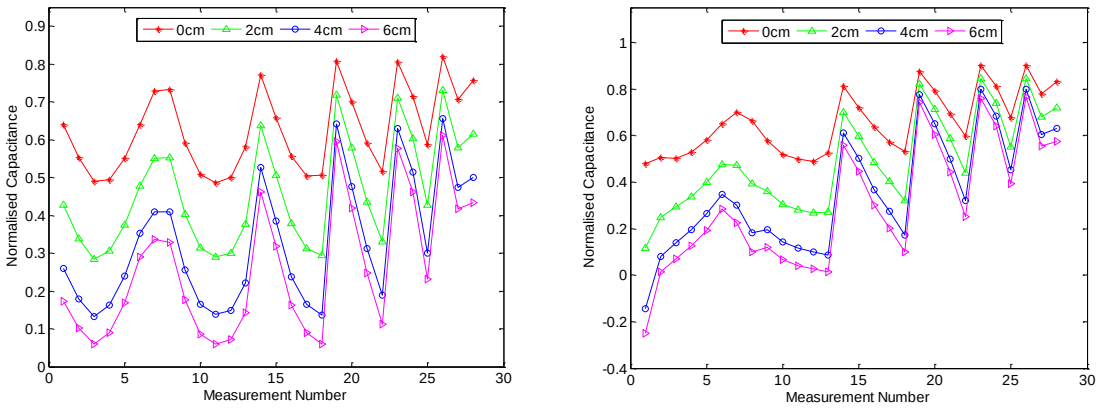

(a) Midway (b) Edge

Figure 5.12 Normalised capacitance for metallic rod at different cross-sectional and axial positions with deioised water as background

Figure 5.12 shows that the normalised capacitance changes similarly with the axial distance of the rod head from the origin as discovered previously. However, the difference between the normalised capacitance for the adjacent or nearly adjacent electrode pairs (e.g. those indentified by measurement number 1 and 2 in Figure 5.12) and the reference value of 1.0 (when the sensor is filled with high permittivity material) is much larger than that with table salt. The maximum difference of the normalised capacitance between different electrode pair from 1.0 is much smaller than that with table salt. This may be induced by the highly non-linear behaviour of capacitance measurement with background material of very high permittivity. Together with the sensitivity maps from the 2D sensor model, 2D images of the metallic rod can be reconstructed. The located cross-sectional centre of the reconstructed rod at different axial position with LBP is shown in Table 5.6, which shows better location accuracy than the corresponding result with LBP for table salt in the previous section. This may be because the SNR of the capacitance measurement with deionised water as background material is much higher than that with table salt. The averaged capacitance change after normalisation of a whole measurement frame with the former is smaller than that with the latter when the metallic rod presents at a specified 3D position inside the sensor. This results in the reconstructed rod with the former being smaller in cross-

sectional area than that with the latter which may help to enhance the location accuracy. Similarly, Landweber iteration was attempted to improve the centre location accuracy for the reconstructed rod at different axial position. The results are shown in Table 5.7. The location accuracy of the x coordinate of the reconstructed rod centre slightly deteriorates after 15 iterations when the rod head is close to the axial origin or stays almost the same otherwise, while for y coordinate it is improved significantly, especially when the rod head is close to the end point. This may be because the maximum difference between the normalised capacitance for different electrode pairs is much smaller with background material of high permittivity (deionised water) than that with background material of low permittivity due to the presence of the rod inside the sensor (the former is almost half of the latter), which becomes even smaller when the rod head is close to axial origin. As the Landweber iteration is a linear reconstruction method, the grey level contrast of the reconstructed image would be small with the small contrast of normalised capacitance for different electrode pairs and easily be affected by iteration errors due to the highly nonlinear behaviour of the capacitance measurement with high permittivity material. This would finally influence the centre location accuracy with Landweber iteration.

Table 5.6 Located cross-sectional centre of reconstructed rod in 2D at different axial position with LBP

Horizontal position	Coordinates	2D	Axial distance of rod head from origin (cm)						
			0	1	2	2.43	4	5.43	6
Midway	x	0.59	0.43	0.49	0.53	0.56	0.6	0.6	0.61
	y	0.59	0.55	0.64	0.72	0.74	0.83	0.84	0.86
Edge	x	1.47	1.38	1.43	1.45	1.49	1.45	1.44	1.43
	y	1.47	1.49	1.6	1.64	1.66	1.68	1.65	1.66

Table 5.7 Located cross-sectional centre of reconstructed rod in 2D at different axial position with Landweber iteration

Horizontal position	Coordinates	2D	Axial distance of rod head from origin (cm)						
			0	1	2	2.43	4	5.43	6
Midway	x	0.83	0.36	0.39	0.43	0.44	0.51	0.49	0.59
	y	0.83	0.64	0.71	0.77	0.8	0.91	0.92	1
Edge	x	1.43	1.23	1.26	1.35	1.36	1.4	1.41	1.39
	y	1.42	1.51	1.6	1.71	1.73	1.83	1.82	1.82

Using the previously proposed method, more accurate 2D images can be reconstructed with the located centre of the reconstructed rod in 2D and the prior knowledge about the rod size, which are shown in Figure 5.13. Note that the 2D images before using the prior knowledge with the rod at the axial distances of 0 and 2 cm are reconstructed by LBP, while others are reconstructed by Landweber iteration (15 iterations and the relaxation factor is updated in each step as discussed previously), because the centre location accuracy with LBP for the rod at the axial distances of 0 and 2 cm is better than that with Landweber iteration. Using the method proposed previously, the axial distance of the rod head from the origin can be derived after calibrating the fringe effect at the end point with rod at the midway and edge of the cross-section of the sensor, which is shown in Table 5.8. It shows that less than 3% relative estimation error (referred to the measurement range of 6 cm) can be obtained in this situation. The above results confirm that 3D imaging of the metallic object with the single-plane ECT sensor is fully feasible for relatively low and high permittivity background materials (i.e. table salt and deionised water).

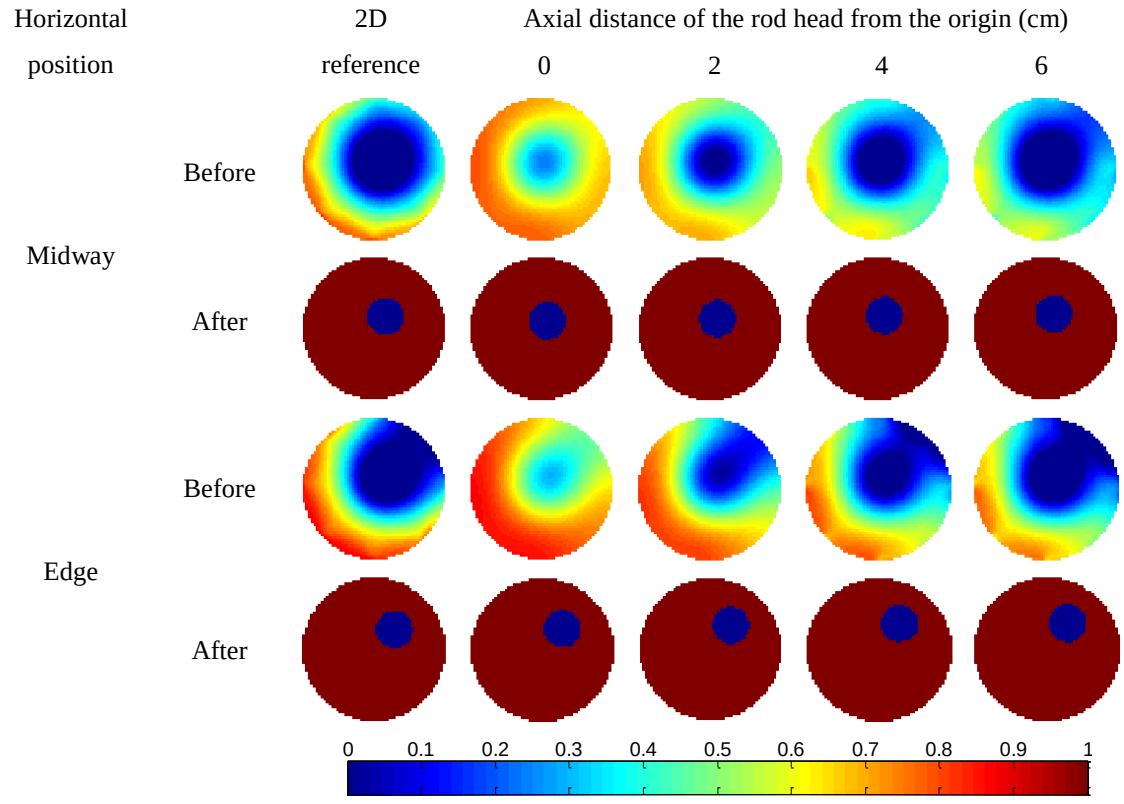

Figure 5.13 Reconstructed 2D images of rod inside deionised water before and after using prior knowledge and proposed method

Table 5.8 Derived axial distance of rod head from origin with rod at midway and edge of cross-section after calibrating fringe effect at end point

Horizontal position	Axial distance of rod head from origin (cm)											
	0.43	1	1.43	2	2.43	3	3.43	4	4.43	5	5.43	6
Midway	0.42	0.98	1.43	2	2.46	3.02	3.47	4	4.42	4.94	5.37	6
Edge	0.44	1.01	1.48	2.07	2.52	3.1	3.55	4.08	4.49	5.02	5.44	6

With the derived axial distance of the rod head from the axial origin, the 3D image of the metallic rod can be reconstructed by extruding the reconstructed 2D image upwards along the axial direction accordingly, which is subject to the experiment setup and the defined 3D volume for illustration.

5.3.4 Estimation of 2D reference and calibration of fringe effect at end point

From the simulation and experiment, it was found that the averaged capacitance after the normalisation of a whole measurement frame only depends on the distance of the rod centre from the cross-sectional centre of the sensor at a fixed axial position, because the ECT sensor has 8 circular symmetric electrodes with a small gap between adjacent electrodes, which is approximately rotation invariant. This means that each time the cross-sectional centre of the reconstructed rod in 2D is located first, and then the distance between the located centre and the sensor centre can be calculated. This calculated distance can be used to derive the 2D reference required in equation (5.2) for the examination of the fringe effect by solving an interpolation polynomial, which is established prior to the reconstruction to describe the change pattern of the 2D reference with the cross-sectional distance of the rod centre from the sensor centre, as shown in Figure 5.14 (a). For the calibration of the fringe effect at the end point, the same method can be adopted since an interpolation polynomial can also be obtained from the 3D simulation, which describes the change pattern of the fringe effect variation at the end point (by referred to that with the rod in the centre of the sensor) with the cross-sectional distance of the rod centre from the sensor centre, as shown in Figure 5.14 (b).

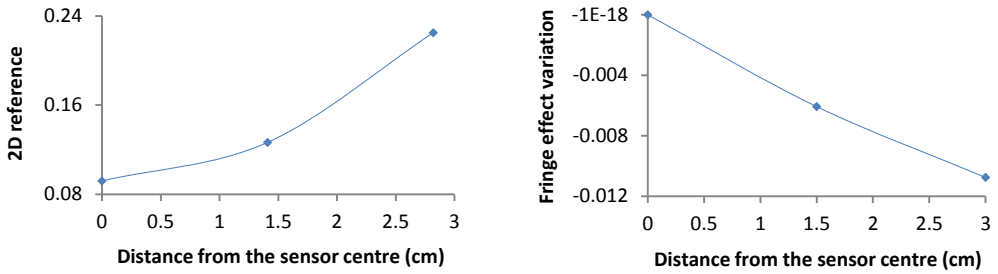

(a) 2D reference (b) Fringe effect variation at end point

Figure 5.14 2D reference and fringe effect variation at end point with rod at different cross-sectional positions and table salt as background material

5.4 Summary

This chapter is dedicated to the fringe-effect-based 3D imaging of an metallic rod with a single-plane ECT sensor. The objective was to explore the model-based 3D imaging principle utilising the fringe effect contained in ET measurement and the prior knowledge about the shape and size of the object to be imaged. In the beginning, the imaging principle for metallic objects with ECT is illustrated. With the capacitance measurement from a single-plane ECT sensor, 2D images of the metallic rod can be reconstructed, the centre of which can be located by certain algorithm. In the meantime, the fringe effect contained in the measured capacitance after normalisation can be examined to estimate the axial position of the object. At last, 3D images of the rod can be reconstructed by fusing the derived 3D position of the rod and the prior knowledge about its shape and size. Based on the proposed method, experiment was conducted to locate the centre of the reconstructed rod in 2D and estimate its axial position while table salt and deionised water were used as the high permittivity background material respectively. The results show that the 3D position of the rod can be calculated accurately in both cases. It is suggested that the proposed method can be applied to 3D imaging of a dielectric object with a single-plane ECT sensor or 3D imaging with a single-plane ERT or EMT sensor when the shape and size of the object are prior knowledge and a similar process is involved, e.g. the removal of the bone cement with a milling tool during total hip revision.

Chapter 6: Conclusions and future work

This chapter will present conclusions drawn from the simulation and experimental results obtained in the previous chapters. Based on the conclusions, some suggestions will be made for future work.

6.1 Conclusions

Fringe effect occurs in the conventional 2D imaging with ET sensors. It is associated with the sensor structure and object distribution as well as the measurement strategy, which was investigated systematically in this research. In view of the relevant findings, fringe effect can be reduced by the appropriate design of sensor structure or the use of some compensation method. To turn the disadvantage into advantage, fringe effect is applied in the 3D imaging of certain processes with a single-plane ECT sensor.

With voltage-excitation strategy and axially uniform distributions, either symmetric or non-symmetric, ECT and ERT sensors have similar fringe effect for a particular electrode length with or without grounded end guards regarding the normalised measurement or reconstructed 2D image by LBP. The simulation result from the corresponding 2D sensor model was used as the reference in the evaluation of the fringe effect for different structures of ECT/ERT sensors. It was revealed that the fringe effect would decrease with the increase in the electrode length and the use of grounded end guards would narrow the axial sensing range of the sensor. The feasibility of ERT with voltage-excitation was verified by experiment, which enables the use of grounded end guards in ERT sensors to reduce their fringe effect. This makes it possible to integrate ECT/ERT sensors into one for ECT/ERT dual-modality measurement to simplify the sensor structure and reduce the inference between each other. There are two drawbacks, however, for the use of long electrodes and grounded end guards: (1) Long electrodes can lower the axial sensing resolution of ECT/ERT sensors. Therefore, a trade-off needs to be made between the fringe effect and axial sensing resolution in some applications; (2) Grounded end guards have a negative effect on the capacitance or conductance measurement since electric field lines are drawn to the grounded guards as described by Yang (2010) and may not be applicable when the background medium is highly conductive.

For ERT with adjacent current-injection and voltage-measurement strategy, much less fringe effect would occur with axially uniform distribution, compared with ECT/ERT with voltage-excitation, because the equivalent electrical models are different in these two cases. To investigate the influences of the non-uniformity of the axial distribution on the fringe effect, simulation was conducted for objects with different axial length and conductivity contrast to the background medium, and at different axial position. For conductive or non-conductive objects inside the sensor plane, it was concluded that the fringe effect would decrease with the increase in the object length. More conductive the object is compared with the background, less fringe effect there would be, if the axial length and position of the object are specified. For non-conductive objects outside the sensor plane, it was concluded that the fringe effect would increase with the increase in the object length for a particular axial position, and decrease with axial distance of the object from the sensor plane for a particular axial length. To reduce the fringe effect, a compensation method was suggested, i.e. selective scaling, which was proven to be effective by simulation and experiment, especially for the distribution with two objects at different axial positions. Based on the compensation method, a three-plane ERT sensor scheme was proposed to reduce the fringe effect induced by objects outside the sensor plane and the over-estimation of object size by Landweber iteration, which was also validated by simulation and experiment. The drawback is that overestimation of object size by Landweber iteration may not occur all the time, especially when the distribution is severely axially non-uniform, e.g. the object to be imaged is much shorter than the tube. For the verification, an experimental ERT system was established with Howland circuits, differential amplification circuits and a commercialised data acquisition unit (Agilent 34972A).

Simulation showed that fringe effect is related to the axial position and length of an object with a regular shape within the axial sensing range of an ET sensor. This implies that it can be applied to 3D imaging with a single-plane ET sensor. Instead of visualising dielectric materials, a single-plane ECT sensor was used to do 3D imaging of a metallic object, the principle of which was introduced by simulation. During the 3D imaging process, a 2D image of the object is reconstructed first, the cross-sectional centre of which can be located with certain algorithms. By examining the fringe effect, the axial position of the object head can be derived with the calibration curve obtained by data interpolation before the 3D imaging, which describes the change pattern of the

fringe effect with the axial position of the object head. With the 3D position of the object head, the 3D image of the object inside the sensor can be reconstructed by incorporating the prior knowledge about its shape and dimensions. Table salt and deionised water were used as the background material for 3D imaging of a metallic rod in the experiment, where different reconstruction algorithms and derivation methods were attempted. Experimental results showed that the proposed 3D imaging method is feasible. For the practical use, some calibration issues were also addressed.

6.2 Future work

In view of the conclusions drawn from this research, future work is suggested in the following aspects.

ERT with voltage-excitation needs to be further verified by experiment regarding minimising the effect of contact impendence in different applications and used with grounded end guards to reduce the fringe effect and improve the measurement accuracy. Relevant electronics need to be developed for ECT/ERT dual-modality measurement with a common sensor as proposed in Chapter 3. The dual-modality measurement accuracy for the conductive and non-conductive phases in a multiphase flow will be evaluated by experiment. In certain cases where the measurement requires the electrode length to be much shorter than the sensor dimension, the electrode combination strategy as mentioned in Chapter 2 may be tested for its effectiveness in reducing the fringe effect of ECT and ERT sensors with voltage-excitation.

The compensation method for fringe effect and three-plane ERT sensor scheme in Chapter 4 may be combined together to reduce the fringe effect due to the axially non-uniform distribution, either induced by objects outside the sensor plane or not. More complicated distributions with multiple objects and different conductivity contrast, may be tested with this combined technique to verify the feasibility. The geometry parameters of the three-plane ERT sensor may be optimised according to the typical flow pattern in a particular application.

To develop a real-time visualisation tool for total hip revision with ECT, a conical ECT sensor has been designed and made, as shown in Figure 6.1, for a test with a pig shank. The marrows inside the main bone of the pig shank were removed before the test. It was

found that the images of the metal rod inside the bone of the pig shank are not as accurate as inside table salt or deionised water in Chapter 5. This may be because the relative permittivity of the human tissues, especially the muscles, is too high (several hundred for muscles) at low frequencies below 5 MHz and the water inside the tissues is conductive. Because most tissues of human beings are more or less conductive and the bone cement is almost non-conductive (Brendle *et al*. 2012a, Brendle *et al*. 2012b).

Figure 6.1 Conical ECT sensor

Due to the ineffectiveness of ECT sensor, the fringe-effect-based 3D imaging technique may be applied with a single-plane ERT or EMT sensor to visualise the milling process in total hip revision. Improved calibration methods without milling the bone cement need to be devised to acquire the change pattern of the fringe effect with the axial position of the milling bit before the imaging process. Other techniques may be attempted to estimate the 3D position of the milling bit, e.g. input an AC voltage signal into a milling tool and measure the response signal on each electrode (grounded for detection) of an ECT sensor in sequence to determine the respective mutual capacitance, which may be used for positioning. Another challenge is when the moving path of the milling bit is not vertical but tilt, where a multi-plane ET sensor may be applied.

References

[1] Agilent Technologies (2010), Agilent 34970A/34972A data acquisition/switch unit user's guide, *2nd Edition*, Printed in Malaysia

[2] Alme K J and Mylvaganam S (2006a), Analyzing 3D and Conductivity Effects in Electrical Tomography Systems Using COMSOL Multiphysics EM Module, Excerpt from the *Proc. 2006 Nordic COMSOL Conference*, 1–2 November, Copenhagen, Denmark

[3] Alme K J and Mylvaganam S (2006b), Electrical capacitance tomography – sensor models, design, simulations, and experimental verification, *IEEE Sensors J.*, 6, pp 1256–1266

[4] Alme K J and Mylvaganam S (2007), Comparison of different measurement protocols in electrical capacitance tomography using simulations, *IEEE Trans. on Inst. and Meas.*, 56, pp 2119–2130

[5] Banasiak R and Soleimani M (2010), Shape based reconstruction of experimental data in 3D electrical capacitance tomography, *NDT&E International*, 43, pp 241–249

[6] Banasiak R, Wajman R, Sankowski D and Soleimani M (2010), Three-dimensional nonlinear inversion of electrical capacitance tomography data using a complete sensor model, *Prog. Electromagn. Res.*, 100, pp 219–234

[7] Banasiak R, Ye Z and Soleimani M (2012), Improving three-dimensional electrical capacitance tomography imaging using approximation error model theory, *J. Electromagn. Waves Appl.*, 26 (2-3), pp 411–421

[8] Barber C C, Brown B H and Freeston I L (1983), Imaging spatial distributions of resistivity using applied potential tomography, *Electron. Lett.*, 19 (22), pp 933–935

[9] Barber D C and Brown B H (1984), Applied potential tomography, *J. Phys. E*, 17 (9), pp 723–733

[10] Boone K G and Holder D S (1996), Current approaches to analogue instrumentation design in electrical impedance tomography, *Physiol. Meas.*, 17 (suppl 1A), pp A229–A247

[11] Boyle A and Adler A (2011), The impact of electrode area, contact impedance and boundary shape on EIT images, *Physiol. Meas.*, 32, pp 745–754

[12] Brendle C, Niesche A, Korff A, Radermacher K and Leonhardt S (2012a), Femoral Test Bed for Impedance Controlled Surgical Instrumentation, *Acta Polytechnica*, 52, pp 17–21

[13] Brendle C, Leonhardt S, Niesche A, Korff A and Radermacher K (2012b), Influence of a Sliding Contact on Impedance Monitoring in a Smart Surgical Milling Tool, *Proc. Int. Workshop on Impedance Spectroscopy*, 26–28 September, Chemnitz, Germany

[14] Cao Z and Xu L J (2011), Direct image reconstruction for electrical capacitance tomography by using the enclosure method, *Meas. Sci. Technol.*, 22, pp 104001

[15] Cao Z and Xu L J (2013), Direct image reconstruction for 3-D electrical resistance tomography by using the factorization method and electrodes on a single plane, *IEEE Trans. on Inst. and Meas.*, 62, pp 999–1007

[16] Cao Z, Xu L J, Fan W R and Wang H X (2010), Electrical capacitance tomography with a non-circular sensor using the dbar method, *Meas. Sci. Technol.*, 21, pp 015502

[17] Cao Z, Xu L J, Fan W R and Wang H X (2011a), Electrical capacitance tomography for sensors of square cross sections using Calderon's method, *IEEE Trans. Instrum. Meas.*, 60, pp 900–907

[18] Cao Z, Xu L J, Fan W R and Wang H X (2011b), 2D electrical capacitance tomography with sensors of non-circular cross sections using the factorization method, *Meas. Sci. Technol.*, 22, pp 114003

[19] Cao Z, Xu L J and Wang H X (2009), Image reconstruction technique of electrical capacitance tomography for low-contrast dielectrics using Calderon's method, *Meas. Sci. Technol.*, 20, pp 104027

[20] Cardu R, Leong P H W, Jin C T and McEwan A (2012), Electrode contact impedance sensitivity to variations in geometry, *Physiol. Meas.*, 33, pp 817-830

[21] Chaplin G, Pugsley T, Lee L vd, Kantzas A and Winters C (2005), The dynamic calibration of an electrical capacitance tomography sensor applied to the fluidized bed drying of pharmaceutical granule, *Meas. Sci. Technol.*, 16 (6), pp 1281–1290

[22] Cilliers J J, Xie W, Neethlings S J, Randall E W and Wilkinson A J (2001), Electrical resistance tomography using a bi-directional current pulse technique, *Meas. Sci. Technol.*, 12, pp 997–1001

[23] Dehghani H, Soni N, Halter R, Hartov A and Paulsen K D (2005), Excitation patterns in three-dimensional electrical impedance tomography, *Physiol. Meas.*, 26, pp S185–S197

[24] Dickin F and Wang M (1996), Electrical resistance tomography for process applications, *Meas. Sci. Technol.*, 7, pp 247–260

[25] Dyakowski T, Jeanmeure L F C and Jaworski A J (2000), Applications of electrical tomography for gas-solids and liquid-solids flows – a review, *Powder Technol.*, 112, pp 174–192

[26] Fang W (2004), A nonlinear image reconstruction algorithm for electrical capacitance tomography, *Meas. Sci. Technol.*, 15, pp 2124–2132

[27] Fasching G E (1988), 3-D capacitance density imaging system, *U.S. Patent*, Number: A7,170,229

[28] Flores N, Gamio J C, Ortiz-Alemán C and Damián E (2005), Sensor modelling for an electrical capacitance tomography system applied to oil industry, Excerpt from the *Proc. COMSOL Multiphysics User's Conference*, October, Boston, USA

[29] Fransolet E, Crine M, Homme G L, Toye D and Marchot P (2001), Analysis of electrical resistance tomography measurements obtained on a bubble column, *Meas. Sci. Technol.*, 12, pp 1055–1060

[30] Fransolet E, Crine M, Homme G L, Toye D and Marchot P (2002), Electrical resistance tomography sensor simulations: comparison with experiments, *Meas. Sci. Technol.*, 13, pp 1239–1247

[31] Fransolet E, Crine M, Marchot P and Toye D (2005), Analysis of gas holdup in bubble columns with non-Newtonian fluid using electrical resistance tomography and dynamic gas disengagement technique, *Chem. Eng. Sci.*, 60, pp 6118–6123

[32] Giguère R, Fradette L, Mignon D and Tanguy P A (2008), ERT algorithms for quantitative concentration measurement of multiphase flows, *Chem. Eng. J.*, 141, pp 305–317

[33] Hansen P C and Saxild-Hansen M (2012), Air Tools – A MATLAB package of algebraic iterative reconstruction methods, *J. Comput. Appl. Math.*, 236, pp 2167–2178

[34] Hartov A, Demidenko E, Soni N, Markova M and Paulsen K (2002), Using voltage sources as current drivers for electrical impedance tomography, *Meas. Sci. Technol.*, 13, pp 1425–1430

[35] Hayes R, Podd F, Newill P, Grieve B D and York T A (2012), Capacitively-coupled impedance measurements for ERT, *Proc. 6th Int. Symp. on Process Tomography*, 26–28 March, Cape Town, South Africa

[36] HP (1987), HP4192A LF impedance analyser service and operation manual

[37] Hu X H (2009), Imaging of hidden objects by planar capacitive and magnetic sensor arrays for security applications, *PhD thesis*, The University of Manchester, UK

[38] Hu X H, Yang M, Ismail I, Li Y, Yang W Q and de Lara M M (2008), An impedance-analyser-based multi-channel imaging system and its applications, *Proc. IEEE Int. Workshop on Imaging Systems and Techniques*, 10–12 September, Chania, Greece, pp 181–186

[39] Huang S M, Dyakowski T, Xie C G, Plaskowski A B, Xu L A and Beck M S (1988a), A tomographic flow imaging system based on capacitance measuring techniques, *Proc. Int. Conf. Pattern Recognit.*, 14–17 November, Rome, Italy, pp 570–572

[40] Huang S M, Plaskowski A B, Xie C G and Beck M S (1989), Tomographic imaging of two-component flow using capacitance sensors, *J. Phys. E: Sci. Instrum.*, 22, pp 173–177

[41] Huang S M, Stott A L, Green R G and Beck M S (1988b), Electronic transducers for industrial measurement of low value capacitances, *J. Phys. E, Sci. Instrum.*, 21, pp 242–250

[42] Huang S M, Xie C G, Thorn R, Snowden D and Beck M S (1992), Design of sensor electronics for electrical capacitance tomography, *IEE Proc. G*, 139 (l), pp 83–88

[43] Huang Z Y, Jiang W W, Zhou X M, Wang B L, Ji H F and Li H Q (2009), A new method of capacitance coupled contactless conductivity detection based on series resonance, *Sens. Actuators B: Chem.*, 143, pp 239–245

[44] Isaksen O and Nordtvedt J E (1993), A new reconstruction algorithm for process tomography, *Meas. Sci. Technol.*, 4, pp 1464–1475

[45] Jia J B, Wang M, Schlaberg H I and Li H (2010), A novel tomographic sensing system for high electrically conductive multiphase flow measurement, *Flow Meas. Instrum.*, 21, pp 184–190

[46] Jin H, Wang M and Williams R A (2007), Analysis of bubble behaviors in bubble columns using electrical resistance tomography, *Chem. Eng. J.*, 130, pp 179–185

[47] Jossinet J, Tourtel C and Jarry R (1994), Active current electrodes for in-vivo electrical impedance tomography, *Clin. Phys. Physiol. Meas.*, 15 (Suppl. 2A), pp 83–90

[48] Khambampati A K, Lee B A, Kim K Y and Kim S (2012), An analytical boundary element integral approach to track the boundary of a moving cavity using electrical impedance tomography, *Meas. Sci. Technol.*, 23, pp 035401

[49] Kim J H, Choi B Y and Kim K Y (2006), Novel iterative image reconstruction algorithm for electrical capacitance tomography: directional algebraic reconstruction technique, *IEICE Trans. Fundamentals*, E89-A, pp 1578–1584

[50] Kim Y S, Lee S H, Ijaz U Z, Kim K Y and Choi B Y (2007), Sensitivity map generation in electrical capacitance tomography using mixed normalization models, *Meas. Sci. Technol.*, 18, pp 2092–2102

[51] Li Y (2008), Key issues of 2D/3D image reconstruction in electrical tomography, *PhD thesis*, The University of Manchester, UK

[52] Li Y and Holland D J (2013), Fast and robust 3D electrical capacitance tomography, *Meas. Sci. Technol.*, 24, pp 105406

[53] Li Y and Soleimani M (2013), Imaging conductive materials with high frequency electrical capacitance tomography, *Measurement*, 46 (9), pp 3355–3361

[54] Li Y and Yang W Q (2008), Image reconstruction by nonlinear Landweber iteration for complicated distributions, *Meas. Sci. Technol.*, 19, pp 094014

[55] Li Y and Yang W Q (2009), Measurement of multi-phase distribution using an integrated dual-modality sensor, *Proc. IEEE Int. Workshop on Imaging Systems and Techniques*, 11–12 May, Shenzhen, China, pp 335–339

[56] Lidgey F J, Zhu Q S, McLeod C N and Breckon W R (1992), Electrode current determination from programmable voltage sources, *Clin. Phys. Physiol. Meas.*, 13, pp 43–46

[57] Lionheart W R B (2001), Reconstruction algorithms for permittivity and conductivity imaging, *Proc. 2nd World Congress on Industrial Process Tomography*, 29–31 August, Hannover, Germany, pp 4–11

[58] Liu S, Fu L and Yang W Q (1999), Optimization of an iterative image reconstruction algorithm for electrical capacitance tomography, *Meas. Sci. Technol.*, 10 (7), pp L37–L39

[59] Liu S, Yang W Q, Wang H, Jiang F and Su Y (2001), Investigation of square fluidized beds using capacitance tomography: preliminary results, *Meas. Sci. Technol.*, 12, pp 1120–1125

[60] Loser T, Wajman R and Mewes D (2001), Electrical capacitance tomography: image reconstruction along electrical field lines, *Meas. Sci. Technol.*, 12, pp 1083–1091

[61] Ma X, Peyton A J, Higson S R, Lyons A and Dickinson S J (2006), Hardware and software design for an electromagnetic induction tomography (EMT) system for high contrast metal process applications, *Meas. Sci. Technol.*, 17 (1), pp 111–118

[62] Ma Y X, Wang H, Xu L A and Jiang C Z (1997), Simulation study of the electrode array used in an ERT system, *Chem. Eng. Sci.*, 52, pp 2197–2203

[63] Ma Y X, Xu L A and Jiang C Z (1999), Experimental study of the guard electrodes in an ERT system, *Proc. 1th World Congress on Industrial Process Tomography*, 14–17 April, Buxton, UK, pp 335–338

[64] Marashdeh Q, Fan L -S, Du B and Warsito W (2008), Electrical capacitance tomography-a perspective, *Ind. Eng. Chem. Res.*, 47, pp 3708–3719

[65] Marashdeh Q, Warsito W, Fan L -S and Teixeira F L (2006a), Nonlinear forward problem solution for electrical capacitance tomography using feed-forward neural network, *IEEE Sensors J.*, 6, pp 441–449

[66] Marashdeh Q, Warsito W, Fan L -S and Teixeira F L (2006b), Non-linear image reconstruction technique for ECT using a combined neural network approach, *Meas. Sci. Technol.*, 17, pp 2097–2103

[67] Marashdeh Q, Warsito W, Fan L -S and Teixeira F L (2007), A multimodal tomography system based on ECT sensors, *IEEE Sensors J.*, 7, pp 426–433

[68] McAdams E T, Jossinet J, Lackermeier A and Risacher F (1996), Factors affecting electrode gel-skin interface impedance in electrical impedance tomography, *Med. Biol. Eng. Comput.*, 34, pp 397–408

[69] McKeen T R and Pugsley T S (2002), The influence of permittivity models on phantom images from electrical capacitance tomography, *Meas. Sci. Technol.*, 13, pp 1822–1830

[70] Mirkowski J, Smolik W T, Yang M, Olszewski T, Szabatin R, Radomski D S and Yang W Q (2008), A new forward-problem solver based on a capacitor-mesh model for electrical capacitance tomography, *IEEE Trans. Instrum. Meas.*, 57, pp 973–980

[71] Mohamad E J, Rahim R A, Leow Pei L, Rahiman M H F, Faizan Bin Marwah O M and Ayob N M N (2012), Segmented capacitance tomography electrodes: a design and experimental verifications, *IEEE Sensors J.*, 12, pp 1589–1598

[72] Murphy S C, Stanley S J, Rhodes D and York T A (2006), 3D electrical tomographic imaging using vertical arrays of electrodes, *Meas. Sci. Technol.*, 17, pp 3053–3065

[73] Neumayer M, Zangl H, Watzenig D and Fuchs A (2011), Current reconstruction algorithms in electrical capacitance tomography, in *New Developments and Applications in Sensing Technology*, 83, Berlin, Germany: Springer-Verlag, ser. Lecture Notes in Electrical Engineering, pp 65–106

[74] Pan T S and Yagle A E (1992), Acceleration of Landweber-type algorithms by suppression of projection on the maximum singular vector, *IEEE Trans. Med. Imaging*, 11 (4), pp 479–487

[75] Peng L H, Merkus H and Scarlett B (2000), Using regularization methods for image reconstruction of electrical capacitance tomography, *Part. Part. Syst. Charact.*, 17, pp 96–104

[76] Peng L H, Mou C H, Yao D Y, Zhang B F and Xiao D Y (2005), Determination of the optimal axial length of the electrode in an electrical capacitance tomography sensor, *Flow Meas. Instrum.*, 16, pp 169–175

[77] Pinheiro P A T, Loh W W and Dickin F J (1998), Three-dimensional reconstruction algorithm for electrical resistance tomography, *IEE Proc.-Sci. Meas. Technol.*, 145, pp 85–93

[78] Polydorides N and McCann H (2002), Electrode configuration for improved spatial resolution in electrical impedance tomography, *Meas. Sci. Technol.*, 13 (12), pp 1862–1870

[79] Rabbani K S and Kabir A M B H (1991), Studies on the effect of the third dimension on a two-dimensional electrical impedance tomography system, *Clin. Phys. Physiol. Meas.*, 12, pp 393–402

[80] Reinecke N and Mewes D (1996), Recent developments and industrial research applications of capacitance tomography, *Meas. Sci. Technol.*, 7, pp 325–337

[81] Ren S J, Dong F, Xu Y Y and Tan C (2014), Reconstruction of the three-dimensional inclusion shapes using electrical capacitance tomography, *Meas. Sci. Technol.*, 25, pp 025403

[82] Saulnier G J, Ross A S and Liu N (2006), A high-precision voltage source for EIT, *Physiol. Meas.*, 27, pp S221–S236

[83] Shih C Y, Li W, Zheng S Y and Tai Y C (2006), A resonance-induced resolution enhancement method for conductivity sensors, *Proc. 5th IEEE Conf. on Sensors*, EXCO, 22–25 October, Daegu, Korea, pp 271–274

[84] Soleimani M and Lionheart W R B (2005), Nonlinear image reconstruction for electrical capacitance tomography using experimental data, *Meas. Sci. Technol.*, 16, pp 1987–1996

[85] Soleimani M, Mitchell C N, Banasiak R, Wajman R and Adler A (2009), Four-dimensional electrical capacitance tomography imaging using experimental data, *Prog. Electromagn. Res.*, 90, pp 171–186

[86] Soleimani M, Wang H G, Li Y and Yang W Q (2007), A comparative study of 3D electrical capacitance tomography, *Int. J. of Inf. and Sys. Sci.*, 3, pp 292–306

[87] Somersalo E, Cheney M and Isaacson D (1992), Existence and uniqueness for electrode models for electric current computed tomography, *SIAM J. App. Math.*, 52 (4), pp 1023–1040

[88] Su B L, Zhang Y H, Peng L H, Yan D Y and Zhang B F (2000), The use of simultaneous iterative reconstruction technique for electrical capacitance tomography, *Chem. Eng. J.*, 77, pp 37–41

[89] Sun J T and Yang W Q (2011), 3D issues of electrical capacitance and resistance tomography sensors, *Proc. IASTED Int. Conf. on Signal and Image Processing and Applications*, 22–24 June, Crete, Greece

[90] Szczepanik Z and Rucki Z (2007), Field analysis and electrical models of multi-electrode impedance sensors, *Sens. Actuators A: Phys.*, 133, pp 13–22

[91] Tang G Q (2009), Analysis and comparison of several calculation methods of beam spot centre, *J. of Beijing institute of Machinery*, 24, pp 61–64

[92] Tang M, Wang W, Wheeler J, McCormick M and Dong X (2002), The number of electrodes and basis functions in EIT image reconstruction, *Physiol. Meas.*, 23 (1), pp 129–140

[93] Toumazou C and Lidgey F J (1989), Novel current-mode instrumentation amplifier, *Electron. Lett.*, 25, pp 228–230

[94] Toye D, Fransolet E, Simon D, Crine M, L'Homme G and Marchot P (2005), Possibilities and limits of application of electrical resistance tomography in hydrodynamics of bubble columns, *Can. J. Chem. Eng.*, 83, pp 4–10

[95] Trillaud C and Jossinet J (1992), An improved design of voltmeter for semi-parallel data acquisition, *Clin. Phys. Physiol. Meas.*, 13 (Suppl. A), pp 5–10

[96] Vijayan M, Schlaberg H I and Wang M (2007), Effects of Sparger geometry on the mechanism of flow pattern transition in a bubble column, *Chem. Eng. J.*, 130, pp 171–178

[97] Wajman R, Banasiak R, Mazurkiewicz L, Dyakowski T and Sankowski D (2006), Spatial imaging with 3D capacitance measurements, *Meas. Sci. Technol.*, 17 (8), pp 2113–2118

[98] Wajman R, Mazurkiewicz L and Sankowski D (2004), The sensitivity map in the image reconstruction process for electrical capacitance tomography, *Proc. 3rd Int. Symp. on Process Tomography*, 9–10 September, Lodz, Poland, pp 165–168

[99] Wang B L, Huang Z Y, Ji H F and Li H Q (2010), Towards capacitively coupled electrical resistance tomography, *Proc. 6th World Congress on Industrial Process Tomography*, 6–9 September, Beijing, China, pp 1574–1577

[100] Wang H X, Zhu X M and Zhang L F (2005), Conjugate gradient algorithm for electrical capacitance tomography, *J. of Tianjin University*, 38 (1), pp 1–4

[101] Wang M (1994), Electrical impedance tomography on conducting walled vessels, *PhD thesis*, The University of Manchester, UK

[102] Wang M (1999), Three-dimensional effects in electrical impedance tomography, *Proc. 1st World Congress on Industrial Process Tomography*, 14–17 April, Buxton, UK, pp 410–415

[103] Wang M (2002), Inverse solutions for electrical impedance tomography based on conjugate gradients methods, *Meas. Sci. Technol.*, 13, pp 101–117

[104] Wang M and Dickin F J (1994), Signal phase shift and compensation in resistive electrical impedance tomography, Beck M S, Campogrande E, Morris

M, Williams R A and Waterfall R C (editors), *Process Tomography – A Strategy for Industrial Exploitation - 1993*, Karlsruhe, UMIST, ISBN0952316501, pp 193–196

[105] Wang M, Yin W and Holliday N (2002), A highly adaptive electrical impedance sensing system for flow measurement, *Meas. Sci. Technol.*, 13 (12), pp 1884–1889

[106] Warsito W and Fan L -S (2005), Dynamics of spiral bubble plume motion in the entrance region of bubble columns and three-phase fluidized beds using 3D ECT, *Chem. Eng. Sci.*, 60, pp 6073–6084

[107] Warsito W, Marashdeh Q and Fan L -S (2007), Electrical capacitance volume tomography, *IEEE Sensors J.*, 7 (4), pp 525–535

[108] Webster J G (1998), Medical Instrumentation: Application and Design, *3rd ed.*, New York: Wiley

[109] Wilkinson A J, Randall E W, Long T M and Collins A (2006), The design of an ERT system for 3D data acquisition and a quantitative evaluation of its performance, *Meas. Sci. Technol.*, 17, pp 2088–2096

[110] Wu X J, Huang G X, Wang J W and Xu C (2013), Image reconstruction method of electrical capacitance tomography based on compressed sensing principle, *Meas. Sci. Technol.*, 24, pp 075401

[111] Xie C G, Huang S M, Hoyle B S, Thorn R, Lenn C, Snowden D and Beck M S (1992), Electrical capacitance tomography for flow imaging: system model for development of image reconstruction algorithms and design of primary sensors, *IEE Proc. G*, 139, pp 89–98

[112] Xie C G, Stott A L, Plaskowski A and Beck M S (1990), Design of capacitance electrodes for concentration measurement of two-phase flow, *Meas. Sci. Technol.*, 1, pp 65–78

[113] Xue Q, Wang H, Cui Z and Yang C (2012), Electrical capacitance tomography using an accelerated proximal gradient algorithm, *Rev. Sci. Instrum.*, 83 (4), pp 043704

[114] Yan H, Liu L J, Xu H and Shao F Q (2001), Image reconstruction in electrical capacitance tomography using multiple linear regression and regularization, *Meas. Sci. Technol.*, 12, pp 575–581

[115] Yan H, Shao F Q, Xu H and Wang S (1999), Three-dimensional analysis of electrical capacitance tomography sensing fields, *Meas. Sci. Technol.*, 10, pp 717–725

[116] Yang M (2007a), Development of electrical tomography systems and application for milk flow metering, *PhD thesis*, The University of Manchester, UK

[117] Yang W Q (1996), Hardware design of electrical capacitance tomography systems, *Meas. Sci. Technol.*, 7, pp 233–246

[118] Yang W Q (2001), Further developments in an ac-based capacitance tomography system, *Rev. Sci. Instrum.*, 72, pp 3902–3907

[119] Yang W Q (2007b), Tomographic imaging based on capacitance measurement and industrial applications, *Proc. IEEE Int. Workshop on Imaging Systems and Techniques-IST 2007*, 5 May, Krakow, Poland, pp 965–969

[120] Yang W Q (2010), Design of electrical capacitance tomography sensors, *Meas. Sci. Technol.*, 21 (4), pp 042001

[121] Yang W Q and Byars M (1999), An improved normalization approach for electrical capacitance tomography, *Proc. 1st World Congress on Industrial Process Tomography*, 14–17 April, Buxton, UK, pp 215-218

[122] Yang W Q and Conway W F (1998), Measurement of sensitivity distribution of capacitance tomography sensors, *Rev. Sci. Instrum.*, 69 (1), pp 233–236

[123] Yang W Q, Nguyen T, Betting M, Chondronasios A, Okimoto S, Okimoto F T and McCann H (2002), Imaging wet gas separation process by capacitance tomography, *Proc. IS&T/SPIE 14 Symp. Electronic Imaging*, 11 March, San Jose, USA, pp 347–358

[124] Yang W Q and Peng L H (2003), Image reconstruction algorithms for electrical capacitance tomography, *Meas. Sci. Technol.*, 14, pp R1–R13

[125] Yang W Q, Spink D M, York T A and McCann H (1999), An image reconstruction algorithm based on Landweber's iteration method for electrical capacitance tomography, *Meas. Sci. Technol.*, 10, pp 1065–1069

[126] Yang W Q, Stott A L and Beck M S (1994), High frequency and high resolution capacitance measuring circuit for process tomography, *IEE Proc. Circuits Devices Syst.*, 141, pp 215–219

[127] Yang W Q and York T A (1999), New AC-based capacitance tomography system, *IEE Proc. Sci. Meas. Technol.*, 146 (1), pp 47–53

[128] Yang Y J and Peng L H (2013), A configurable electrical capacitance tomography system using a combining electrode strategy, *Meas. Sci. Technol.*, 24, pp 074005

[129] York T (2001), Status of electrical tomography in industrial applications, *J. Electron. Imaging*, 10 (3), pp 608–619

[130] York T, McCann H and Ozanyan K B (2011), Agile sensing systems for tomography, *IEEE Sensors J.*, 11, pp 3086–3105

[131] Zhang L F and Wang H X (2009), A new normalization method based on electrical field lines for electrical capacitance tomography, *Meas. Sci. Technol.*, 20, pp 104028

[132] Zhu Q S, Lidgey F J and Vere-Hunt M A (1992), Improved wideband instrumentation amplifier, *Clin. Phys. Physiol. Meas.*, 13 (Suppl. A), pp 51–55